Tunnel barriers for spin injection into graphene

Inauguraldissertation

zur
Erlangung der Würde eines Doktors der Philosophie
vorgelegt der
Philosophisch-Naturwissenschaftlichen Fakultät
der Universität Basel

von

Matthias Wolfgang Bräuninger
aus Deggendorf (Deutschland)

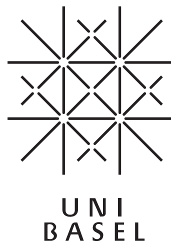

Basel, 2014

Genehmigt von der Philosophisch-Naturwissenschaftlichen Fakultät
auf Antrag von
Prof. Dr. C. Schönenberger
Dr. B. Beschoten

Basel, den 18.02.2014

Prof. Dr. Jörg Schibler
Dekan

Contents

Introduction **1**

1 Theory **3**
- 1.1 Ferromagnetism 3
  - 1.1.1 Exchange interaction 3
  - 1.1.2 Band ferromagnetism and Stoner criterion 5
  - 1.1.3 Shape anisotropy and anisotropic magnetoresistance . . . 6
  - 1.1.4 Permalloy 8
- 1.2 Spin-dependent transport 9
  - 1.2.1 Two-current model and spin polarisation 9
  - 1.2.2 Tunnelling magnetoresistance 10
  - 1.2.3 Spin injection and conductivity mismatch problem 11
  - 1.2.4 Spin relaxation 12
  - 1.2.5 The *F/I/N/I/F* spin valve 13
  - 1.2.6 Non-local measurement geometry 14
  - 1.2.7 Non-local signals with tunnelling and transparent contacts 16
  - 1.2.8 Hanle spin precession 17
- 1.3 Characteristics of graphene 19
  - 1.3.1 Fabrication of graphene 19
  - 1.3.2 Crystallographic properties of graphene 20
  - 1.3.3 Electronic properties and minimum conductivity 21
  - 1.3.4 Raman spectroscopy on graphene 23
  - 1.3.5 Graphene’s feasibility for spin transport 24
  - 1.3.6 Influence of substrate and adatoms 24
  - 1.3.7 Influence of the contact resistance 25
- 1.4 Tunnelling 26
  - 1.4.1 Tunnelling mechanisms in solids 26
  - 1.4.2 Tunnelling vs. pinhole transport in electrical measurements 27
  - 1.4.3 Tunnelling and pinhole signatures in spin transport 28

2 Sample fabrication **29**
- 2.1 UV lithography 29
- 2.2 Graphene deposition 29

2.3 Electron beam lithography . . . 30
2.4 Final fabrication steps . . . 31
2.5 Measurement and characterisation techniques . . . 32

3 Al_2O_3 tunnel barriers 33
3.1 Al_2O_3 deposition on graphene . . . 34
3.1.1 The trimethyl-aluminium/water process . . . 34
3.1.2 NO_2 functionalisation of graphene . . . 35
3.1.3 TiO_2 functionalisation of graphene . . . 36
3.1.4 Summary of the ALD recipes . . . 37
3.2 Characterisation of directly deposited aluminium oxide . . . 37
3.3 Characterisation of the Al_2O_3 layers with NO_2 functionalisation . 38
3.3.1 Fabrication . . . 38
3.3.2 Estimation of the thickness . . . 38
3.3.3 AFM measurements . . . 39
3.3.4 Quality of graphene below NO_2-Al_2O_3 . . . 42
3.3.5 $I - V$ measurements . . . 44
3.3.6 Resistance-area product for two barriers in series . . . 45
3.3.7 Temperature dependence of the $I - V$ measurements . . . 47
3.3.8 Conclusion for the NO_2-seeded ALD layers . . . 49
3.4 Characterisation of the TiO_2-seeded ALD layers . . . 50
3.4.1 AFM measurements . . . 50
3.4.2 Electric measurements . . . 51
3.4.3 Spin-valve measurements . . . 52
3.4.4 Comparison with data from other barriers . . . 54
3.4.5 Conclusion for the TiO_2-seeded ALD layers . . . 55
3.5 Summary . . . 55

4 MgO tunnel barriers 57
4.1 Fabrication . . . 57
4.1.1 Deposition of the MgO layer . . . 58
4.1.2 Lithography . . . 59
4.2 Quality of graphene below MgO . . . 59
4.3 AFM measurements on TiO_2-seeded and non-seeded MgO . . . 61
4.3.1 Thickness of the oxide layers . . . 61
4.3.2 TiO_2/MgO on graphene . . . 64
4.3.3 Conclusion . . . 66
4.4 Transport measurements . . . 67
4.4.1 Electrical measurements . . . 67
4.4.2 Non-local spin-valve measurements . . . 69
4.4.3 Spin precession measurements . . . 72
4.4.4 Single magnetic switches . . . 76
4.4.5 Comparison with data from other barriers . . . 76
4.4.6 Conclusion of the electrical measurements . . . 77

4.5 Summary 77

5 Graphene spin valves with MoS_2 tunnel barriers 79
5.1 Boron nitride vs. MoS_2 79
5.2 Material properties of MoS_2 80
5.2.1 Structural properties 80
5.2.2 Electronic properties 81
5.3 Fabrication 82
5.3.1 Exfoliation of MoS_2 82
5.3.2 Transfer technique 83
5.3.3 Lithography 84
5.3.4 Thermal expansion of the graphene-MoS_2 stacks 85
5.4 Characterisation of MoS_2 87
5.4.1 Raman spectroscopy on a graphene-MoS_2 heterostructure 87
5.4.2 AFM characterisation of bare MoS_2 87
5.4.3 AFM measurements on MoS_2 on graphene 89
5.4.4 Transport measurements on bare MoS_2 91
5.4.5 Conclusion 94
5.5 Electrical measurements on graphene-MoS_2 stacks 95
5.5.1 Determination of the contact resistance 95
5.5.2 Contact resistances in graphene-MoS_2 heterostructures . . 96
5.5.3 Conductance fluctuations 99
5.5.4 Conclusion 101
5.6 Spin-valve measurements 101
5.6.1 Three-terminal measurements 101
5.6.2 Four-terminal non-local measurements 103
5.6.3 Comparison with data from other barriers 104
5.6.4 Conclusion 104
5.7 Summary 105

6 Summary and outlook 107

A Lithography issues 111

B Schottky barriers at the permalloy-MoS_2 interface 113

C Offset voltages in non-local measurements 115
C.1 Common-mode signal from the voltage amplifier 116
C.2 Thermoelectric contributions from Joule or Peltier heating 118
C.3 Conclusion 119

D Correlation between contact resistances and non-local signals 121

Bibliography 125

Curriculum Vitæ **137**

List of publications **139**

Technology is neither good nor bad; nor is it neutral.

Melvin Kranzberg's (1917 – 1995) First Law of Technology

Introduction

In today's microprocessors, information is transmitted and controlled by electrical currents using a large number of transistors. The last decades have seen a continuous decrease in the dimensions of the transistors, and thus a strong increase in their density on a microprocessor. So far, this trend has allowed for a steady rise in computation power and efficiency. However, further reduction of the channel lengths of the transistors will eventually lead to quantum tunnelling between source and drain contacts, i. e. leakage currents reducing the on-off ratio of a transistor. This constitutes a hard limit to further miniaturisation.

On the other hand, the ongoing size reduction allows the access of length scales which are comparable to the diffusion lengths of electron spins. Hence, one possible evolution of electronics is the technology of *spintronics* [1–4]. This portmanteau word for *spin transport electronics* describes a technology paradigm which aims to encode and transmit information using the spins of the electrons. These can assume two possible states, "up" (↑) and "down" (↓), analogous to the "on" and "off" states of a conventional transistor. Due to the magnetic moment of a spin, this property is intrinsically linked to magnetism. A prominent example from the field of spintronics is the *giant magnetoresistance* (GMR) effect, independently discovered by the groups of A. Fert and P. Grünberg [5, 6]. GMR is based on spin-dependent scattering of electrons in ferromagnets and led to a considerable increase in storage densities of magnetic hard disks during the last decade.

The technological use of spins also opens the possibility to implement quantum-mechanical concepts like entanglement and superposition into solid-state-based devices. As an example, the quantum-mechanical superposition of spin-up and spin-down states, e. g. in a single-electron quantum dot [7], defines a quantum bit (*qubit*) which forms the basis of the paradigm of quantum computation.

A prepared spin ensemble will relax to its ground state, thus losing the encoded information, after a certain material-dependent *relaxation time*. Most spintronic applications require long relaxation times which allow conducting logic operations and information storage. A possible candidate for such a material is the carbon allotrope graphene, a zero-gap semiconductor, which was first fabricated and investigated in 2004 [8]. Due to its very weak hyperfine and spin-orbit coupling [9, 10], this material promises low intrinsic spin relaxation and

thus long spin relaxation times. Successful spin injection into graphene from a ferromagnetic electrode was first demonstrated by Tombros *et al.* [11] in lateral spin-valve structures. They also extracted spin diffusion lengths of an order of magnitude as high as μm which have since been surpassed by this and other research groups. These length scales are well-suited for device fabrication. Together with the prospect of a long intrinsic spin half-life, this has made graphene a very promising choice as spin transport material.

To ensure the successful injections of spins from a ferromagnet into e. g. a non-magnetic semiconductor, a high-quality tunnel barrier has to be inserted between the two materials [12]. This barrier allows to avoid the effect of conductivity mismatch which strongly degrades the spin injection efficiency [13]. Tunnel barriers have been the central aspect of this work.

This thesis describes the fabrication, characterisation and optimisation of suitable tunnel barriers for spin injection as well as detection experiments with graphene. The thesis is structured in the following way:

- **Chapter 1** covers the basic theory by giving brief introductions to relevant magnetic effects, spin transport, graphene and tunnelling.
- The fabrication steps common to all our samples are summarised in **chapter 2**. This chapter also features a brief description of our measurement setups and cryostats.
- **Chapters 3** and **4** focus on the Al_2O_3 and MgO tunnel barriers, respectively. They describe the fabrication methods and optimisation of these oxide barriers and the characterisation of the graphene spin-valve devices by electrical and magnetic measurements.
- In a different approach, we use the layered dichalcogenide MoS_2 as tunnel barrier on graphene. **Chapter 5** gives an overview over the properties of MoS_2 and the fabrication method and summarises our own results of the characterisations of the bare MoS_2 layers. Electronic and magnetic measurements of the graphene-MoS_2 heterostructures are shown as well.

Chapter 1

Theory

Spintronics is directly linked to ferromagnetism, because ferromagnetic electrodes can provide charge carriers which are spin-polarised, at least to a certain degree. The following section 1.1 briefly explains the physical mechanisms behind ferromagnetism and introduces the ferromagnet *permalloy* from which we have fabricated our electrodes. Section 1.2 summarises basic aspects about spin transport. 1.3 describes the basic structural and electronic properties of graphene, as well as its particular spin transport properties. The theory chapter concludes with a brief description about tunnelling and the signature of pinholes in a tunnelling barrier (section 1.4).

1.1 Ferromagnetism

This section introduces the most important concepts, notably the exchange interaction (section 1.1.1) and the band ferromagnetism of Fe, Co and Ni (section 1.1.2). Parts of this section follow existing literature [14–17].

1.1.1 Exchange interaction

Ferromagnetism is a collective ordering of the electron spins in certain materials. This effect manifests itself below a certain temperature, the *Curie temperature*, which depends on the ferromagnetic material. The collective ordering is a purely quantum-mechanical phenomenon [18] and was found to be a direct consequence of the exchange interaction, which arises from both the Coulomb interaction and the Pauli exclusion principle. The theoretical treatment of an H_2 molecule reveals that the exchange of electrons between the two H atoms causes a bonding force, termed *covalent bonding*.

Since electrons are fermions, their total wave functions Ψ must be antisymmetric upon pairwise exchange of two indistinguishable electrons. This leads to either symmetric spatial wave functions $\varphi_{1,2}$ with an antisymmetric spin part χ or an

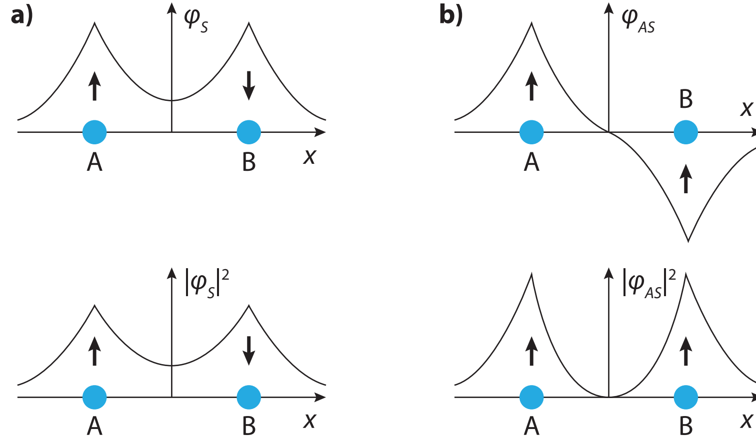

Figure 1.1: Hydrogen molecule with electrons of **a)** symmetric and **b)** antisymmetric spatial wave functions φ_S, φ_{AS}. $|\varphi_S|^2$ and $|\varphi_{AS}|^2$ denote the probability densities of the electrons, the arrows represent the spin functions. After [19].

antisymmetric spatial function with symmetric spin part. These combinations reflect the Pauli princple: A symmetric spatial electron wave function means that the electrons may have identical quantum numbers (n, l, m_l) and they are spatially close (often denoted *Fermi heap*). As a consequence, their spins must differ [14]. The antisymmetric spin part forms a singlet (S) state:

$$\chi_S(s_1, s_2) = \frac{1}{\sqrt{2}}(|\uparrow\downarrow\rangle - |\downarrow\uparrow\rangle) \quad S = 0. \tag{1.1}$$

The symmetric spin part leads to a triplet (T) state:

$$\chi_T(s_1, s_2) = \begin{cases} |\uparrow\uparrow\rangle & S = 1, m_S = 1 \\ \frac{1}{\sqrt{2}}(|\uparrow\downarrow\rangle + |\downarrow\uparrow\rangle) & S = 1, m_S = 0 \\ |\downarrow\downarrow\rangle & S = 1, m_S = -1 \end{cases} \tag{1.2}$$

When calculating the energies of the singlet and the triplet state, one learns that the singlet state has the lowest energy in H_2, because both electrons are localised between the H atoms, thus creating a bonding force. The spatial part of their wave function is symmetric, which results in an antisymmetric spin configuration. Note that the singlet is not generally the lowest energy state: The situation is reversed when considering e. g. an He atom. In this case, the Coulomb repulsion between the two electrons dictates that they should be further apart (see fig. 1.1, this situation is also called *Fermi hole*), which is fulfilled by a wave function with antisymmetric spatial part. This combination of Coulomb interaction between electrons and the Pauli principle is called *exchange interaction* [14].

The energy difference between singlet and triplet state is $E_T - E_S = -2J$, J is called *exchange constant*. Using J, one can introduce a model Hamiltonian, the *Heisenberg operator*, acting on the electrons' spin functions:

$$\mathcal{H}_{\text{spin}} = -2J\sigma_1\sigma_2, \tag{1.3}$$

where the spin operators σ can be represented by the Pauli spin matrices [16].

1.1.2 Band ferromagnetism and Stoner criterion

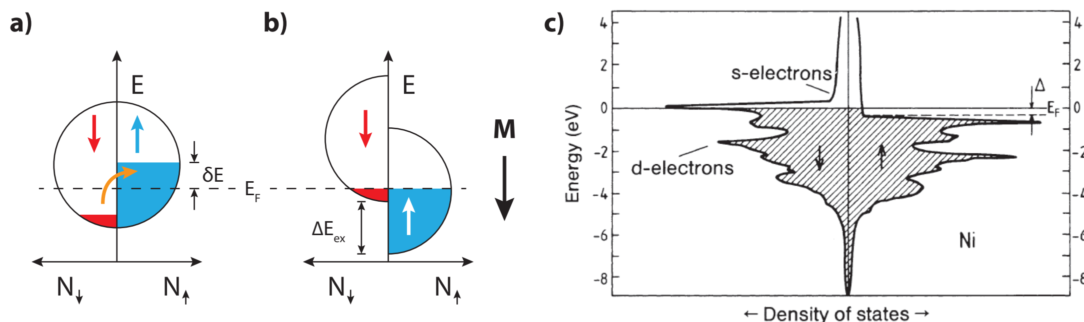

Figure 1.2: a) Spin-flip processes (orange arrow) from the ↓ band to the ↑ band lead to separate densities of states (DOS) for the majority spins (blue) and the minority spins (red) in **b)**. The DOS are represented by semi-circles (modeled after [19]) and separated by the exchange splitting ΔE_{ex}. The magnetisation $\boldsymbol{M}$ points in the direction of the minority spins. This sketch represents the *Stoner model* of a ferromagnet [14]. **c)** Calculated DOS of Ni (from [16]).

In the 3d transition metals Fe, Co and Ni, these simple considerations for the pairwise interactions between electrons do not hold anymore. The density of states (DOS) in ferromagnets differs for electrons with ↑ and ↓ spins, creating a non-equilibrium distribution of the spins, which is commonly referred to as *spin splitting* of the DOS and which can be described by the *Stoner model*. In Fe, Co and Ni, this splitting occurs spontaneously, i. e. it is not caused by an external magnetic field. It is governed by the electrons in the partly filled d bands, hence the name *band ferromagnetism*. A brief description of the underlying mechanisms is given below and can be found in more detail in references [14–16].

The spontaneous splitting of the DOS is caused by the exchange interaction and corresponds to an arrangement of the conduction electrons which is energetically more favourable than a random distribution: The Pauli principle forbids two electrons with the same spin wavefunction to share the same spatial wavefunction. Hence, the electrons have less spatial overlap (cf. section 1.1.1) and the Coulomb attraction between atomic cores and considered electrons is less well screened, which reduces the electrons' potential energy. The more electrons align their spins with each other, the lower their potential energy becomes.

This alignment corresponds to spin-flip processes of $\downarrow$ electrons in an interval $[E_F - \delta E, E_F]$. The kinetic energy of the spin-flip electrons increases by δE, because the electrons are added to the $\uparrow$ band (cf. fig. 1.2 a)). Consequently, the number of $\uparrow$ spins is greater and the corresponding spin direction is called *majority spin* direction. *Minority* (or, $\downarrow$) *spin* refers to the opposite spin direction in the band with fewer spins. The increase in kinetic energy caused by spin flips competes with the energy decrease from the exchange interaction described above and can lead to a spontaneous ferromagnetic ordering of the spins in the system. This competition is expressed by the *Stoner criterion*,

$$I\tilde{D}(E_F) > 1 \tag{1.4}$$

where I is the *Stoner parameter*, related to the exchange-related energy decrease, and $\tilde{D}(E_F)$ is the density of states per atom and spin direction at the Fermi level. A combination of a strong exchange interaction and a large DOS at the Fermi level leads to spontaneous ferromagnetism, which is the case for the 3d-metals Fe, Co and Ni. Fig. 1.2 c) shows a calculation for the spin-dependent DOS in Ni.

Ferromagnetic ordering leads to the formation of domains where the spins are aligned in the same direction and which give rise to a finite magnetisation of ferromagnets. Fig. 1.2 b) illustrates the convention used in this thesis: The *magnetisation* $\boldsymbol{M}$ of the ferromagnet is the sum over all magnetic moments associated with the spins. $\boldsymbol{M}$ points in the direction of the minority spins.

The degree of *spin polarisation* (DSP) in the bulk of a ferromagnet is related to the value $\mathcal{N}_{\uparrow(\downarrow)}(E_F)$, the spin-dependent DOS at the Fermi energy, where $\uparrow$ ($\downarrow$) is the respective spin direction. The DSP is defined as [20]

$$P_{\mathcal{N}} := \frac{\mathcal{N}_{\uparrow}(E_F) - \mathcal{N}_{\downarrow}(E_F)}{\mathcal{N}_{\uparrow}(E_F) + \mathcal{N}_{\downarrow}(E_F)}. \tag{1.5}$$

$|P_{\mathcal{N}}|$ can assume values between 0, corresponding to a non-magnetic metal, and 1, which indicates a full majority and an empty minority spin band. An excess of minority spin electrons at the Fermi surface gives $P_{\mathcal{N}}$ a negative sign, as in the case of Ni (see Mazin [20] and fig. 1.2 c). $P_{\mathcal{N}}$ can be probed e. g. by spin-resolved photoemission.

1.1.3 Shape anisotropy and anisotropic magnetoresistance

If a sample of a ferromagnetic material is not perfectly isotropic, its magnetisation $\boldsymbol{M}$ depends strongly on the sample geometry (*shape anisotropy*). Elongated shapes, e. g. ellipsoids, are easier to magnetise along their long axis (or, *easy axis*). Our electrodes are shaped as cuboids, hence $\boldsymbol{M}$ is preferentially aligned along the cuboid's easy axis when no external field is applied.

An external magnetic field $\boldsymbol{B}_{\text{ext}}$ can be used to reverse the magnetisation of the strip, which is described by the *Stoner-Wohlfarth model* [21]. Since, in our experiments, we chose $\boldsymbol{H}_{\text{ext}}$ to be parallel to the long axis of the contact strips, this explanation is restricted to the case that $\boldsymbol{M}$ is parallel to the easy axis as well – parallel and antiparallel alignment are energetically most favourable. Upon reversing $\boldsymbol{B}_{\text{ext}}$ to antiparallel alignment with the strip, $\boldsymbol{M}$ also changes its orientation to antiparallel alignment with $\boldsymbol{B}_{\text{ext}}$ at a certain switching field which is on average identical to the coercive field H_c of the ferromagnetic strip [21]. Due to the dependence of H_c on the geometry, electrodes of different width can be created, whose magnetisations switch at different coercive fields.

One way to determine the coercive field of a ferromagnetic electrode is the *anisotropic magnetoresistance* (AMR) which was first observed by Thomson [22]: When a current $\boldsymbol{j}$ passes through a ferromagnetic strip which has a magnetisation $\boldsymbol{M}$, the strip's resistivity is different for the cases $\boldsymbol{j} \parallel \boldsymbol{M}$ and $\boldsymbol{j} \perp \boldsymbol{M}$.

An AMR measurement, recorded at 2 K, is presented in fig. 1.3 a) for a 300 nm wide permalloy strip. Its electrical resistance R_{strip} is measured while the magnetisation is gradually reduced to negative values. For an external field $\boldsymbol{B}_{\text{ext}}$ which is aligned parallel to the easy axis, one obtains the situation $\boldsymbol{B}_{\text{ext}} \parallel \boldsymbol{j} \parallel \boldsymbol{M}$. This is the case for values of $B_y \geq 25$ mT for the orange curve in the figure. During the reversal of B_y, one can observe that R_{strip} decreases when the coercive field H_c is approached (see fig. 1.3 a), corresponding to the formation of several domains in the ferromagnet. At H_c itself, a sharp upwards switching feature indicates the reversal of the strip's magnetisation $\boldsymbol{M}$.

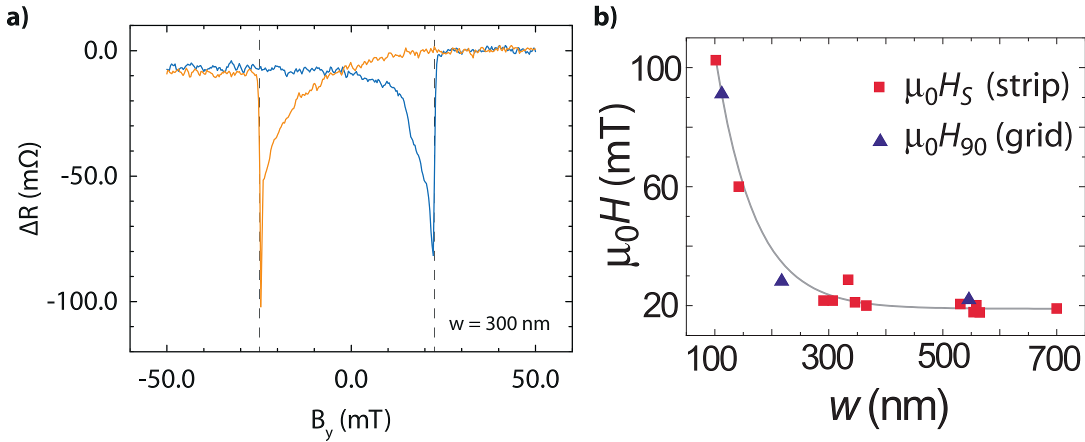

Figure 1.3: a) AMR curve (own measurement) for a 300 nm wide strip with a clear jump at H_c, indication the reversal of its magnetisation. Strip width and coercive field correspond well to previously obtained data shown in b). The large width of the dip shows that the contact strip forms several magnetic comains as B_y approaches H_c. **b)** Width dependence of the magnetic coercive field for elongated permalloy rectangles with a thickness of 25 nm and lengths between 10 and 17 μm. The grey line is a guide to the eye. From [23].

This behaviour of R_{strip} in fig. 1.3 a) is explained by the anisotropic shape of the $3d$ orbitals of the ferromagnet which follow the magnetisation. We have fabricated electrodes from permalloy ($Ni_{80}Fe_{20}$, see section 1.1.4 below). Transport in Ni is dominated by light s electrons rather than its heavy d electrons (cf. fig. 1.2) [24]. Spin-orbit coupling in the material causes spin-flip scattering and majority s electrons can be scattered into minority d states which increases the resistance [15]. This is strongest when the direction of the current is parallel to $\boldsymbol{M}$ [24]. Due to the anisotropy of the d orbitals, which change direction with $\boldsymbol{M}$, the scattering (and thus R_{strip}) also depends on the angle between $\boldsymbol{j}$ and $\boldsymbol{M}$. The resistance is lowered when $\boldsymbol{H}_{\mathbf{ext}}$ is near the coercive field and, due to imperfections in the strip and its alignment in the external field, $\boldsymbol{j} \parallel \boldsymbol{M}$ does not hold anymore. In an ideal strip, which forms one large domain, the AMR signal is a very narrow spike. Note that, at higher temperatures, magnon magnetoresistance (MMR) can play a role as well [25]. Near H_c, MMR leads to an increase in resistance and to a downwards jump at H_c, which can mask the AMR signal.

The width dependence of the coercivities of permalloy is shown in fig. 1.3 b), taken from [23]. Their data were recorded on strips of 25 nm thickness and lengths between 10 and 17 μm. The red squares correspond to electrical measurements, the triangles correspond to measurements of the magnetisation of a large amount of identical permalloy strips with a vibrating sample magnetometer (cf. Aurich [17]).

1.1.4 Permalloy

We chose permalloy for the fabrication of the ferromagnetic electrodes (cf. [17]). Permalloy, or $Ni_{80}Fe_{20}$, is an alloy of nickel and iron with ferromagnetic properties. It is a soft ferromagnet with low coercivities, hence its magnetisation can be reversed using relatively small magnetic fields (see also section 1.1.3). In addition, it shows a low magnetostriction, i. e. a low deformation under an external magnetic field.

It is an important prerequisite for spin injection that the electrodes must have uniform magnetisation, at least over their cross-section area with the spin transport material, to ensure that the maximum amount of spins of either $\uparrow$ or $\downarrow$ alignment are injected. Permalloy fulfills that requirement because it only forms few, large domains when magnetised [26].

Permalloy shows a spin polarisation in the range of $P_{\mathrm{Py}} = 0.45 \ldots 0.48$ [27–29]. Its electrical resistivity, ρ_F, lies between 25 $\mu\Omega\,\mathrm{cm}$ [17] and 50 $\mu\Omega\,\mathrm{cm}$[1]. For permalloy's spin polarisation length λ_F, rather low values of 4.3 nm [30] and 5.5 nm [31] were reported independently. Furthermore, Nadgorny *et al.* [28]

[1]Measured by J. Gramich from our group, personal communication

state that spin tunnelling in Ni_xFe_{1-x} systems is governed by the majority spins despite a smaller DOS at E_F. Thus, the injected spins are antiparallel to the magnetisation of the permalloy electrodes which is reflected in most spin injection sketches throughout this thesis.

1.2 Spin-dependent transport

This section compiles several aspects of spin transport, such as injection, detection and relaxation in regard to the experiments we conducted. Parts of this section follow the existing literature [3, 32].

1.2.1 Two-current model and spin polarisation

As a consequence of the spin splitting of the density of states (DOS) in ferromagnets (see fig. 1.2 in section 1.1.2), the spin-dependent transport in a ferromagnet can be described independently for both spin directions by using the *two-current model* originally developed by Mott [33, 34]. Due to negligible scattering between the spin channels, this model allows to give separate conductivities $\sigma_{\uparrow(\downarrow)}$, where $\sigma_\uparrow$ represents majority ($\uparrow$) spins and $\sigma_\downarrow$ minority ($\downarrow$) spins in a bulk ferromagnet. The degree of the current's polarisation in the ferromagnet is defined as

$$P_F = \frac{\sigma_\uparrow - \sigma_\downarrow}{\sigma_\uparrow + \sigma_\downarrow} \tag{1.6}$$

Spin transport phenomena often require the knowledge of the degree of spin polarisation (DSP). Mazin [20] states that the definition of the DOS-dependent DSP $P_\mathcal{N}$, given in section 1.1.2, is not suitable for explaining transport phenomena. The particular DOS of a ferromagnet mainly arises from the contributions of heavy d electrons, whereas transport in band ferromagnets is governed primarily by lighter s electrons. The definition for transport-related spin polarisation can be derived using the two-current model and reads

$$P_T = \frac{j_\uparrow - j_\downarrow}{j_\uparrow + j_\downarrow}, \tag{1.7}$$

which is the ratio of the spin-polarised current (enumerator of the fraction) and the total electric current (denominator). $j_{\uparrow(\downarrow)}$ denotes the majority (minority) spin current density across an interface, such as $F/I/F$[2] (magnetic tunnel junction, 1.2.2), F/N[3] and $F/I/N$ interfaces (1.2.3), described in the following sections. P_T can be determined from spin-dependent tunnelling experiments, e. g. with magnetic tunnel junctions (see section 1.2.2).

[2] **f**erromagnet/**i**nsulator/**f**erromagnet
[3] **f**erromagnet/**n**on-magnetic material

1.2.2 Tunnelling magnetoresistance

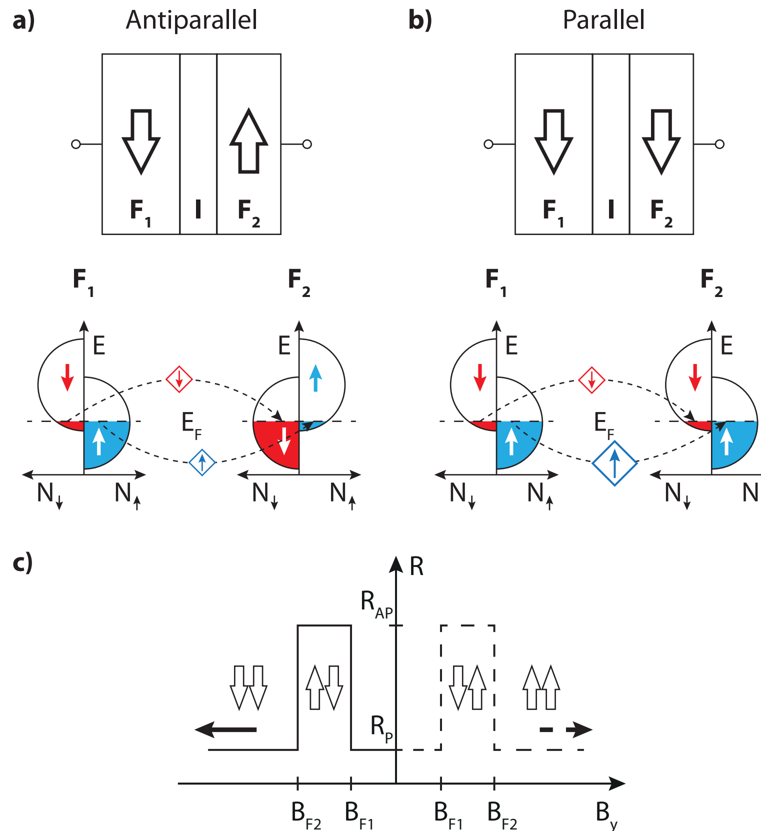

Figure 1.4: a) Sketch of a magnetic tunnel junction (MTJ) with both electrodes F_1 (polariser) and F_2 (analyser) in antiparallel magnetisation (denoted by the hollow arrows). The sketch below shows the corresponding spin-dependent densities of states (DOS). F_2's DOS has fewer ↑ states available for the ↑ spins arriving from F_1. This leads to scattering and to an increase in resistance. **b)** Parallel configuration of the MTJ. Both electrodes have the same majority spin direction and the resistance for the majority spin channel is considerably lower than for the minority channel. The spin-dependent DOS shows that the majority spins from F_1 find enough states in F_2. Inspired by [3]. **c)** Device resistance in dependence of an external magnetic field B_y at parallel and antiparallel magnetisations.

An easy example for spin-dependent transport is the *tunnelling magnetoresistance* (TMR), first defined by Jullière [35]. Jullière measured the tunnelling conductance in a *magnetic tunnel junction* (MTJ) where Fe and Co electrodes were separated by a 10 nm thin oxidised Ge film. Fig. 1.4 shows a sketch of such an MTJ with ferromagnetic electrodes F_1 and F_2 and an insulating layer I acting as tunnel barrier (cf. section 1.2.3). The transport through this device is referred to as $F/I/F$ tunnelling [3].

The electric resistance of an MTJ can be manipulated by an external magnetic field B_y. Using two ferromagnets, one of them being magnetically softer than

the other, their magnetisations can be varied independently by B_y, which allows to choose parallel (P) or antiparallel (AP) alignments of the electrodes' magnetisations. This will also change their majority and minority spins. Antiparallel magnetisation (fig. 1.4 a) will yield a high resistance of the MTJ, whereas tuning the electrodes to parallel magnetisation (fig. 1.4 b) decreases the resistance.

This is described by the *tunnelling magnetoresistance*, defined as [3]

$$TMR = \frac{\Delta R}{R_P} = \frac{R_{AP} - R_P}{R_P} = \frac{G_P - G_{AP}}{G_{AP}} \tag{1.8}$$

$$= \frac{2P_1 P_2}{1 - P_1 P_2}, \tag{1.9}$$

where P_1 and P_2 are the spin polarisations related to the densities of states of the two ferromagnets (see section 1.2.1). These spin-dependent DOS are relevant for the dependence of the device resistance on an external field B_{ext}:

For transport considerations, only electrons near E_F are relevant. For antiparallel magnetisations, the injected majority spins, which arrive from the polariser electrode, find considerably less available states in the analyser than in the parallel case. As a consequence, they are scattered at the interface between I and F_2. Only few minority spins are injected (cf. fig. 1.4 a). This increases the resistance in comparison to the parallel case where the injected majority spins find enough available states in the analyser.

In the extreme case of fully spin-polarised electrodes, only majority spins are present in the ferromagnet. In the absence of any spin-flip scattering, an antiparallel magnetisation of the spin valve would cause an infinite electrical resistance because there are no free states in the analyser electrode for the majority spins injected from the polariser.

1.2.3 Spin injection and conductivity mismatch problem

Electronic spin injection is the transfer of spin-polarised electrons, usually supplied from a polarised ferromagnetic contact (F), into a non-magnetic material (N), as sketched in fig. 1.5 a). This results in a magnetisation flow δM from F to N and generates a spin imbalance in N, referred to as *spin accumulation*. As a consequence, the Fermi level of N will be split into $\uparrow$ and $\downarrow$ subbands (cf. fig. 1.5 b). Charge neutrality in N dictates that the excess of $\downarrow$ spins is accompanied by a lack of $\uparrow$ spins, and vice versa [36]. Assuming diffusive spin transport in N, δM decays within a certain distance $\lambda_s = \sqrt{D\tau_s}$ from the interface. D is the diffusion constant of the spins – note that, since the spins are coupled to the electrons, charge and spin diffusion constants, D_c and D_s, are virtually the same. This has also been verified for graphene by Józsa *et al.* [37]. Hence, $D_c \approx D_s = D$ will be used throughout this thesis. τ_s, the half-life of the polarised ensemble, is usually

referred to as *spin relaxation time* and is section 1.2.4 below for a more detailed treatment).

A detector placed within a distance λ_s from the first interface can measure δM which can be obtained in the form of a current if the contact from N to the detector is transparent (see fig. 1.5 c), or a voltage in case of a weakly coupled detector (fig. 1.5 d) [36].

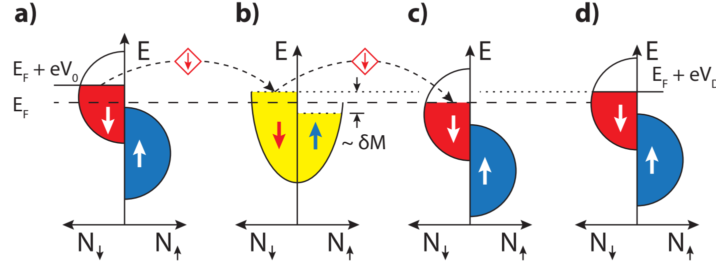

Figure 1.5: Illustration of spin injection and detection. **a)** Spin-polarised DOS of a Stoner ferromagnet (F) with an applied bias voltage V_0. **b)** F is in contact with into a non-magnetic material (N) and a spin-polarised current (↓) flows from F to N. A non-equilibrium magnetisation δM is introduced in N. **c)** Strongly coupled F detector in contact with N. **d)** The Fermi level of a weakly coupled F detector will align with the non-equilibrium Fermi level of N. Adapted from [36].

When spins are injected from a ferromagnetic metal into a semiconductor SC, the spin injection efficiency is very low if the ferromagnet is in direct contact with the semiconductor [13] (*transparent* contact). The conductivities of F and SC differ strongly (*conductivity mismatch*) and, in contrast to F, the conductivities in an SC do not depend on the spin alignment. The spin splitting at the F-SC interface becomes very small [3] which leads to a very low spin imbalance in the semiconductor. As a consequence, one obtains only very weak signals which are hard to measure. Some groups successfully tried to overcome this obstacle by using ferromagnetic semiconductors as spin polarisers [38, 39]. Rashba [12] suggested introducing a high interface resistance, as e. g. exhibited by a tunnel barrier, between the ferromagnetic contacts and the semiconducting spin transport material to increase the imbalance in the semiconductor. This has also been proven to work well in the case of graphene [11]. Several groups [40, 41] have systematically researched various ferromagnet-graphene contacts with different transparencies (see also section 1.3.7).

1.2.4 Spin relaxation

After their injection into a non-magnetic material N (e. g. a semiconductor SC), the electron spins are usually subject to four important spin relaxation processes. These can quickly decrease the degree of the injected polarisation within N, thus

reducing the length scale λ_s on which a nonequilibrium spin can be detected (cf. section 1.2.3). For many types of spin transport experiments, long spin relaxation times are desirable, hence strong spin relaxation can render a certain N material unsuitable for spintronics. Usually, four spin relaxation mechanisms are reported to be relevant for metals and semiconductors:

1. *Elliot-Yafet* (EY) mechanism: Spin flips can occur when charge carriers are scattered at impurities
2. *D'yakonov-Perel'* (DP) mechanism: Spin-orbit coupling causes precession of the electron spins, which causes dephasing of the prepared spin ensemble
3. In p-doped semiconductors and at low temperatures, the *Bir-Aronov-Pikus* (BAP) mechanism becomes relevant. This mechanism causes electron spin relaxation by local fluctuating magnetic fields caused by electron-hole exchange scattering [3, 42]
4. *Hyperfine interaction* can couple nuclear and electron spins which leads to electron spin relaxation by the material's nuclei

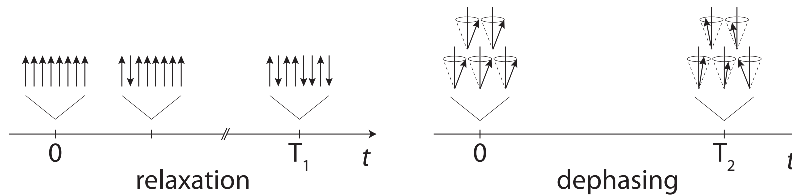

Figure 1.6: Spin relaxation during T_1 and spin dephasing during T_2

These relaxation mechanisms will gradually randomise the individual spins and thus reduce their polarisation on certain time scales. Two important values are the *spin relaxation time* T_1 and the *spin dephasing time* T_2 [3]. During T_1, the spin ensemble exchanges energy with the lattice and loses its well-ordered state. T_2 is the time during which spins, precessing in phase about an external field, lose their phase. This is directly linked to a reduction in the diffusion length $\lambda_s = \sqrt{\tau_s D}$, where the spins' half-life τ_s is any of T_1, T_2.

1.2.5 The *F/I/N/I/F* spin valve

Non-magnetic materials N usually show a much longer spin half-life than F metals. This allows the manipulation of the spins on longer length scales and is crucial to spintronic data storage applications. A prominent example is the spin transistor, proposed by Datta and Das [43], which uses the *spin-valve* geometry.

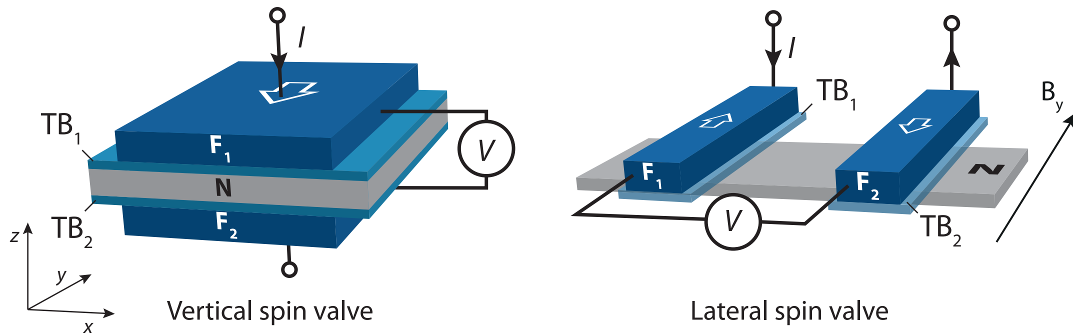

Figure 1.7: Vertical and lateral spin valve geometries, consisting of two ferromagnets $F_{1,2}$ contacting a non-magnet N via barriers TB_1 and TB_2.

A spin valve, as depicted in fig. 1.7 a)[4], is different from an MTJ in that the spins are injected from F_1 into a non-magnetic material (N). Both the injector and the detector F_2 are separated from N by an insulating tunnel barrier ($TB_{1,2}$ in the figure). During the transport in N, which can be a metal or a semiconductor, the spins will usually experience relaxation governed by mechanisms relevant for the N material (see section 1.2.4).

Fig. 1.7 shows the two existing types of spin valves. A big advantage of the lateral geometry is the possibility to gate the non-magnetic material in order to test the influence of the charge carrier density on the spin transport, or to electrostatically manipulate the spin ensemble's direction [3, 43]. It is also possible to fabricate contacts with different distances, which allows testing the spin relaxation length. Furthermore, since the shape anisotropy leads to different coercive fields of the electrodes, the fabrication is facilitated in comparison to vertical spin valves: Different coercivities in lateral spin valves can easily be obtained by fabricatind contacts with different widths. Vertical spin valves would require a soft and a hard ferromagnetic contact, which are usually made from different materials, leading to more fabrication steps. Due to graphene's low thickness, the lateral geometry is best suited for graphene-based spin valves.

1.2.6 Non-local measurement geometry

A very common spin-valve geometry in spintronics is the non-local lateral spin valve [11], first proposed by Johnson and Silsbee [45]. Four electrodes are placed on a graphene[5] sheet (see fig. 1.8 a) and are separated from graphene by tunnel

[4]This combination of ***F*** contacts, **i**nsulating barriers and **n**on-magnetic material is often referred to as *F/I/N/I/F* spin valve [44] or current-perpendicular-to-plane (CPP) spin valve

[5]The description in this section will restrict to graphene as non-magnetic (N) material, but the non-local geometry is suitable for any thin N film.

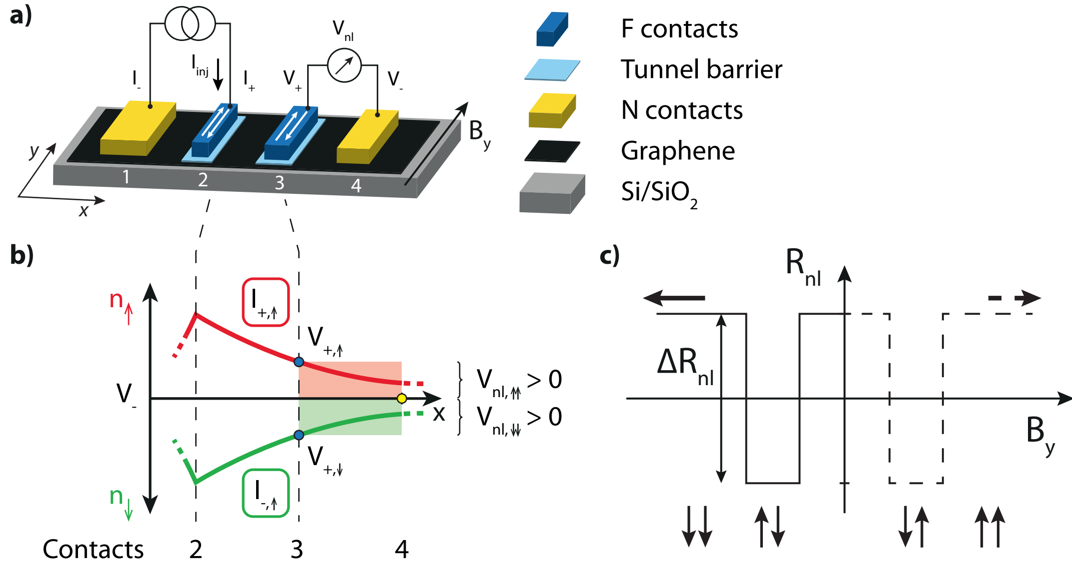

Figure 1.8: a) Sketch of a non-local graphene spin-valve device with ferromagnetic polariser (I_+) and analyser (V_+) electrodes, both aligned in y direction. I_- is the ground electrode and V_- the reference electrode for the voltage measurement. **b)** Spin density and non-local signal: The red and green branch show the density of the injected spins, which is determined by the magnetisation of the injector I_+. The detector V_+ measures the concentration of the $\uparrow$ or the $\downarrow$ spins (blue dot on the red or green branch) in respect to the non-magnetic reference electrode V_- (yellow dot; the blue dots would represent ferromagnetic reference electrodes – see text). $V_{\text{nl}} > 0$ corresponds to parallel magnetisations of injector and detector, $V_{\text{nl}} < 0$ to the antiparallel case. After [11]. **c)** The jumps in V_{nl} indicate switches of the contacts' magnetisation as described in b) (for clarity, the flat parts of the curves have been left out). The horizontal arrows indicate the sweep direction of B_y.

barriers to improve spin injection and detection. In this configuration, a spin-polarised charge current is injected at the polariser electrode I_+ and flows to the ground electrode I_- (see fig. 1.8 a). I_+, V_+ and V_- are on the same electrostatic potential. Since charge carriers can diffuse between the injector and the other electrodes, the spin accumulation below I_+ leads to a pure spin current outside the current loop, which is subject to dephasing and relaxation depending on the spin transport material N. This non-equilibrium spin concentration can be measured between the electrodes V_+ and V_- (see also fig. 1.5) as *non-local voltage* $V_{\text{nl}} := V_{+\uparrow(\downarrow)} - V_-$, which measures the purely spin-dependent chemical potential difference caused by relaxation/dephasing of the injected, diffusing $\uparrow$ ($\downarrow$) spins. This method allows the detection of very small changes in the chemical potential separately from the electrostatic potential.

As already mentioned in section 1.2.4, the injected spins relax in N within a certain diffusion length $\lambda_s = \sqrt{D\tau_s}$ (cf. section 1.2.3). Hence, V_+ should be placed within a distance λ_s from the polariser in order to obtain a spin-dependent signal. Fig. 1.8 b) shows the decreasing net spin density of the injected electrons,

which are diffusing between polariser, analyser and reference. The red curve represents the injected ↑ spins, the green curve the injected ↓ spins, depending on the magnetisation of I_+. The measured non-local signal mainly depends on the magnetisation directions of the polariser I_+ and the analyser V_+ electrodes. In the case of parallel magnetisations, the detector V_+ is sensitive to the same type of spins injected at I_+. This results in a positive non-local voltage $V_{\mathrm{nl},P}$, which is represented by the red box in fig. 1.8 b).

The magnetisation of e. g. the detector can be flipped by reducing the external magnetic field B_y below the coercive field of the electrode. In antiparallel configuration, V_+ probes the spin alignment opposite to I_+, which corresponds to a lack in the spin alignment to which V_+ is sensitive. The resulting signal $V_{\mathrm{nl},AP} = -V_{\mathrm{nl},P}$ is negative, represented by the green box in fig. 1.8 b). Since the magnetisation flips very quickly (cf. section 1.1.3), a sharp jump ΔV_{nl} from positive to negative values marks the $P \rightarrow AP$ transition. A similarly sharp transition occurs at the transition $AP \rightarrow P$ when B_y is further reduced (cf. fig. 1.8 c). A non-local resistance can be defined as the ratio of the measured non-local voltage and the injected current:

$$R_{\mathrm{nl}} := \frac{V_{\mathrm{nl}}}{I_{\mathrm{inj}}} \quad \text{and} \quad \Delta R_{\mathrm{nl}} = R_{\mathrm{nl},P} - R_{\mathrm{nl},AP} = 2R_{\mathrm{nl},P} \tag{1.10}$$

In fig. 1.8, only two electrodes are ferromagnetic. The fabrication process can be simplified by choosing the same ferromagnetic material for all contact strips. If the ferromagnetic reference electrode is too close to the analyser, the measured signal is reduced because of its own spin sensitivity. The distance between V_+ and V_- should therefore be much longer than λ_s such that all spins have relaxed and the ferromagnetic electrode V_- probes equilibrium spin distribution in N. If more than two ferromagnetic electrodes are used, more than two jumps can appear in the non-local signal in fig. 1.8 c) (see for example Tombros *et al.* [11]).

1.2.7 Non-local signals with tunnelling and transparent contacts

Takahashi and Maekawa [46] found an analytical formula which relates the jump of the non-local resistance, ΔR_{nl}, to the corresponding contact resistance in a non-local spin valve device (cf. fig. 1.8) with equal tunnelling barriers $R_1 = R_2 = R_B$. Its most general form is

$$\Delta R_{\mathrm{nl}} = 4R_G^s e^{-\frac{L}{\lambda_G}} \frac{\left(\frac{P_T \frac{R_B}{R_G^s}}{1-P_T^2} + \frac{P_F \frac{R_F^s}{R_G^s}}{1-P_F^2} \right)^2}{\left(1 + \frac{2\frac{R_B}{R_G^s}}{1-P_T^2} + \frac{2\frac{R_F^s}{R_G^s}}{1-P_F^2} \right)^2 - e^{-\frac{2L}{\lambda_G}}} \tag{1.11}$$

Here, P_T is the polarisation associated with the transport across the barrier and P_F the spin polarisation in the bulk of the ferromagnet (see section 1.2.1). R_B is the barrier (or, contact) resistance and $R^s_G = \lambda_G/(\sigma_G W)$ the spin resistance of graphene, i. e. the resistance within the range of its spin diffusion length λ_G. σ_G is graphene's sheet conductivity. Correspondingly, $R^s_F = \rho_F \lambda_F / A_J$ is the spin resistance of the ferromagnet, where A_J is the cross-section area of the $F/I/N$ junction and ρ_F the electrical resistivity. Since the spins decay quickly, only the volume defined by A_J and the spin diffusion length $\lambda_{G,F}$ are relevant for $R^s_{G,F}$. For diffusive transport, $\lambda = \sqrt{D\tau_s}$ (cf. section 1.2.3). These two quantities can be obtained from Hanle spin precession measurements (see section 1.2.8 below).

Since $R^s_F \ll R^s_G$, formula (1.11) reduces to

$$\frac{\Delta R_{\text{nl}}}{R^s_G} = 4e^{-\ell} \frac{\left(\frac{P_T}{1-P_T^2}\right)^2 \left(\frac{R_B}{R^s_G}\right)^2}{\left(1 + \frac{2}{1-P_T^2}\frac{R_B}{R^s_G}\right)^2 - e^{-2\ell}} \quad \text{where} \quad \ell := \frac{L}{\lambda_G} \tag{1.12}$$

ℓ is the ratio of spin transport channel length L and spin diffusion length λ_G. Two extremal cases can be distinguished in this relation:

For **transparent contacts**, i. e. $R_B \ll R^s_G$, (1.12) can be transformed to

$$\frac{\Delta R_{\text{nl}}}{R^s_G} \approx \frac{2P_T^2}{\sinh \ell} \left(\frac{R_B}{R^s_G}\right)^2 \tag{1.13}$$

Tunnelling contacts correspond to $R_B \gg R^s_G$. Since $0 < e^{-2\ell} < 1$, eqn. (1.12) simplifies to

$$\frac{\Delta R_{\text{nl}}}{R^s_G} \approx P_T^2 e^{-\ell} \tag{1.14}$$

Substituting graphene's spin resistance R^s_G into eqn. (1.14) yields the formula for the non-local resistance jump found in the literature (e. g. [47, 48]):

$$\Delta R_{\text{nl}} = \frac{1}{\sigma_G} \frac{P_T^2 \lambda_G}{W} e^{-\ell} \tag{1.15}$$

$$= R_G P_T^2 \frac{e^{-\ell}}{\ell}, \tag{1.16}$$

where eqn. (1.16) can be used for rectangular geometries. Note that R_G denotes the ohmic resistance of graphene in this equation.

1.2.8 Hanle spin precession

If the injected spins are subject to a magnetic field B_z perpendicular to the plane of graphene, they will start to precess about this field with the Larmor frequency

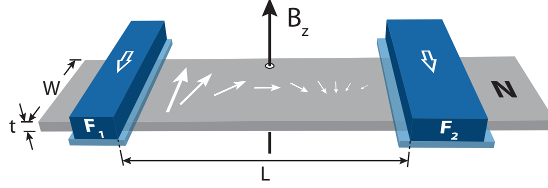

Figure 1.9: a) Spin precession for parallel contact magnetisation (hollow white arrows) and applied B_z field. Spin relaxation is symbolised by the varying size of the arrows. The measurement circuitry has been left out for clarity. In the sketch, W is the width of the spin transport channel, L its length and t its thickness.

$\omega_L = \frac{g\mu_B B_z}{\hbar}$, as sketched in fig. 1.9. The effect of this precession on the non-local signal can be described with the Hanle formula (cf. e. g. Tombros *et al.* [11]):

$$R_{\text{nl}}(B_z) = \pm \frac{DP_T^2}{\sigma_G W} \int_0^\infty \frac{1}{\sqrt{4\pi Dt}} e^{-L^2/(4Dt)} \cdot \cos(\omega_L t) \cdot e^{-t/\tau_S} dt \qquad (1.17)$$

This integral sums the trajectories of the diffusing and relaxing spins over all times. Its sign states if the initial magnetisation of the injected majority spins is parallel $(+)$ or antiparallel $(-)$. The first term of the integrand is a Gaussian accounting for the spin diffusion, the second term describes the actual spin precession by a cosine function and the third term is the exponential decay over time. Eqn. (1.15) follows from (1.17) by setting $B_z = 0$.

There exists an analytical equivalent [44, 47] to this formula which can be obtained when solving the Bloch equations in steady-state conditions [36]. In the form given in [44], the magnetisation in the y direction (cf. fig. 1.8) reads

$$V_{\text{nl}}(b,l) = \frac{1}{2} P_T^2 \frac{I_{\text{inj}}}{e^2 \mathcal{N}(E_F) A_{\text{sc}}} \sqrt{\frac{\tau_s}{2D}} F_1(b,l), \qquad (1.18)$$

$$\text{where} \quad F_1(b,l) = \frac{1}{f(b)} \left[\sqrt{1+f(b)} \cos\left(\frac{lb}{\sqrt{1+f(b)}} \right) - \right.$$
$$\left. - \frac{b}{\sqrt{1+f(b)}} \sin\left(\frac{lb}{\sqrt{1+f(b)}} \right) \right] e^{-l\sqrt{1+f(b)}}. \qquad (1.19)$$

$A_{\text{sc}} = Wt$ is the cross-section of the semiconductor of width W and thickness t. $b := \gamma B \tau_s = \omega_L \tau_s$ is the reduced magnetic field, $l := \frac{L}{\sqrt{2D\tau_s}} = \frac{L}{\sqrt{2}\lambda_G}$ the reduced injector-detector separation length and $f(b) := (1+b^2)^{1/2}$ [36, 44]. The *Einstein relation*,

$$\sigma_{\text{sc}} = \mathcal{N}(E_F) e^2 D_c, \qquad (1.20)$$

can be used in the denominator. As already mentioned in section 1.2.3, $D_c \approx D_s$ also holds true in graphene [37]. Using the sheet conductivity, e. g. in the case of graphene, eqn. (1.18) can be re-written as

$$R_{\mathrm{nl}}(b,l) = \frac{P_T^2}{2\sqrt{2}} \frac{\lambda_G}{\sigma_G W} F_1(b,l) \quad (1.21)$$

$$\overset{(1.15)}{=} \frac{\Delta R_{\mathrm{nl}}(B_z=0)}{2} \frac{e^{\sqrt{2}l}}{\sqrt{2}} F_1(b,l) \quad (1.22)$$

Eqn. (1.22) can be used to fit Hanle precession data. ΔR_{nl} is obtained from non-local spin-valve measurements or from the magnitude of $R_{\mathrm{nl}}(B_z = 0)$ from the corresponding Hanle curve.

The calculation of P_T from eqn. (1.21) assumes perfect tunnel barriers and requires the knowledge of the geometry of the spin transport channel (width W and length L) and the sheet conductivity σ_G of graphene.

1.3 Characteristics of graphene

This section introduces graphene and some of its unique properties. Parts of this section are closely following existing reviews about graphene [49–52].

1.3.1 Fabrication of graphene

Graphene is a crystalline allotrope of carbon, like diamond, graphite, carbon nanotubes and fullerenes. It is a planar material and its carbon atoms are arranged in a hexagonal lattice. Graphene is a monoatomic sheet of graphite and hence a two-dimensional material. It is often called *single-layer graphene*, SLG, to distinguish it from few-layer graphenes (FLG), such as *bilayer graphene* (BLG) or *trilayer graphene* (TLG), all of which have their own unique properties [9].

Due to graphite's layered structure – its layers are bound by weak van-der-Waals forces – graphene can be easily fabricated by mechanical exfoliation of graphite pieces using suitable tape and by pressing the cleaved graphite planes onto an SiO_2 substrate [8, 53]. Fig. 1.10 a) shows a thin graphene flake on SiO_2 produced with the exfoliation technique. Other methods for producing graphene are epitaxial growth on SiC and chemical vapour deposition (CVD) on suitable substrates such as Cu [54–56]. In the latter case, graphene needs to be transferred from the metallic growth substrate onto an insulating substrate [56, 57] for further processing.

Its low thickness and high mobilities make graphene a very interesting material for certain industrial applications, and several groups are exploring the mass production of graphene [58, 59]. However, a big issue in respect to applications is the absence of a band gap in natural graphene, preventing potential graphene transistors to be switched off. While several groups predicted the opening of a gap in graphene under certain curcumstances, e. g. when it is placed between two sheets of boron nitride [60], these predictions have not yet been experimentally verified.

1.3.2 Crystallographic properties of graphene

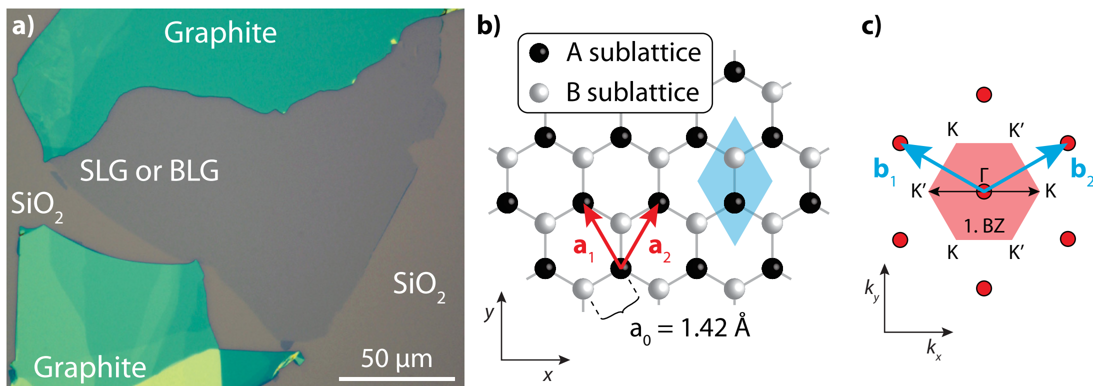

Figure 1.10: a) Contrast-enhanced optical micrograph of a large piece of exfoliated single- or bilayer graphene ("SLG or BLG": blueish area in the centre), surrounded by pieces of thin graphite (green), on an SiO_2 substrate. **b)** Sketch of graphene's honeycomb lattice as pair of two triangular sublattices A and B with the basis vectors $\boldsymbol{a_1}$ and $\boldsymbol{a_2}$. The basis vectors span a unit cell (blue rhombus). **c)** Reciprocal lattice of graphene with the basis vectors $\boldsymbol{b_1}$ and $\boldsymbol{b_2}$. The first Brillouin zone is coloured red, several crystallographic points are highlighted. The black arrows are vectors pointing to the K points (only two vectors are shown for clarity).

The C atoms in a graphene sheet are linked by strong covalent σ bonds, as in benzene. These bonds arise from the $2s$, $2p_x$ and $2p_y$ atomic orbitals of carbon which hybridise into three sp^2 orbitals with a bonding angle of 120°. Two overlapping sp^2 orbitals from neighbouring atoms create the covalent σ bonds which, due to their bonding angle, are responsible for the hexagonal arrangement of the carbon atoms, the *honeycomb lattice*, in a graphene sheet. The distance between two carbon atoms in the honeycomb lattice is a_0 = 0.142 Å (cf. fig. 1.10 b)). The remaining $2p_z$ orbitals of the individual carbon atoms are oriented out of the plane of graphene and form an additional, weak π bond. The π bonds create a delocalised electron system which extends over the whole graphene sheet. Two graphene sheets are bonded to each other by weak van-der-Waals forces, which is the reason for the easy cleaving technique.

A honeycomb lattice is not a Bravais lattice [52]: While two neighbouring carbon atoms, sketched in black and white in fig. 1.10, are equivalent in a chemical sense, they are different from a crystallographic point of view – the surroundings of the carbon atom sketched black in the figure is different from the white one. Graphene's lattice is described as triangular lattice with a two-atomic basis. The lattice vectors are $\boldsymbol{a_1}$ and $\boldsymbol{a_2}$.

Fig. 1.10 c) shows the reciprocal lattice with the vectors $\boldsymbol{b_1}$ and $\boldsymbol{b_2}$ and the first Brillouin zone (BZ). The most relevant high-symmetry points of the BZ are the Γ point at the centre of the BZ and two types of K points, denoted K and K', which are inequivalent, a consequence of the hexagonal lattice, because they cannot be connected by integer multiples of the reciprocal lattice vectors $\boldsymbol{b_i}$. Due to the lattice symmetry, all three K points are equivalent, as well as all three K'.

1.3.3 Electronic properties and minimum conductivity

The electronic properties of graphite were derived as early as 1947, using a tight-binding approximation with a Bloch wave ansatz in a two-atomic basis which accounts for the sublattices A and B [61, 62]. Mathematically, the sublattices are described with a spinor-like formalism for which the term *sublattice pseudospin* has been coined. A detailed derivation of the band structure of graphene can be found in [49, 52]. Taking only nearest-neighbour hopping into account, the dispersion relation reads

$$E_{\pm}(\boldsymbol{k}) = \pm t \left[1 + 4\cos\left(\frac{3a_0}{2}k_x\right)\cos\left(\frac{\sqrt{3}a_0}{2}k_y\right) + 4\cos^2\left(\frac{\sqrt{3}a_0}{2}k_y\right)\right]^{1/2}. \tag{1.23}$$

In this equation, t is the energy that an electron requires to hop from sublattice A to B (and vice versa). The conduction band π^* corresponds to the positive sign, the valence band π to the negative one. This dispersion relation is shown in fig. 1.11 a), and it is apparent that the π^* and the π bands touch at the K points of the Brillouin zone. In intrinsic graphene, which is not subject to external influences such as doping, the π band is filled and the π^* band is empty. Hence, the Fermi energy lies at the touching points, the *charge neutrality points* or *Dirac points* (see below). In this case, electrons require an energy of $t \approx 2.8$ eV to move between the two sublattices.

The K and K' points are the band maxima (minima) of the π (π^*) band, usually called *valleys*. Mathematically, the valley degeneracy of graphene is represented by another pseudospin, the *valley pseudospin*, sometimes called *isospin*. Goerbig [52] and Castro Neto *et al.* [49] provide further insight into these basic properties of graphene.

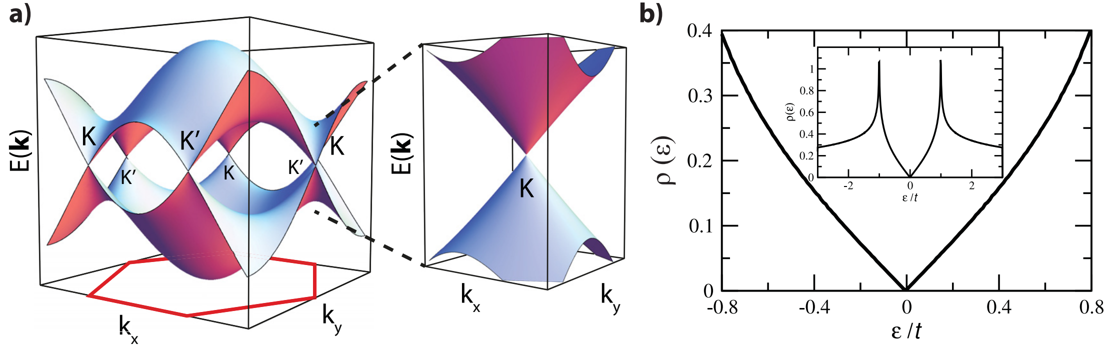

Figure 1.11: a) Band structure of single-layer graphene near the first Brillouin zone (sketched in red). The right panel shows a zoom on one of the Dirac cones. **b)** Graphene has a linear density of states (DOS) near the Dirac cones. The inset shows the DOS in the full energy range with van-Hove singularities at $E = \pm t$. $t \approx 2.8$ eV is the nearest-neighbour hopping energy. From [50].

In this thesis, we restrict to the low-energy properties of graphene, hence we can limit our analysis to the electronic structure near the K points: Let $\boldsymbol{K}$ be the location of the K point in the reciprocal space and $\boldsymbol{q}$ a small momentum vector $|\boldsymbol{q}| \ll |\boldsymbol{K}|$. For momenta $\boldsymbol{k} = \boldsymbol{K} + \boldsymbol{q}$ near the Dirac points, eqn. (1.23) can be Taylor-expanded which yields a linear dispersion relation of SLG near K:

$$E_{\pm}(\boldsymbol{q}) = \pm \hbar v_F |\boldsymbol{q}| + \mathcal{O}(q/K^2) \tag{1.24}$$

$v_F = \frac{3ta_0}{2\hbar} \approx 10^6$ m/s is the Fermi velocity. Eqn. (1.24) is valid for all K and K' points. This is the same dispersion relation as for relativistic mass-less particles given by the Dirac-Weyl equation [50, 51], attributing zero effective mass to graphene's low-energy conduction electrons. Many features in graphene's electronic structure related to the relativistic description bear Dirac's name.

The dispersion relation takes the form of cones near the Dirac points, commonly called *Dirac cones* (see fig. 1.11 a). Eqn. (1.24) does not show an energy gap and the density of states vanishes at the Dirac points (cf. fig. 1.11 b), hence graphene is classified as a zero-gap semiconductor. Eqn. (1.24) is identical for both K points. Since there are two K points (K and K' valleys) in graphene, its zero-energy states are *valley-degenerate* with a degeneracy of $g_v = 2$.

Experimentally, the charge carrier density can be tuned by gating (i. e., electrostatically doping) graphene. Chen *et al.* [63] found that chemical doping of graphene shifts the gate voltage which corresponds to the Dirac point. Although the density of states of graphene vanishes at the Dirac point, the conductivity of graphene is not zero, but rather seems to have a value of $\sigma(E_F) = 4e^2/h$ [9]. The ballistic limit of the conductivity is $\sigma(E_F) = 4e^2/(\pi h)$ [50], but it is not easy to reach this limit experimentally due to charge inhomogeneities [64]. In the literature, these are also referred to as *electron-hole puddles* and were experimentally observed by Martin *et al.* [65].

Very high mobilities of over 100,000 cm^2 V^{-1} s^{-1} have been reported for graphene by suspending the flakes (see e. g. [66] and [67]), or by choosing a suitable substrate: Dean *et al.* [68] report 60,000 cm^2 V^{-1} s^{-1} for graphene on hexagonal boron nitride. Together with graphene's low thickness, those would in principle be ideal prerequisites for graphene to replace silicon in electronics manufacturing. A major obstacle, however, is the fact that graphene does not have an intrinsic band gap, thus graphene-based transistors cannot be switched off.

1.3.4 Raman spectroscopy on graphene

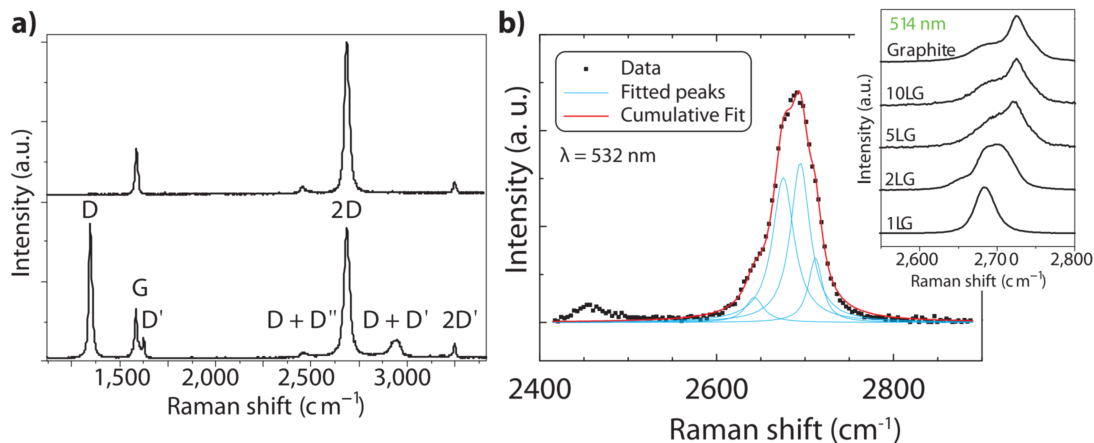

Figure 1.12: a) Raman spectrum of pristine (top) and defective (bottom) graphene with the corresponding peaks. Pristine graphene only shows the *G* and the *2D* peak. From [69]. **b)** Typical *2D* peak of bilayer graphene (own data, linear background subtracted). The peak can be fitted as superposition of four individual sub-peaks for every possible *K*-*K′* transition. The inset, taken from [69], shows the evolution of the *2D* peak with graphene's thickness from SLG to bulk graphite.

Raman spectroscopy is a non-invasive tool and the spectra of graphene are well understood [69–72]. Fig. 1.12 a) shows a typical spectrum for pristine graphene (upper spectrum) with clear *G* and *2D* peaks characteristic for graphene. The lower spectrum was recorded on damaged graphene. A clearly distinguishing feature is the existence of a prominent additional peak in the lower spectrum, the *D* peak, which is caused by additional phonon scattering events arising from defects. You *et al.* [73] found that the *D* peak can also be used to determine the edge chirality in graphene. Another defect-related signal is the much weaker *D′* peak, as well as all superpositions of *D* and *D′*.

Raman spectroscopy also allows to distinguish between monolayer and bilayer graphene by comparing the *2D* peaks: Single-layer graphene shows a narrow *2D* signal, whereas bilayer graphene has a wider *2D* peak which actually consists of four Lorentzians accounting for two-phonon scattering events (see fig. 1.12 b,

spectrum recorded with an incident laser beam of 532 nm wavelength) in the particular bandstructure of bilayer graphene [70].

1.3.5 Graphene's feasibility for spin transport

In addition to its remarkable electronic properties described in section 1.3.3, isolated intrinsic graphene promises to be an outstanding material for spin transport experiments. Two characteristic properties strongly decrease the influence of the four spin relaxation mechanisms compiled in section 1.2.4:

- The low atomic weight of carbon ($Z = 6$) causes a low spin-orbit coupling. Hence, the spin relaxation due to spin-orbit coupling will be low as well.
- The ^{12}C isotope of carbon has zero nuclear spin. Since about 1.1 % of natural carbon consists of the isotope ^{13}C which does have a nuclear spin, this amount will also be found in graphene and other carbon-containing compounds. However, this low content will not lead to a significant contribution from the hyperfine interaction to the spin relaxation.

Furthermore, the BAP mechanism is not the dominating spin relaxation mechanism in two-dimensional semiconductors [42] and should not be relevant for graphene. Hence, we expect a major contribution from the EY mechanism in graphene. Careful cleaning of the used graphene flakes should also minimise the EY contribution. The EY mechanism was found to be dominant in single-layer graphene, whereas the DP mechanism was the main spin relaxation contribution in bilayer graphene [74, 75]. Based on these considerations, graphene is expected to exhibit very long spin lifetimes, for example several microseconds in graphene quantum dots [76]. In graphene, the relaxation time T_1 and the dephasing time T_2 seem to be equal [11]. This allows us to specify τ_s as the general spin relaxation time in accordance with the literature.

Graphene's feasibility for spin injection was indeed shown some years ago [11] and a large number of experiments on graphene fabricated in different ways – exfoliated, CVD, SiC-grown etc – have been conducted since. Seneor *et al.* [10] recently published a review about the state of the art of graphene spintronics. So far, spin relaxation times τ_s close to 10 ns were published [41, 74, 75], but the reported values for τ_s are still far from theoretical expectations. This is briefly discussed in the following two sections.

1.3.6 Influence of substrate and adatoms

Ertler *et al.* [77] investigated the influence of the substrate on the spin relaxation in graphene, in particular charged impurities and polar-optical surface phonons.

Using Monte-Carlo simulations, they show that these contributions from the substrate would in fact limit the spin relaxation times to values between micro- and millisecons. This range of values can be seen as upper boundary for the experimental determination of τ_s of supported graphene.

In the same article, Ertler *et al.* estimated that spin-orbit coupling induced by adatoms can lead to spin relaxation times below 1 ns, depending on type and density of the adatoms. In-situ deposited Au [78] or Mg [79] adatoms, acting as charged impurities, did not significantly influence the spin relaxation. Similiar results were found when tuning the mobility of the charge carriers in graphene by using organic nanoparticles as charged impurities [80]. The amount of dopants did not play a significant role, but the spin lifetimes measured in this way were indeed found to be in a range of up to 2 ns [80]. Kochan *et al.* [81] found that magnetic impurities can account for a reduction of the spin lifetime as well. Hence, the existence of charged or magnetic impurities might partly account for the low spin relaxation times.

1.3.7 Influence of the contact resistance

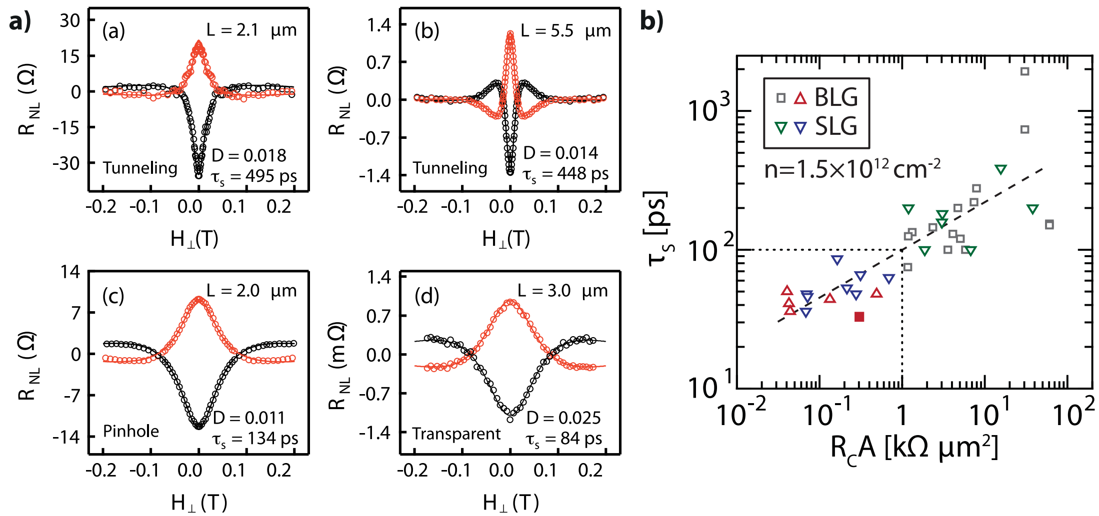

Figure 1.13: a) Several Hanle precession curves taken on spin-valve devices with barriers of various transparency. The spin relaxation time τ_s is considerably lower for the pinhole-dominated barrier and lowest for the transparent one. From [48]. **b)** The RA dependence of the spin relaxation time hints at a contribution of the contact to the spin relaxation. From [41].

A significant role arises from the contact resistances between the ferromagnet and graphene. Han *et al.* [48] investigated the role of the tunnel barriers at the contacts and distinguished spin valves with transparent, pinhole-dominated and tunnelling contacts. Several of their results are demonstrated in fig. 1.13 a)

which shows that the spin relaxation time τ_s for transparent contacts is lower than for tunnelling contacts. Maassen *et al.* [40] addressed the same problem and identified the effect of contact-induced relaxation to cause a modification of Hanle line shapes. Fits to these modified Hanle curves would yield lower spin relaxation times. However, τ_s is an intrinsic property of graphene and should not depend on extrinsic quantities.

Very recently, Volmer *et al.* [41] investigated the influence of the contact resistance in more detail and indeed discovered an explicit dependence of τ_s on $R_c A$, the resistance-area product of the tunnel barrier (see fig. 1.13 b). Their results illustrate that lower resistivities reduce the spin relaxation time. This is supprted by the long spin diffusion lengths of > 100 μm and long spin relaxation times > 100 ns reported by Dlubak *et al.* [82] which were measured in expitaxially-grown graphene on SiC with contact resistivities of about 1 MΩ.

1.4 Tunnelling

1.4.1 Tunnelling mechanisms in solids

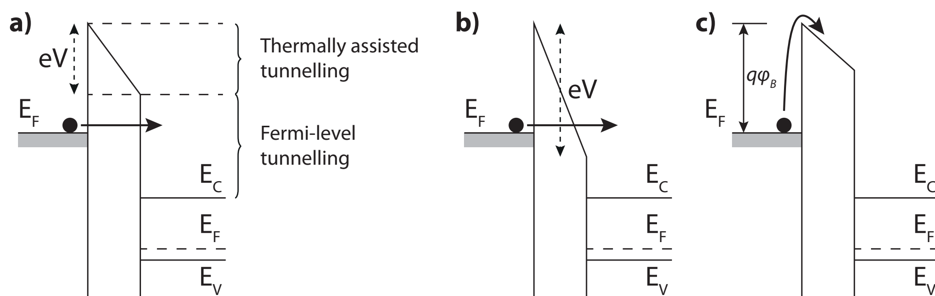

Figure 1.14: Conduction mechanism in solids. **a)** Direct tunnelling (from the Fermi level and thermally asisted); **b)** Fowler-Nordheim tunnelling; **c)** Thermionic emission. After [83] and [84].

This section gives a brief overview over the tunnelling mechanisms which are most relevant for our experiments.

- *Direct tunnelling*, relevant for small bias voltages, is an elementary quantum-mechanical phenomenon. Charge carriers can tunnel through finitely high and very thin barriers. If the system is under a bias eV, the barrier shape becomes triangular, as sketched in fig. 1.14 a and b. At finite temperatures, the energy distribution of electrons is thermally broadened and some of them have a sufficiently high energy to experience a lower barrier width ("Thermally assisted tunnelling" in the figure).

- The situation in 1.14 b) is called *Fowler-Nordheim tunnelling*. In this case, the externally applied bias eV is strong enough to decrease the width of the barrier through which the charge carriers have to tunnnel. This leads to an increased tunnelling probability and thus an increased tunnelling current. For higher temperatures, the tunnelling carriers have higher energies and thus see an even more reduced barrier thickness.

Although it is not a tunnelling process, *thermionic emission* (fig. 1.14 c) is mentioned here as well, because it is a very common mechanism which allows charge carriers to overcome a barrier. In thermionic emission, temperature and energy of the charge carriers cause electron emission which is described by the Richardson equation [83]:

$$J_n \propto T^2 \exp\left(-\frac{e\varphi_B}{k_B T}\right) \tag{1.25}$$

Plotting $\ln\left(\frac{I_{SD}}{T^2}\right)$ versus T^{-1} (*Arrhenius plot*) yields a straight line with a slope of $-\frac{e\varphi_B}{k_B}$, which allows to determine the barrier height φ_B.

1.4.2 Tunnelling vs. pinhole transport in electrical measurements

Åkerman *et al.* [85] formulated a set of criteria which allows to determine if the observed transport in a device is caused by tunnelling or by transparent regions (cf. fig. 1.15). These criteria were originally compiled for superconductor-insulating-superconductor (*S/I/S*) structures [86]. For non-superconducting electrodes, this set reduces to three relevant rules [85]:

- The conductance σ through a barrier decays exponentially with increasing barrier thickness d, i. e. $\sigma \sim \exp(-d)$
- Non-linear behaviour of $I - V$ or $dI/dV - V$ curves
- The barrier resistance increases weakly with decreasing temperature

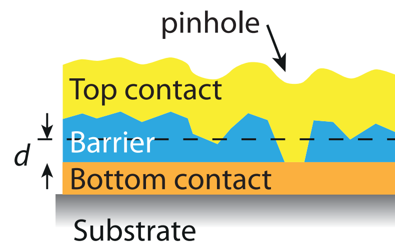

Figure 1.15: Illustration of the random growth of a barrier material (blue) which causes the contact material (yellow) to be in direct contact with

Åkerman *et al.* [85] showed that only the weak temperature dependence ultimately discerns tunnelling from direct transport, and that the other two criteria should be used with caution. They considered random deposition of insulating barrier material on a perfectly smooth metal surface. The random growth causes surface roughness which may leave parts of the metal surface beneath the barrier uncovered as illustrated in fig. 1.15. The spatial dependence of the insulator's thickness is Poisson-distributed. The probability to find pinholes in such a barrier, p_{short}, decays exponentially with its average thickness d, but the area A_{short} of this pinhole has the same dependence. Thus, the first criterion is not a unique signal for tunnelling.

With supporting experiments, Åkerman *et al.* could also show that non-linear behaviour of $I - V$ curves is not necessarily a signature of tunnelling either. Another group [87, 88] draws the same conclusion from their own measurements.

1.4.3 Tunnelling and pinhole signatures in spin transport

Han *et al.* [48] have found a way to determine if the transport through a tunnel barrier is dominated by pinholes. For transparent and pinhole-dominated contacts, the non-local magnetoresistance ΔR_{nl} more or less follows the conductivity of graphene, i. e. $\Delta R_{\text{nl}} \propto \sigma_G$, and is inversely proportional to σ_G for tunnelling contacts. This is essentially a consequence of eqn. (1.11), calculated in corresponding limits. The back-gate dependence of ΔR_{nl} can reveal this dependence. This offers the possibility to judge the quality of the tunnel barrier and can supplement the criteria from section 1.4.2 for spin-valve devices.

Chapter 2

Sample fabrication

This chapter briefly describes the steps to fabricate our samples. Our substrates are wafer pieces of degenerately doped silicon, which is used as gate electrode in our measurements. A 300 nm SiO_2 layer at the surface forms the gate insulator.

2.1 UV lithography

We first deposit a marker grid to facilitate the localisation of graphene flakes. A full 4" wafer is covered with a UV photoresist, either ma-N 415 (negative), ma-P 1205 (positive)[1] or AZ 1512HS (positive) [2], where the latter showed the best quality. The resist is irradiated with UV light (365 nm) through a mask holding the marker grid pattern in a mask aligner[3]. After developing, the grid is made by electron beam deposition (5 nm Ti, 35 nm Au) and the disc is cut into pieces of about 1.5 cm $\times$ 1.5 cm.

2.2 Graphene deposition

1. Sonicating in acetone and subsequent reactive ion etching (RIE) of the wafer pieces with the gold marker grid. The pieces are etched for five minutes in an argon/oxygen plasma with a power of 30 W and a gas pressure of 25 mTorr. The base pressure was at $5 \cdot 10^{-5}$ mbar.

2. Cleaving of natural graphite pieces[4] with wafer protection tape[5]. The freshly cleaved graphite is pressed onto the substrate immediately after etching

[1] both from MICRORESIST GMBH, http://www.microresist.de
[2] MICROCHEMICALS GMBH, http://www.microchemicals.com
[3] SÜSS MICROTECH, http://www.suss.com
[4] NGS NATURGRAPHIT GMBH, LEINBURG, GERMANY, http://www.graphit.de
[5] SPV 224P BY NITTO DENKO, http://www.nittoeurope.com

3. Tape removal in acetone, cleaning of the wafer piece in acetone and isopropanol and heating to 120°C for 30 minutes
4. In-situ cleaving by pressing a fresh piece of Nitto tape onto the wafer and removing without using solvents
5. Location and identification of suitable flakes in an optical microscope[6] and by Raman spectroscopy (see chapter 1.3.4)
6. If necessary, cutting graphene into ribbons using electron beam lithography for patterning and reactive ion etching to remove undesired graphene
7. Annealing in 20 sccm H_2 at 350 °C for 30 minutes or in high vacuum at 350 °C for several hours

The tunnel barriers were deposited in the subsequent step. Since we used different materials, Al_2O_3, MgO and MoS_2, which all required different approaches and fabrication processes, they are described separately: Al_2O_3 in chapter 3, MgO in 4 and MoS_2 in chapter 5.

2.3 Electron beam lithography

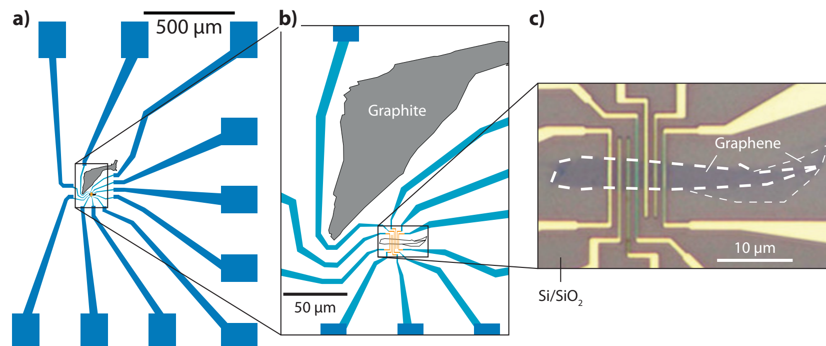

Figure 2.1: Graphene device with all-permalloy contacts. **a)** and **b)** show the structures for the bonding pads and leads, **c)** is an optical micrograph of the finished device which shows the permalloy electrodes (bright yellow) on top of the graphene flake (outlined). See also section 4.4.2.

After the deposition of the tunnel barrier material, the graphene ribbons received ferromagnetic contacts. We chose thin permalloy (Py) strips of 35 nm thickness which we defined by lithographically patterning an electron-beam-sensitive resist with a ZEISS SUPRA 40 electron microscope using the program ELPHY[7]. Initially, we used PMMA resist, but later changed to ZEP502A due to

[6] OLYMPUS AMERICA INC., http://www.olympus.com
[7] RAITH SOFTWARE GMBH, http://www.raith.com/

fabrication issues (see appendix A). Py is deposited by electron-beam evaporation from a NiFe target[8] in a UHV deposition system[9], typically at base pressures of 10^{-9} mbar. To improve lift-off, the sample is cooled during Py deposition. The permalloy strips were designed as rectangles with a length of about 12 μm in order to minimise their magnetic stray fields which can affect the magnetisation in an uncontrollable manner. The corners of these contacts, where the stray fields are predominant, were placed sufficiently far away from the graphene ribbon. We used different methods for the electrode fabrication:

- *Single-step lithography:* In some cases, the contact structures were designed in a single lithography step, which is a common method [37, 48, 75] and saves time. With this technique, all electrodes, leads and bonding pads fully consist of permalloy, and we introduced kinks of 90° into our structures to prevent random magnetic domain movement from the structures outside the strips (leads and bonding pads) into the electrodes (cf. fig. 2.1)
- *Multi-step lithography:* As an alternative, we also fabricated the rectangular ferromagnetic strips in a separate step and contacted them with a nonmagnetic material. With this technique, we aimed at achieving cleaner magnetic signals. This method also allowed us to use nonmagnetic contact pads and leads

The contact strips were designed in four different sizes (120 nm, 150 nm, 200 nm and 300 nm) which ensures distinct coercive fields (see fig. 1.3 and Aurich *et al.* [23]). Two-terminal measurements of the strip resistance in dependence of an external magnetic field B_z were conducted at temperatures below 4 K, either with a resistance bridge[10] or an in-house-built compensation circuit.

2.4 Final fabrication steps

All devices fabricated on a silicon wafer piece were checked for shortcuts or dead contacts with a needle-prober. The wafer piece was cut into small dice with dimensions of about 3mm by 3mm. These dice, sometimes carrying more than one device, were fixed in a chip carrier[11] using conductive silver to connect the highly-doped Si, which acts as back-gate, to the base plate of the carrier. Afterwards, back-gate and bonding pads were connected to the chip carrier's 20 contacts by microbonding with a wirebonder[12]. Afterwards, the chip carrier with the sample was mounted into a measurement cryostat.

[8] Goodfellow Cambridge Ltd./Goodfellow GmbH, `http://www.goodfellow.com/`
[9] BesTec GmbH, `http://www.bestec.de`
[10] AVS-47B by Picowatt, `http://www.picowatt.fi`
[11] Kyocera Fineceramics GmbH, `http://www.kyocera.de`
[12] Model 5332 BDA from F&K Delvotec GmbH, `http://www.fkdelvotec.com/`

2.5 Measurement and characterisation techniques

During fabrication, we characterised our graphene flakes using Raman spectroscopy, which is a non-invasive and quick method (see section 1.3.4). To this end, we used a confocal Raman microscope[13] with an incident laser wavelength of 532 nm. The recorded data were evaluated with the software WITEC PROJECT, shipped with the microscope.

The morphology of the tunnel barriers can be obtained with atomic force microscopy (AFM). Our results were recorded with a DIMENSION 3100 AFM[14], operated in tapping mode in order to minimise tip-sample contacts. We used suitable high-resolution tips[15] with a radius of < 10 nm for a pristine tip.

We performed most of our electrical measurements with the lock-in technique, using lock-in amplifiers[16]. These amplifiers have a built-in voltage source able to supply DC voltages up to ± 10 V and AC voltages up to 5 V. Several lock-ins can be coupled to operate with the same frequency. For finite-bias measurements and for back-gate tuning, we used DC voltage sources[17]. Measurements of DC voltages and currents were performed with a multimeter[18]. We used LABVIEW programs to control the measurement devices and to record our data.

Most of our measurements were taken in a ^{4}He system[19] equipped with two superconducting magnets which can be used to create a vector field in two spatial directions. This is particularly useful for spin precession measurements where one magnet is used to magnetise the contacts on our sample with one magnet and the other to probe the spin precession. The variable temperature insert which is part of the system allows for sample temperatures between room temperature and 1.4 K.

The coercive fields of our permalloy strips lie between 10 and 100 mT (see fig. 1.3). To make sure that the electrodes are fully magnetised before every measurement, we sweep the magnetic field to values between ± 500 mT and ± 1 T and leave it at this value for a few seconds. Subsequently, the field is reduced, usually to about 120 mT, and the actual sweep (e. g. between 120 mT and -120 mT) is started.

[13] WITEC GMBH, `http://www.witec.de`
[14] BRUKER CORPORATION, `http://www.bruker.com`
[15] Type PPP-NCHR by NANOANDMORE, `http://www.nanoandmore.com`
[16] SR830 by STANFORD RESEARCH SYSTEMS, INC., `http://www.thinksrs.com`
[17] YK7651 by YOKOGAWA ELECTRIC CORPORATION, `http://www.yokogawa.com`
[18] DMM-2000 by KEITHLEY INSTRUMENTS, `http://www.keithley.com`
[19] OXFORD INSTRUMENTS PLC, `http://www.oxford-instruments.com/`

Chapter 3

Al_2O_3 tunnel barriers

Aluminium oxide, Al_2O_3, is a very common choice for tunnel barriers in semiconductor spintronics and was reported to work in combination with graphene as well: Tombros *et al.* [11] used a tunnel barrier to inject spin-polarised electrons into graphene. Their findings led to a strong increase of activity in the field of graphene spintronics.

In order to create a tunnel barrier on graphene for their spin injection experiments, Tombros *et al.* deposited aluminium and oxidised it. Several challenges are connected with this method of fabrication:

- The aluminium layer might not be fully oxidised. Metallic clusters embedded in the barrier would effectively locally reduce its thickness or, in the worst case, act as transparent contacts to graphene. This reduces the amount of polarised spins through contact-induced relaxation (see section 1.2.3) and might lead to other effects such as local heating.
- Aluminium does not grow homogeneously on graphene which leads to the formation of transparent contact regions (pinholes). These will also decrease the total spin accumulation in graphene.

To ensure optimum spin injection and detection, it is desirable to fabricate aluminium oxide tunnel barriers on graphene which are homogeneously oxidised, are free of pinholes and have a uniform thickness. The thickness should also not be too high in order to still allow for tunnelling. A very well-suited method to create thin and homogeneous layers is *atomic layer deposition* (ALD). Section 3.1 describes this technique on the basis of the fabrication of our samples and gives details about the necessary pre-treatment of graphene before depositing the actual Al_2O_3 layer. A brief summary of the recipe is given in 3.1.4.

Sections 3.3 and 3.4 summarise the characterisation of our Al_2O_3 layers with AFM and $I - V$ or spin-valve measurements. With the help of AFM measurements, we can judge the morphology of the aluminium oxide barriers and obtain a first impression of their quality. $I - V$ measurements are another way to characterise our barriers, and spin-valve measurements will allow us to judge their spin injection performance. Here lies another requirement the oxide layers have

to meet: Their resistances should be lower than $\lesssim 1\ \text{M}\Omega$ so that we still can measure them with a reasonable signal-to-noise ratio.

Using Raman spectroscopy, we also investigated the influence of the aluminium oxide deposition on graphene. Our results are presented in section 3.3.4.

3.1 Al_2O_3 deposition on graphene

3.1.1 The trimethyl-aluminium/water process

In general terms, ALD allows the growth of conformous, thin oxides from precursor substances which are physisorbed or chemisorbed on the surface of a substrate in a self-terminating reaction [89, 90]. Here, we apply this method to our graphene flakes which are prepared as described in chapter 2.2. Our oxides are grown from the precursors trimethylaluminium (TMA, $Al(CH_3)_3$) and water in a SAVANNAH 100 ALD reactor[1]. The carrier gas is highly purified N_2.

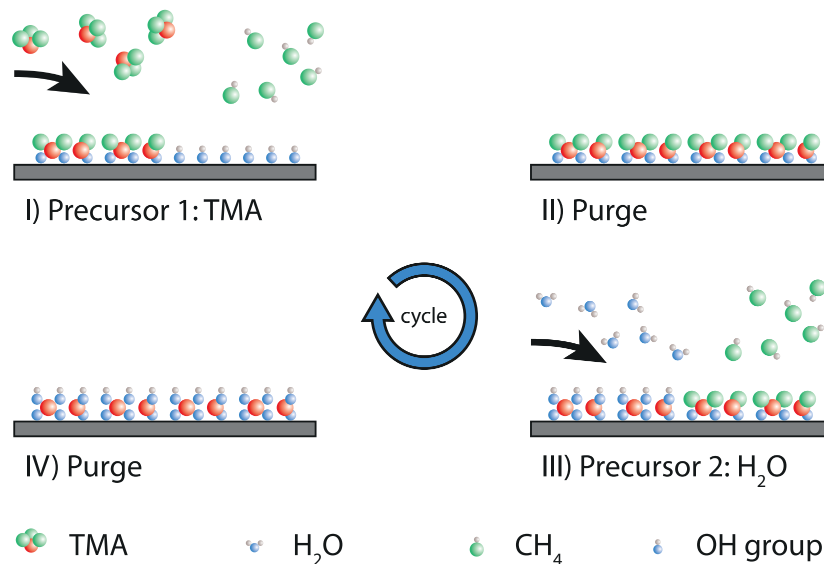

Figure 3.1: Sketch of an ideal Al_2O_3 deposition cycle (clockwise, starting from the top left image), taking place at the OH-terminated surface of a substrate (grey).

The process is described by the following chemical formula [90]:

$$2\text{Al}(\text{CH}_3)_3 + 3\text{H}_2\text{O} \longrightarrow \text{Al}_2\text{O}_3 + 6\text{CH}_4, \quad \Delta\text{H} = -376\text{kcal}.$$

The graphene flakes are placed in the ALD reaction chamber where they reside in a constant laminar flow of highly pure N_2 acting as carrier gas for the precursors.

[1] CAMBRIDGE NANOTECH INC., http://www.cambridgenanotechald.com/

The alumina layer is grown by repeating a reaction cycle of TMA and water at a temperature of 225 °C, following Farmer and Gordon [91]. Such a cycle consists of four steps (cf. fig. 3.1 a):

I) Deposition of TMA

II) Purging with N_2 to remove excess precursors and the side product CH_4

III) Injection of water which reacts with TMA according to the above formula

IV) Another purging step

Both reactants are injected into the reaction chamber by high-precision valves which can release a brief pulse of precursor gas of defined duration. The thickness of the alumina layer depends on the number of cycles and on the growth mode of aluminium oxide on graphene. Note that our Al_2O_3 layers are not patterned but cover the full wafer piece with the graphene flake.

3.1.2 NO_2 functionalisation of graphene

Graphene has a highly inert surface, resulting from the sp^2 bindings of the carbon atoms (see chapter 1.3.2), which makes the deposition of oxides on its surface generally difficult and requires a seeding or functionalisation step prior to the oxide growth. Several growth promotion processes were proposed, among them NO_2 functionalisation [91], O_3 treatment [92] or PTCA coating [93, 94]. We chose NO_2 functionalisation, because it can easily be integrated into our ALD process, and we expect it to be the least damaging of these methods.

Farmer and Gordon [91] published a recipe for the deposition of an NO_2-TMA seeding layer on suspended carbon nanotubes. The nanotubes were functionalised with NO_2 to create nucleation sites to which the TMA molecules can dock. A single cycle of this recipe consists of the following steps:

I) Deposition of gaseous NO_2

II) Purging with N_2

III) Deposition of TMA

IV) Another purging step

NO_2 and TMA must be deposited at room temperature, since NO_2 desorbs easily at higher temperatures [91]. Fig. 3.2 shows a schematic drawing of one cycle of the NO_2 functionalisation process. 50 of these cycles are repeated to ensure a thorough wetting of the graphene flake's surface.

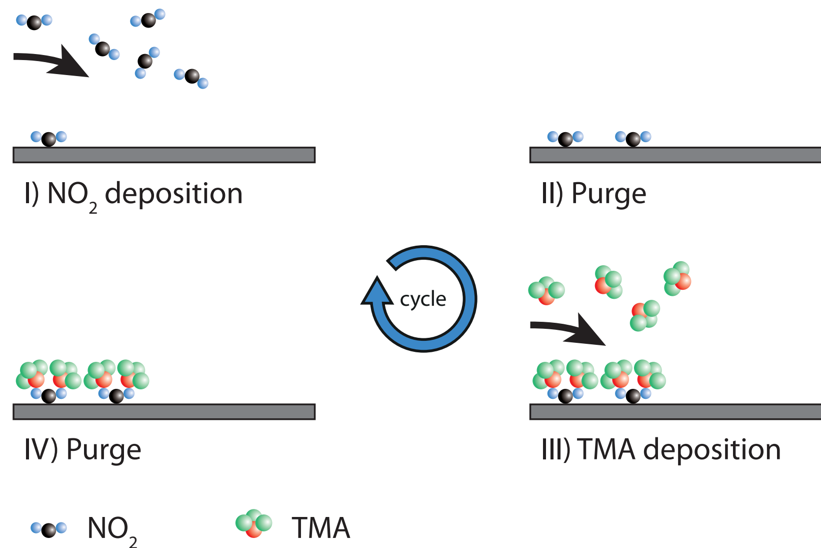

Figure 3.2: Sketch of a cycle (clockwise, starting from the top left image) of the self-terminating NO_2 deposition process of Al_2O_3 on graphene as proposed in Farmer and Gordon [91], originally used for carbon nanotubes. The sketch reflects the low yield of a single NO_2 deposition cycle.

To avoid NO_2 desorption during the growth of the aluminium oxide layer which takes place at 225 °C, we create an extra capping layer on the NO_2/TMA nucleation sites at room temperature [91] which consists of a thin (5 cycles) Al_2O_3 layer, grown with the TMA/water recipe (section 3.1.1). In our case, the growth temperature was 55 °C, the lowest possible temperature in the ALD system. The temperature is then increased to 225 °C and the final TMA/water cycles for the alumina layer deposition are executed. This NO_2-based recipe was e. g. used for graphene by Williams *et al.* [95] to grow a gate insulator on graphene.

3.1.3 TiO_2 functionalisation of graphene

We also tried a different method, following Wang *et al.* [96] who used a submonolayer of TiO_2 as seeding layer for the growth of smooth MgO tunnel barriers on graphene. We tried to adapt their approach for improving the growth of Al_2O_3: A submonolayer (about 1.2 Å) of Ti is deposited onto graphene in UHV at -35 °C. The Ti layer is oxidised in air at 120 °C for 13 hours after deposition. The Al_2O_3 layer is grown in the ALD machine as before, during 5 cycles at 55 °C and three cycles at 225 °C. Fallahazad *et al.* [97] also investigated this method with the aim of creating a thin gate dielectric on graphene.

3.1.4 Summary of the ALD recipes

The two recipes used for our Al_2O_3 layers are as follows:

Recipe 1:

1. Functionalisation with NO_2 and TMA during 50 cycles at 55 °C
2. Capping by five cycles of Al_2O_3, grown at 55 °C
3. Growing Al_2O_3 from TMA and water at a temperature of 225 °C in a varying number of cycles ("high-temperature cycles")

Recipe 2:

1. Deposition of a Ti submonolayer at -35 °C and oxidation to TiO_2
2. Capping by five cycles of Al_2O_3 growth at 55 °C
3. Growing Al_2O_3 from TMA and water at a temperature of 225 °C in a varying number of cycles ("high-temperature cycles")

3.2 Characterisation of directly deposited aluminium oxide

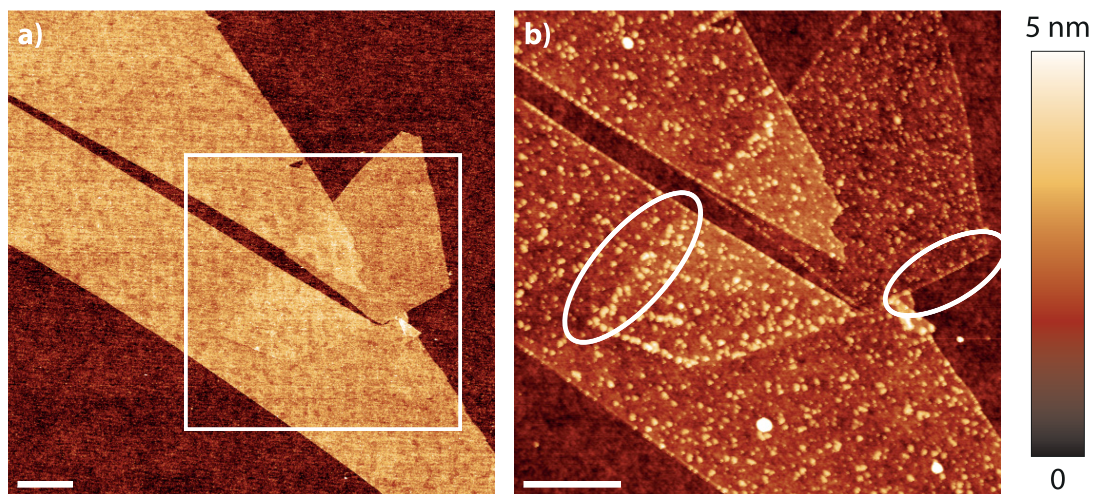

Figure 3.3: a) Bare graphene flake before ALD. The faint interference fringes on graphene are an artifact of the AFM. The scale bar in both AFM images represents 1 μm; **b)** Close-up of the marked section in a) after ALD without functionalisation. Seeding was omitted to demonstrate the growth of the oxide at defects and step edges. A few of these regions are highlighted by the ellipses.

As a first test, we directly deposited 10 high-temperature cycles of ALD onto a graphene flake (see AFM image fig. 3.3 a) without applying any seeding method. In agreement with the literature, we find that it is not possible to deposit TMA onto bare graphene due to its inert nature [93, 98]. Fig. 3.3 b) shows that alumina has preferentially grown at the edges of the graphene flake, or at defects. This preparation method is not suitable for the fabrication of tunnel barriers.

3.3 Characterisation of the Al_2O_3 layers with NO_2 functionalisation

3.3.1 Fabrication

The graphene flakes were prepared as described in chapter 2.2. For depositing the NO_2-seeded Al_2O_3 layers, we used recipe 1 (see section 3.1.4) and varied the number of high-temperature ALD cycles: Since we planned to characterise the barriers with $I - V$ measurements, we tried to cover a broad range of contact resistances by producing samples with different Al_2O_3 thicknesses. The number of high-temperature cycles varied from 20 to 3.

3.3.2 Estimation of the thickness

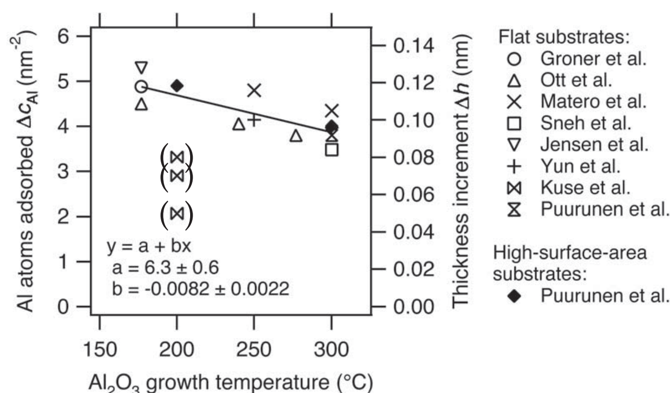

Figure 3.4: Temperature dependence of the parameter Δc (growth per cycle) from several values reported in the literature. The graph legend shows the sources of these values as references in Puurunen [89] from where the figure was adopted. The values which were disregarded for fitting are put in parentheses.

It is useful to convert the number of cycles into an actual thickness value. The most direct way to determine the thickness would be to pattern the oxide layer and measure the step height, e. g. with AFM. Lithographical patterning is not

possible in our case, since the temperature of the growth process is too high for typical resists. Resist residues sticking to the oxide layer or the substrate could influence a thickness measurement. Shadow-masking can easily lead to edges which are too smooth and wide for the AFM. The low thickness of the oxide layer in combination with its roughness prevents the use of other methods such as using a step profiler.

One can obtain a first-order approximation of the thickness from a growth model of ALD-Al_2O_3 developed by Puurunen [89, 99]: The model contains a parameter

$$\Delta c = \Delta h \rho N_A M^{-1} \tag{3.1}$$

("growth per cycle") which represents the amount of aluminium atoms (in the compound of $AlO_{1.5}$) deposited per surface area and ALD cycle. Δh is the oxide layer thickness per cycle, $\rho = 3.5 \cdot 10^{-21}$g nm^{-3} the bulk density of $AlO_{1.5}$ and $M = 50.98$g mol^{-1} its molecular weight. Fig. 3.4 from [89] shows a linear fit to several values of Δc at various process temperatures reported in the literature. From this, one can extract $\Delta c = (4.5 \pm 0.8)$ nm^{-2} at 225 °C. Using eqn. (3.1) and assuming layer-by-layer growth, it is possible to deduce a value of (1.1 ± 0.2) Å per cycle. The errors were calculated from the values provided in the figure. The errors of temperature T and density ρ were assumed to be much lower and thus have been omitted.

There is no data available from [89] for temperatures lower than 150 °C. By linearly extrapolating the fit to lower temperatures, one obtains $\Delta h = 1.4$ Å per cycle for the deposition at 55 °C. We always create a capping layer with five ALD cycles at room temperature which would correspond to (7.1 ± 0.3) Å of aluminium oxide if layer-by-layer growth is assumed. The total thickness $t_{\mathrm{ox}}$of the oxide layer after n cycles amounts to

$$t_{\mathrm{ox}} = 7 \text{ Å} + n \cdot 1.1 \text{ Å} \tag{3.2}$$

3.3.3 AFM measurements

Atomic force microscopy (AFM) can provide valuable informations about surfaces, e. g. topography and roughness R_q. This allows us to determine if the surface roughness depends on the oxide layer thickness. Fig. 3.5 shows AFM images of graphene flakes covered with the thickest and the thinnest Al_2O_3 layers in our study. The R_q values in dependence of the number of ALD cycles and the estimated thickness are plotted in fig. 3.6.

Figs. 3.5 a) and b) show two AFM images from the same flakes on sample ALD-1. The alumina layer was grown with recipe 1 with 20 high-temperature cycles on the graphene flakes, one of which has thick and thin regions. The thin parts of the graphene flakes are single- or bilayer graphene, given by optical microscopy.

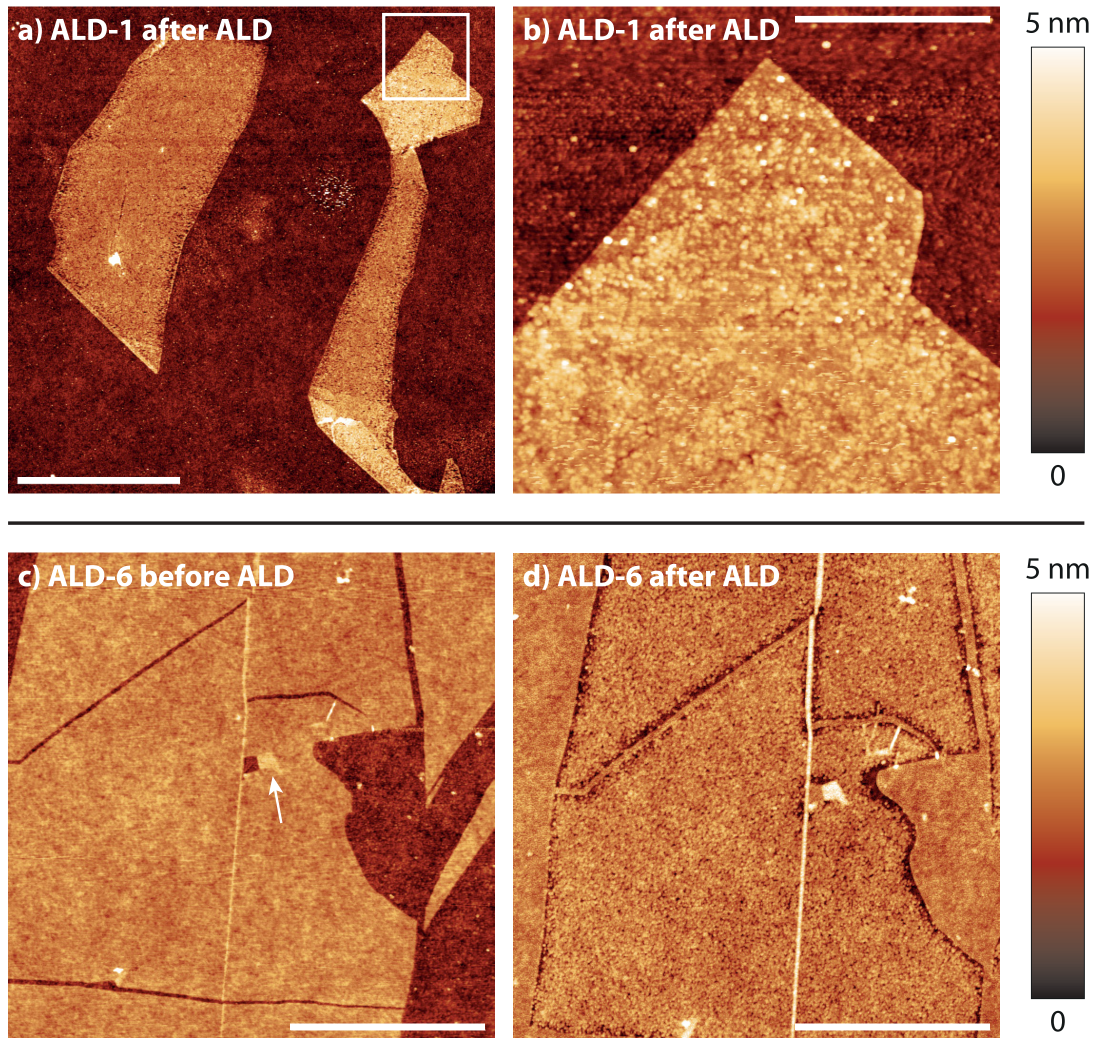

Figure 3.5: AFM images of graphene flakes with the thickest (a, b) and thinnest (c, d) Al_2O_3 layers. **a)** Graphene flake on sample ALD-1 after 25 ALD cycles (5 at 55 °C and 20 at 225 °C). The scale bar corresponds to 5 μm. **b)** Close-up of the marked area in a). The scale bar represents 1 μm. **c), d)** Annealed graphene flake on sample ALD-6 before and after the ALD process. The arrow in a) marks a piece of graphene which is folded back. In both figures, the scale bar is 2 μm.

Sample	cycles	est. thickness	R_q on graphene	R_q on SiO_2	fig.
ALD-1	25	28.6 ± 0.9 Å	0.50 nm	0.34 nm	3.5 a), b)
ALD-5	20	23.2 ± 0.8 Å	0.32 nm	0.34 nm	-
ALD-2	15	17.9 ± 0.7 Å	0.57 nm	0.44 nm	-
ALD-4	10	12.5 ± 0.5 Å	0.43 nm	0.43 nm	-
ALD-6	8	10.3 ± 0.5 Å	0.56 nm	0.40 nm	3.5 c), d)
ALD-8	5	7.1 ± 0.3 Å	0.63 nm	0.85 nm	-

Table 3.1: Alumina layer thicknesses and RMS values for different samples coated with ALD-Al_2O_3. Each given number of cycles includes the five growth cycles at 55 °C. All thickness values and errors were calculated from the estimate in section 3.3.2. The rms values are extracted from AFM measurements, e. g. fig. 3.5.

It is clearly visible in the AFM image that the oxide layer is very inhomogeneous along the edges of the thin parts of graphene. The measurements show a root-mean-square (rms) roughness of 0.50 nm on these parts of the flake. It also seems that the coverage of the thick graphene flake is more continuous than of the thin flake, especially along the edges.

In the case of thinner Al_2O_3 layers, as shown in fig. 3.5 c) and d) for sample ALD-6, the coverage of the flake is even less homogeneous, especially at the edges. This is also reflected by the rms values (0.56 nm for the Al_2O_3-covered flake and 0.4 nm for the covered substrate) which differ visibly from the values for the uncovered flake and substrate (black and red diamonds in fig. 3.6) taken previously.

Figs. 3.5 a) and b) also reveal that the oxide on the graphene flakes is above the Al_2O_3-covered areas of the substrate. In fig. 3.5 d), the Al_2O_3-covered graphene is not clearly above the substrate. Both flakes presented in fig, 3.5 are single- or bilayer graphene. This indicates that the aluminium oxide grows similarly fast on graphene and SiO_2. The oxide on graphene shows a very grainy structure which may be caused by wetting problems during the growth.

Table 3.1 sums up several roughness values measured with AFM on samples with different alumina thickness which are also presented in fig. 3.6. For the samples ALD-4 and ALD-6, roughness values before and after deposition are available and are plotted for comparison (hollow symbols in the figure). There is a certain variation of the roughness which could indicate that the preparation of our layers is not very reproducible. On the other hand, AFM tips tend to pick up material which essentially changes the tip radius. This also has an influence on the measured roughness. Altogether, we can conclude that there is no clear correlation between roughness and the amount of ALD cycles. With (0.54 ± 0.10) nm, the mean roughness of these samples is quite high.

Further lowering the thickness by leaving out the high-temperature ALD steps altogether creates layers with a much higher roughness (sample ALD-8, see table 3.1 and fig. 3.6). The estimated thickness of the oxide is 7 Å (cf. section 3.3.2). Such a thin and rough layer is very likely to contain pinholes.

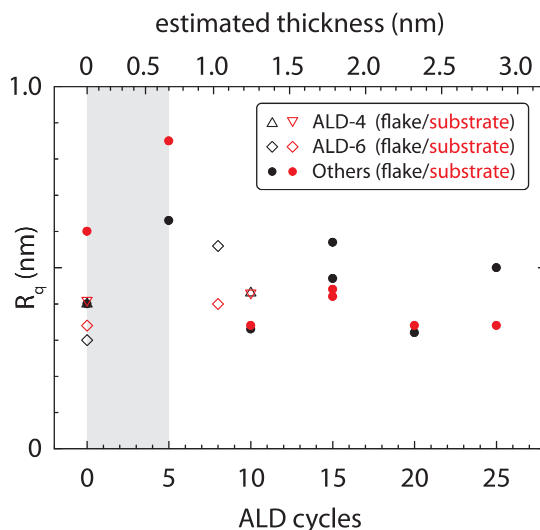

Figure 3.6: RMS roughness R_q vs. cycles/thickness of several flakes and their substrates which were coated with Al_2O_3 using recipe 1 (filled circles). For the samples ALD-4 and ALD-6, rms values for bare and alumina-covered flakes and substrates have been plotted separately (hollow triangles and diamonds). The shaded region corresponds to the low-temperature cycles (note the different scale for the estimated thickness below 7 Å). Some of these values are also compiled in table 3.1.

3.3.4 Quality of graphene below NO_2-Al_2O_3

It is crucial to learn about the impact which the deposition of aluminium oxide has on graphene. Raman spectroscopy (see chapter 1.3.4) offers the possibility to judge the quality of graphene below the alumina layer in a non-destructive way. Fig. 3.7 shows the Raman signals taken on a graphene flake before and after covering with Al_2O_3 (8 cycles with recipe 1). The Raman spectrum was created by shining a laser with a wavelength of 532 nm and a power of 2 mW onto the surface.

The *D* peak is absent in the spectrum recorded after the ALD process in the bulk of graphene (red curves in panels b and c of fig. 3.7). However, there is a certain region in which the height map of the *D* peak (panel d) displays a high intensity. This resulted from accidentally scratching graphene with an AFM tip before the spectrum was taken. We did not observe *D* peaks in our other, undamaged NO_2-Al_2O_3 graphene samples and conclude that the ALD process does not introduce defects to graphene, in contrast to sputtering of Al_2O_3 [100].

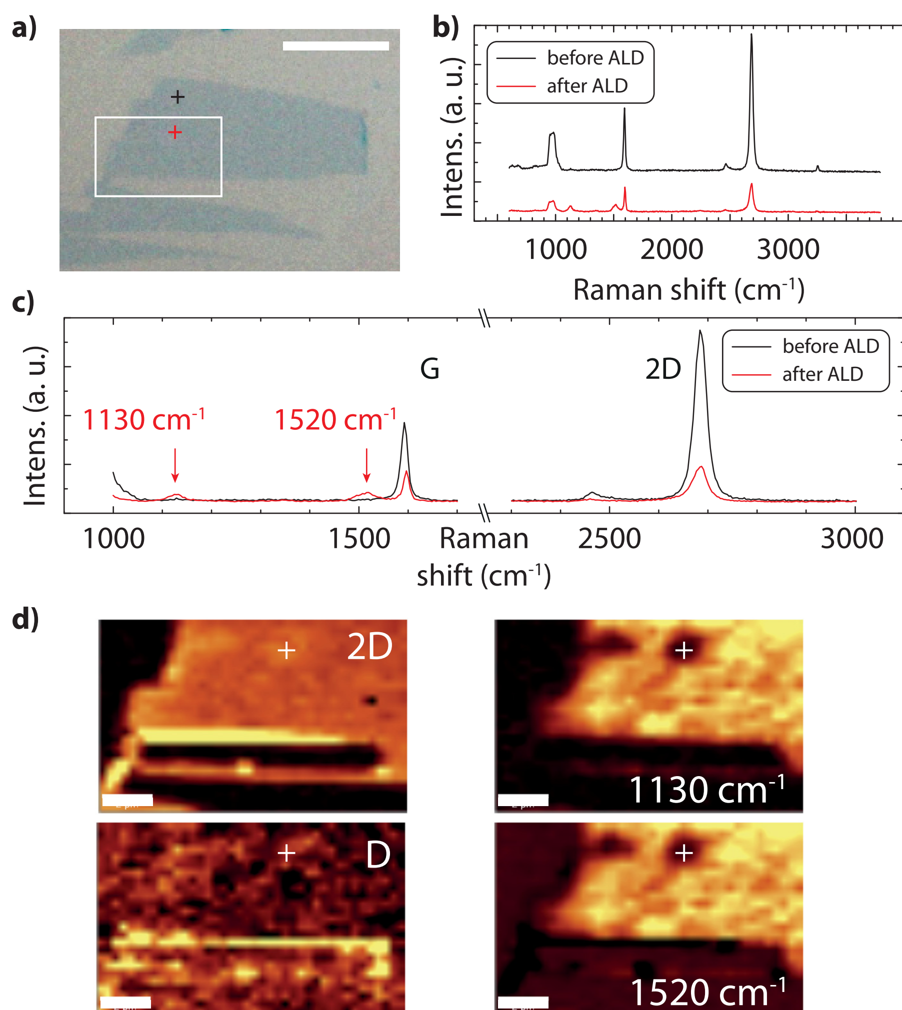

Figure 3.7: a) Photography of the freshly cleaved graphene flake, the scale bar corresponds to 10 μm. The marked area was investigated with Raman spectroscopy. The colours of the crosses correspond to the spectra in b) and d) and show their location on the flake. **b)** Comparison of full Raman spectra before and after Al_2O_3 deposition from nearby spots on the flake. For clarity, the red curve is plotted with an offset. **c)** Zoom of the data after the ALD process. **d)** Height maps of the *2D*, *D* and the unknown peaks of graphene after the ALD process. The bright features in te *D* map show damaged graphene. The height maps for the unknown peaks in b) are almost identical. The dark spots in these height maps show where the laser hit the surface. The crosses show where the red spectral curves in b) and d) were recorded. All scale bars represent 2 μm.

A few Raman spectra showed additional peaks, such as those at 1520 cm^{-1} and 1130 cm^{-1} in the red spectrum in fig. 3.7. Their origin is unclear, but they always appeared together with the peaks of graphene and never on silicon. Closer inspection revealed that the new peaks behave identically: Their height maps shown in fig. 3.7 a) are essentially the same. These maps also exhibit darker areas which are spots where the Raman laser had hit the surface in previous measurements. It is possible that the new peaks are caused by organic dirt or even the oxide layer itself which was heated by the laser and burnt off prior to measuring. A slightly brighter area in the height map of the *2D* peak around the cross and 2μm left of it coincides with the dark spots in the 1530 cm^{-1} picture.

Fig. 3.7 c) also shows that the *G* peak of graphene shifted to slightly higher energies by about 5 cm^{-1}, corresponding to 0.6 meV. This was probably caused by heating with the laser.

3.3.5 $I - V$ measurements

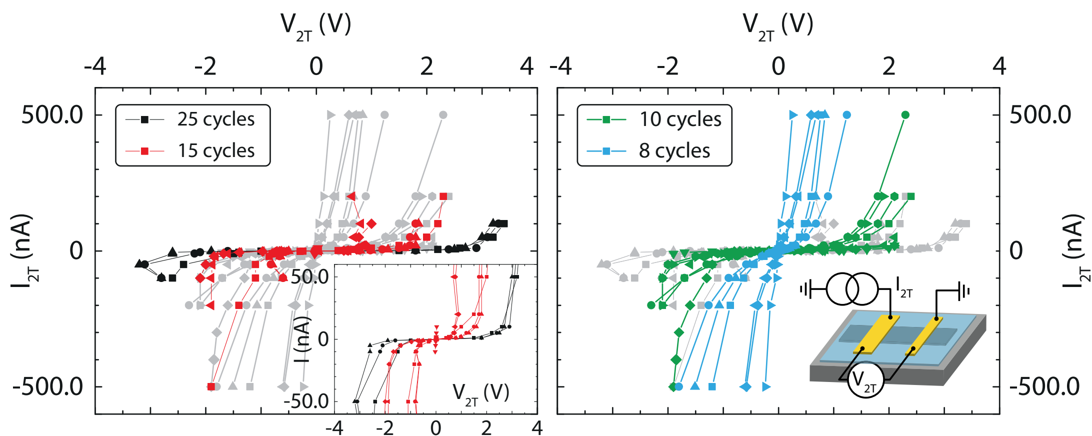

Figure 3.8: Sets of $I(V)$ curves for different numbers of ALD cycles. For clarity, both panels show the same curves with a different pair of datasets highlighted in each graph. The inset in the left panel is a zoom of the data to illustrate the low current around zero volts. The inset in the right panel shows a sketch of the sample and the measurement scheme.

Since the electrical resistance of our barriers should not exceed 1 MΩ, we prepared several graphene flakes with varying alumina thicknesses (cf. table 3.1) and deposited contacts of 5 nm Ti and 35 nm Au by electron beam evaporation. The contacts were defined by standard electron-beam lithography techniques using a bilayer resist (200 nm PMMA on 90 nm MA). To realise a clean graphene-Al_2O_3 interface, we chose to deposit the oxide layer directly after cleaving and cleaning the graphene flakes instead of lithographically patterning it, since this would have left undesired resist residues on the surface. Hence, the oxide layer

fully covered the wafer. As a consequence, there were no direct contacts to graphene (cf. right panel in fig. 3.8 a and fig. 3.9 a below).

We conducted $I-V$ measurements on samples with varying ALD layer thicknesses using a KEITHLEY 2400 SOURCEMETER we used to supply a bias current to the sample and to measure the voltage drop over the barrier. The results are compiled in fig. 3.8, where every $I(V)$ curve represents a two-terminal measurement on a different junction. The colours correspond to the number of ALD cycles performed on the sample and are thus related to the alumina thickness.

On the samples with thicker ALD layers (black and red curves), we observed several signs for barrier breakthroughs. All samples displayed a linear $I(V)$ dependence near zero current and a non-linear dependence for higher bias. This is a well-known behaviour in tunnelling [101, 102]. The blue curves in fig 3.8, corresponding to eight ALD cycles, show this most clearly. With linear fits to these curves near zero, we calculated the resistance-area products $R \cdot A$ of our tunnelling contacts (see fig. 3.9 b) below).

3.3.6 Resistance-area product for two barriers in series

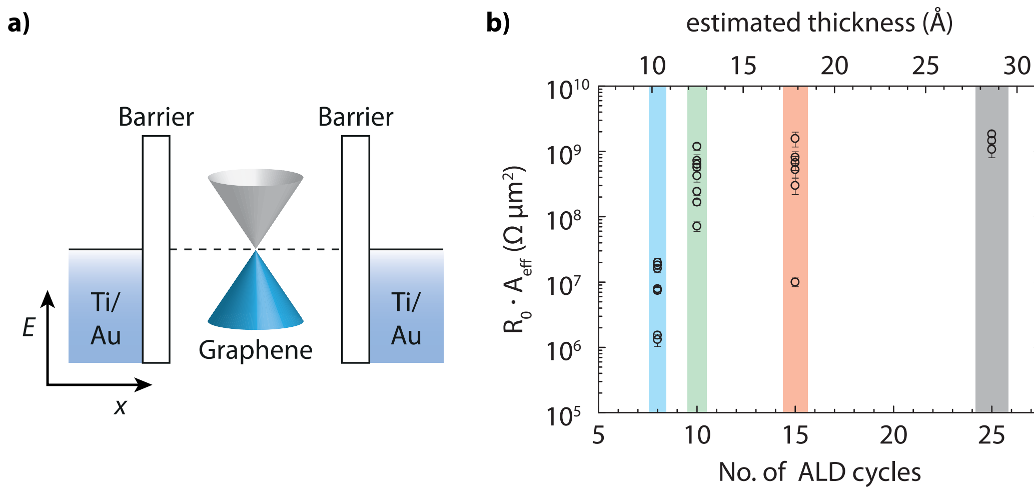

Figure 3.9: a) Sketch of the electronic structure of graphene between two ideal tunnel barriers contacted by Ti/Au electrodes. **b)** Resistance-area products extracted from the $V(I)$ curves in fig. 3.8 around zero volts. The shaded rectangles represent the error of the thickness estimate, their colours correspond to the number of cycles. The error bars resulted from the linear fits to the resistances.

In the case of a perfectly homogeneous oxide layer, all contact resistances scale with the area of their cross-section with graphene below the barrier. This can be verified by calculating their resistance-area product. All contacts are on top of the alumina layer and there is no direct contact to graphene. There is a possibility

to calculate an RA product of two barriers in series (cf. fig. 3.9 a): The total measured resistance R_{2T} can be expressed as the sum of graphene's resistance and the two barrier resistances R_1 and R_2, which depend on the cross-section area of their contact with graphene. We focus on the regime around zero bias and use the index "0" for the resistance to emphasize that the quantities used below are only valid in this regime. The total resistance near zero bias is

$$R_0 = R_1 + R_{Gr} + R_2 \tag{3.3}$$

For low applied voltages, the tunnelling current density j_B through a barrier of area A_B is proportional to the applied bias V_B, as derived in eqn. (24) in [102]:

$$j_B = V_B \cdot \underbrace{\frac{\sqrt{2m_e\bar{\varphi}}}{\Delta s}\left(\frac{e}{h}\right)^2 \exp\left[-\frac{4\pi\Delta s}{h}\sqrt{2m_e\bar{\varphi}}\right]}_{=:C_0} \tag{3.4}$$

The proportionality constant C_0 contains the free electron mass m_e, the mean zero-voltage barrier height $\bar{\varphi}$ and the barrier thickness Δs as parameters. We have observed the same $I \propto V$ behaviour for low bias currents in our samples and can thus express the resistance of the ith barrier as:

$$R_i = \frac{V_i}{j_i A_i} = \frac{1}{A_i C_0}, \tag{3.5}$$

Substituting (3.5) into (3.3) yields the resistance-area product of the barrier series:

$$(R_0 - R_{Gr}) \cdot A_{eff} = \frac{1}{C_0}, \quad \text{where} \quad A_{eff} := \frac{A_2 A_1}{A_2 + A_1}. \tag{3.6}$$

By linearly fitting the $I - V$ curves of fig. 3.8 close to zero, we could extract ohmic resistances R_0 for every two-terminal measurement. All these resistances lie in a range between 350 kΩ and 20 MΩ, hence it is safe to neglect graphene's resistance in the formula:

$$R_0 \cdot A_{eff} = \frac{1}{C_0}. \tag{3.7}$$

With the contact area extracted from SEM images or lithography designs we calculate the resistance-area products $R_0 A_{eff}$ of the two barriers in series. These values are plotted versus the estimated layer thickness in fig. 3.9 b) and compiled in table 3.2. The resistance values seem to saturate at about 1 GΩ, which is most probably an artifact of the used KEITHLEY SourceMeter: Because of the low number of data points, we underestimate R at higher layer thicknesses.

We observe that the values for $R_0 A_{eff}$ are spread more or less over an order of magnitude for all Al_2O_3 layer thicknesses, except for the case of 25 cycles. For

Sample	cycles	Contact	area	Sample	cycles	Contact	area
ALD-1	25	1	2.0 μm	ALD-2	15	2	2.0 μm
	25	17	2.0 μm		15	3	2.9 μm
	25	18	1.5 μm		15	5	7.6 μm
ALD-4	10	3	2.6 μm		15	7	2.5 μm
	10	5	3.6 μm		15	10	8.1 μm
	10	7	1.9 μm		15	17	6.0 μm
	10	10	2.4 μm	ALD-6	8	11	6.0 μm
	10	12	2.9 μm		8	15	10.0 μm
	10	15	2.4 μm		8	16	6.0 μm
	10	17	6.1 μm		8	17	6.0 μm
	10	18	2.4 μm		8	19	1.0 μm

Table 3.2: Contact areas of several ALD samples. The resistances shown in fig. 3.3.5 were measured on these contacts. The areas shown here were used to calculate the resistance-area products in fig. 3.9.

perfectly homogeneous barriers, these values would be identical. This is a clear sign that the barriers vary from contact to contact. A few of these values are very low, for example on the samples with 10 and 8 ALD cycles. This could hint at pinholes – section 3.3.7 presents further analysis for the sample with 8 cycles. We conclude from these values that our barriers are generally inhomogeneous which, especially in the case of the thinner layers, increases the risk for pinholes.

3.3.7 Temperature dependence of the $I - V$ measurements

As explained in chapter 1.4.2, only the temperature dependence of the tunnel resistance can distinguish tunnelling from pinhole-dominated transport. We focus on sample ALD-6 (8 cycles, recipe 1), since it is the only one which showed suitable resistance values in the MΩ range. $I - V$ measurements were recorded for various temperatures down to 4 K in a ^{4}He cryostat with a variable temperature insert. The voltage is supplied from a DC voltage source[2] and the current is measured with a Keithley 2000 multimeter in combination with an in-house-built IV converter. A coloured SEM image of the graphene device with the measurement circuit is presented in Fig. 3.10 a).

We extracted resistance values from the $I - V$ curves of three different junctions at different temperatures by linearly fitting the data close to zero bias. Following [85], we normalised them with their respective room-temperature values (cf. section 3.3.5) and plotted them in fig. 3.10 b). All of these resistances show an

[2] YK7651 from Yokogawa Electric Corporation

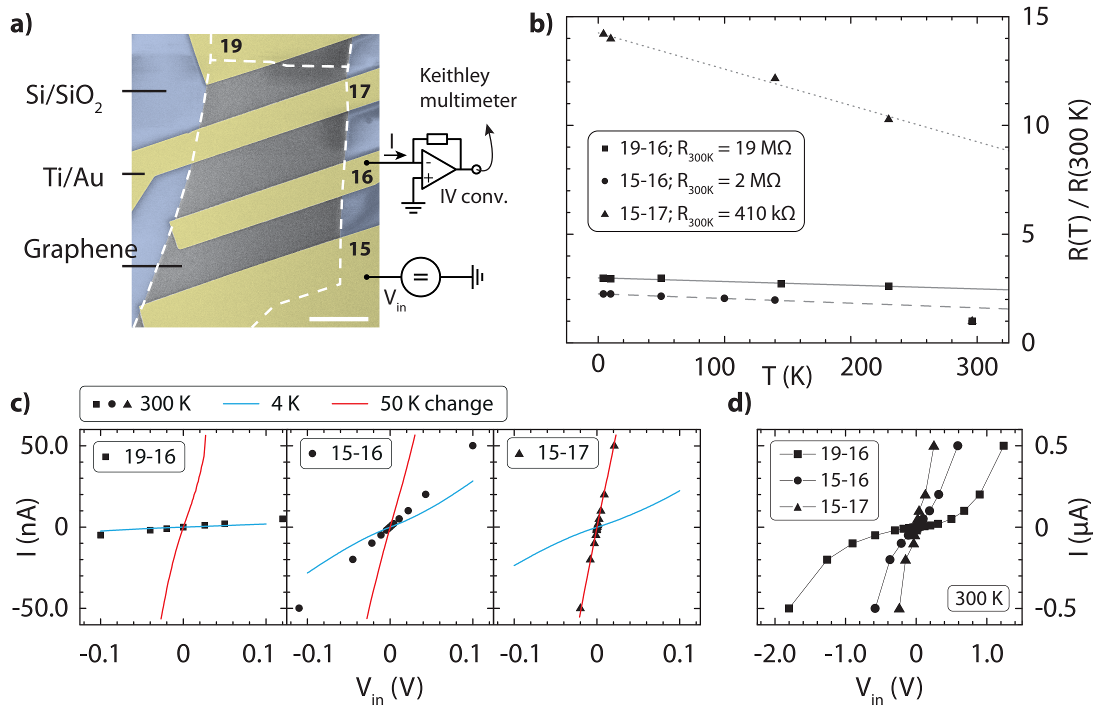

Figure 3.10: a) Coloured SEM micrograph of the measured device on sample ALD-6 with sketch of the DC voltage source and the IV converter used for the measurements. The broken line outlines the graphene flake. **b)** Resistances extracted from linear fits to the $I(V)$ curves at different temperatures, taken while cooling the sample. The resistances are normalised with their respective values at room temperature (given in the legend). The symbols represent the contact pairs and the lines are guides to the eye. **c)** $I(V)$ curves measured on three different contacts on the device for different temperatures. The data for 300 K and 4 K were measured while cooling, the "50 K change" data while warming up the sample. The latter show a spontaneous change in the behaviour of all contacts in the device, revealing a limited sample stability. **d)** Full data corresponding to the contact pairs in c) at room temperature. Taken from the blue curves in fig. 3.8.

increase for decreasing temperatures, the smoking-gun signature of tunnelling [85]. The resistance of junction 15-17 even increases by an order of magnitude. The room-temperature data for these three junctions, presented in fig. 3.8 above, are shown in fig. 3.10 d) for comparison.

In our measurements conducted while warming up the sample, we observed a sudden, unexpected change in the $I - V$ characteristics of all contacts. Fig. 3.10 c) shows the current for room temperature (black symbols) and 4 K (blue line), as well as the current after the change (red line) for all three contacts. The curves for 50 K show that the resistance decreased substantially and, in most cases, even dropped below the room-temperature resistance measured earlier (symbols in figs. 3.10 c) and d)). This can be explained by a barrier which broke through: Fig. 3.10 d) shows the full $I - V$ curves for the three junctions discussed here.

Junction 15-17 has a more or less linear $I - V$ curve at room temperature but shows a very flat trace around 4 K (right graph of fig. 3.10 c). Whilst cooling to 200 K, its resistance increased by a factor of 10, suggesting that room temperature is already sufficient to overcome the barrier. The spontaneous change decreases the resistance and its value jumps back to its original room-temperature value. It is possible that the different thermal expansion coefficients of graphene and gold applied strain to the oxide layer, causing the suspected barrier breakthrough.

It is briefly mentioned in section 3.3.3 (see p. 42) that we also fabricated a sample with an even thinner Al_2O_3 layer. On devices made from this sample, we measured resistances which are still between 1 and 100 MΩ. On some of those junctions, the 2-terminal resistances showed metallic behavior, i. e. a resistance decrease for decreasing temperature (data not presented here). This metallic behaviour is a pinhole signature, which is consistent with the increased roughness of the oxide layer combined with its low thickness (an estimated 7 Å).

3.3.8 Conclusion for the NO_2-seeded ALD layers

We conclude from the presented data that it is possible to achieve tunnelling through NO_2-functionalised Al_2O_3. We found 8 cycles to be the best compromise between thickness and tunnelling transport. The lowest resistances and resistance-area products we measured and extracted from the devices without pinholes are still spread across a range of 1 to 30 MΩ, i. e. over almost two orders of magnitude. These values are generally very high in comparison to values between 10 and 100 kΩ reported by other groups [11, 94] for Al_2O_3 barriers. On the other hand, we do observe tunnelling behaviour in our devices which suggests that a further reduction of the oxide thickness is necessary to meet our requirement that the contact resistances should remain below 1 MΩ.

The large spread of the RA values, however, is a clear sign for strong inhomogeneities in the barrier. When we further reduced the oxide thickness by omitting the high-temperature ALD step, we observed metallic behaviour in some junctions, whereas the resistances of the non-tunnelling junctions are still in the range of 1 to 100 MΩ. Possibly, Au or Ti/Au clusters form very small metallic contacts through pinholes.

We are convinced that the large RA spread and the sample stability issues are ultimately caused by the difficulties in growing thin conformal NO_2-seeded aluminium oxide layers on graphene with our recipe. Consequently, the ALD process in this form is not suited to fabricate sufficiently homogeneous ultrathin layers, and we decided to try a different functionalisation method.

3.4 Characterisation of the TiO_2-seeded ALD layers

We chose seeding the Al_2O_3 growth with a submonolayer of Ti which is oxidised after deposition (see recipe in section 3.1.3) as an alternative approach to improve the quality of our tunnel barriers.

3.4.1 AFM measurements

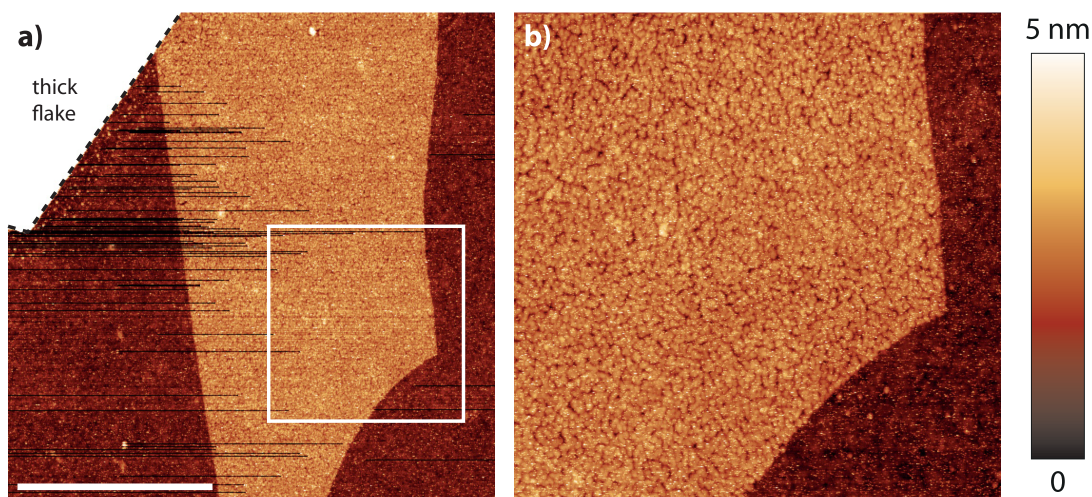

Figure 3.11: AFM images of a graphene flake after TiO_2 deposition at -35 °C and after ALD (5 cycles at 55 °C and 3 at 225 °C). The lines in a) come from material which was dragged over the surface by the AFM tip. The white area in the upper left is a thick piece of graphite. The scale bar corresponds to 2 μm. **b)** Close-up of the region in **a)** which is marked by the white rectangle (2 μm × 2 μm).

The graphene flakes were prepared as described in chapter 2.2 and used recipe 2 from section 3.1.4 for the fabrication of TiO_2-seeded alumina layers. Fig. 3.11 shows the topography of a graphene flake which was covered with this type of oxide. We obtain a roughness of 0.47 nm for the alumina layer and 0.40 nm for the substrate. This is in the range of the rms values for NO_2-seeded Al_2O_3 (see table 3.1 on p. 41).

The temperature of the sample during the deposition of Ti seems to have a strong effect on the surface roughness: Ti deposition at room remperature yielded a much worse coverage than at a sample temperature of -35 °C, possibly because the Ti clusters which land on graphene show increased diffusion at room temperature. For room temperature deposition, the roughness of the alumina-covered flake is 0.68 nm, the substrate roughness 0.24 nm.

3.4.2 Electric measurements

After growing the oxide, we deposited permalloy contacts (see chapter 1.1.4) by electron-beam evaporation from a permalloy target. In a second lithography step, the permalloy strips were contacted with palladium. To ensure contact between palladium and permalloy, 1 to 2 nm of the oxidised permalloy were sputtered away at the Py/Pd junction immediately before depositing Pd. Sputtering was performed in Ar atmosphere with a back-ground pressure of 10^{-5} mbar. Without breaking the vacuum, the samples were transferred into the evaporation chamber where palladium was deposited by thermal sublimation.

Before the transport measurements, we verified that there were no leaks from graphene to the back-gate. For a first characterisation of our samples, we performed two-terminal zero-bias measurements by applying an AC voltage and measuring the current, both with the same lock-in amplifier[3]. The resistances we obtained on this sample scaled much better with the contact area than in the case of NO_2 functionalisation. The resistances also increased during cool-down. Generally, the order of magnitude of the two-terminal resistances was between 10 to 100 kΩ, which corresponded well to resistances reported in the literature for comparable devices. These values were much lower and more homogeneously distributed than for NO_2 functionalisation, but still showed a certain spread.

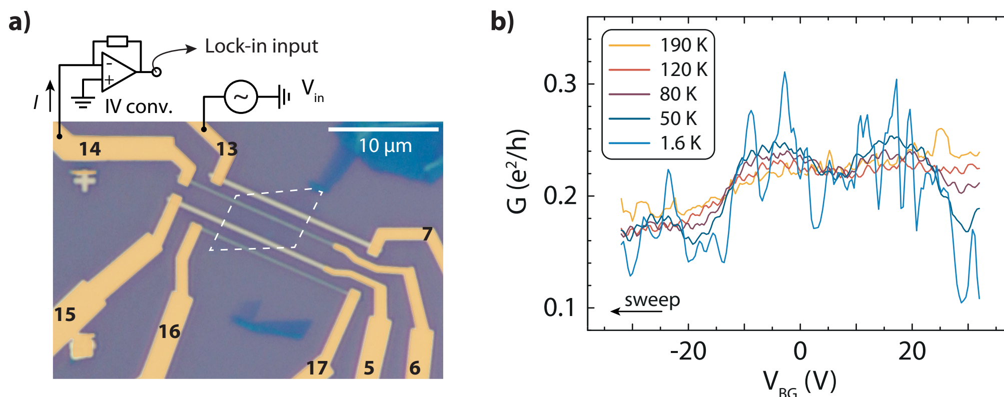

Figure 3.12: a) Optical micrograph of a graphene spin-valve device on sample "TiO2" with a sketch of current source and voltage probe used for the non-local measurements. The dashed line outlines the graphene flake. The four parallel contact strips consist of permalloy and are contacted with Pd which is coloured orange for clarity. **b)** Series of back-gate sweeps at different temperatures with a fixed AC bias voltage of 10 μV. The traces do not show a clear Dirac point but fluctuations which are reproducible when sweeping back and forth (not shown).

Two-terminal back-gate measurements on our devices, e. g. presented in fig. 3.12 a), usually showed conductance fluctuations which could be reproduced in several consecutive measurements and which were independent of the back-gate

[3]SR830 from STANFORD RESEARCH

sweep direction. Fig. 3.12 b) shows the temperature dependence of several back-gate measurements between two contacts. It is not possible to distinguish a clear Dirac point at high temperatures and it is most probably beyond the measured range.

The curves show oscillations which could be reproduced when sweeping the back-gate in both directions. Lowering the temperature increased their amplitude. From our available data, it is not possible to determine the origin of these fluctuations. Two candidates could be responsible:

- *Universal conductance fluctuations*, UCF, arise from a phase change of the electrons when they are scattered in graphene [103]. On a certain length scale, the *phase coherence length* L_φ, the electrons move along trajectories where their phases are correlated. Electrons travelling on different phases in a channel of length L interfere, which generates the UCF pattern with a maximum amplitude of $\sim e^2/h$. These interferences can be averaged out if $L_\varphi \ll L$. This type of fluctuation vanishes with increasing temperature and changes with an externally applied perpendicular B field.
- Alternatively, these oscillations could be Coulomb blockade-like features arising from charging of trap states in the oxide. Fig. 3.11 b) shows that the interface between permalloy and Al_2O_3 is not very homogeneous. Some regions in the barrier could be charged by the injected current, and a certain voltage, depending on the temperature, will be necessary to overcome this barrier.

Our available data do not allow us to draw definite conclusions. Since there was a TiO_2-Al_2O_3 top layer on graphene which was not perfectly homogeneous, as indicated by the AFM image in fig. 3.11, one can assume that the universal fluctuations were averaged out by the top layer and that the charging features played a greater role in theses measurements.

3.4.3 Spin-valve measurements

We performed magnetic-field-dependent measurements on devices with a non-local spin-valve layout (cf. section 1.2.6). The distance between the electrodes, i. e. the length of the spin channel, was 2 μm, its width close to 8 μm. Before measuring, we magnetised the electrodes[4] for a few seconds at a magnetic field of 700 mT. The back-gate was kept at zero. Fig. 3.13 shows two subsequent pairs of measurement traces (blue and orange, black and red) of the non-local resistance of a graphene spin-valve with TiO_2-functionalised tunnel barriers. The non-local resistance exhibits a jump ΔR_{nl} of about 8 Ω.

[4]Permalloy, contacted with palladium, as described in section 3.4.2

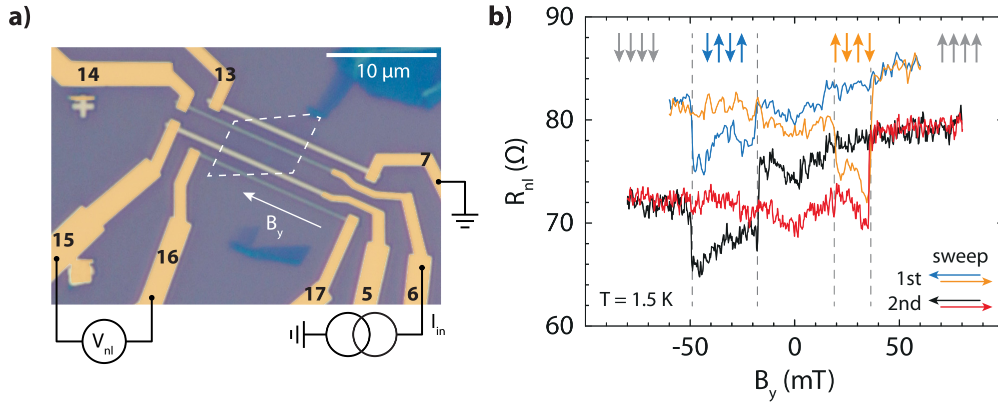

Figure 3.13: a) Picture from fig. 3.12 a), but with the measurement setup for the non-local geometry. **b)** Two consecutive sets of measurements of the non-local resistance R_{nl} of the device. The broken lines highlight the magnetic switchings and the arrows represent the magnetisation of the individual contacts.

Since two of the four ferromagnetic electrodes were designed with a width of 400 nm, the other two with 150 nm (see fig. 3.13 a), one would expect a jump in R_{nl} at ± 20 mT for the wider and at ± 60 mT for the narrower electrode (cf. section 1.1.4). Due to broken contacts, the coercive fields H_c of the electrodes could not be determined by AMR masurements. However, since almost all non-local resistance jumps in these four traces are reproducible (only one jump in the red trace is missing), it is still possible to assign the switching fields to the strip widths: The wider contacts correspond well to the expected H_c of 20 mT (see section 1.1.3), whereas the narrower electrodes have lower coercivities than expected from fig. 1.3. Most probably, a slight broadening of the contact due to the lithographic process is responsible for the decrease in H_c.

For values of B_y beyond ± 50 mT, the orange (red) R_{nl} trace coincides with the blue (black) trace, which is a sign that the contacts do not retain any residual magnetisation. However, there is a hysteresis between the black and the red curve near $B_y = 0$ which indicates an incomplete alignment of the domains in the electrodes. This is probably related to the fact that R_{nl} is lower on the left side than on the right. The same holds for the blue and orange trace where the hysteresis is much smaller. The jumps of the narrower contacts corresponding to higher switching fields are not symmetric around $B_y = 0$, but they occur at the same magnetic fields for all traces.

For comparison, we also fabricated a sample with transparent contacts to graphene, i. e. without a tunnel barrier. Panel a) of fig. 3.14 is an optical micrograph of the Py and Ti/Au electrodes on graphene. Similar to the device shown in fig. 3.13 a), the electrodes were designed to have widths of 400 nm and 130 nm and were contacted with 5 nm of Ti and 35 nm of Au after sputtering away oxidised permalloy. Back-gate measurements conducted on this device (panel

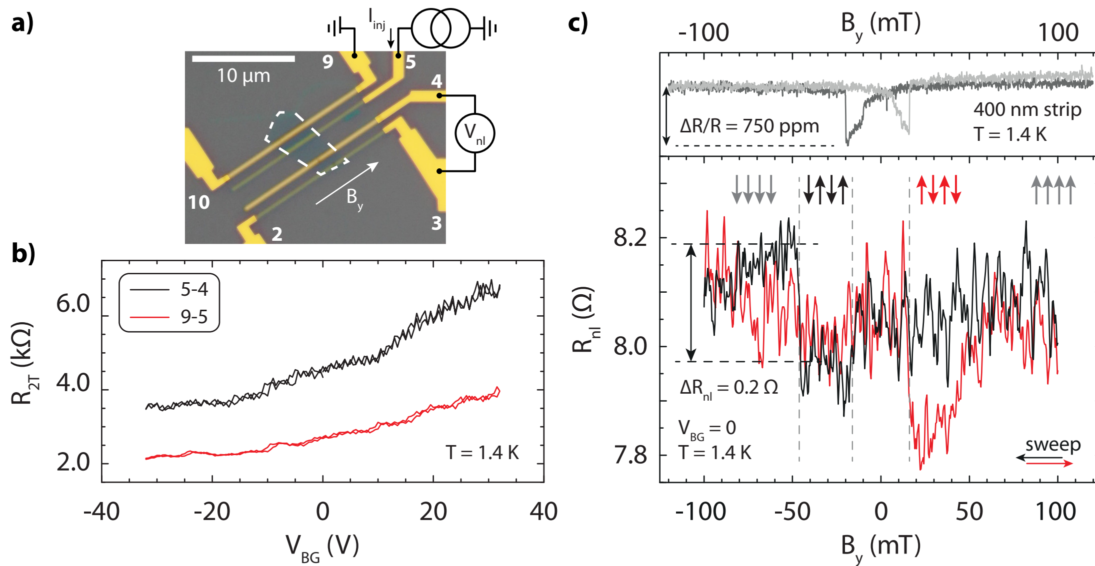

Figure 3.14: a) Device with transparent contacts made of permalloy (four parallel strips of pairwise different widths of 400 nm and 130 nm). The Ti/Au contacts are coloured yellow for clarity. The broken line highlights the graphene flake. **b)** Two-terminal back-gate measurements for the spin transport channel (5-4) and the injection path (5-9). The graph shows both sweep directions of V_{BG} for both contact pairs. **c)** non-local measurement on a device without a tunnel barrier with corresponding AMR measurements. The broken lines mark the magnetic switchings. The arrows represent the magnetisation of the individual contacts.

3.14 b) suggest that a Dirac point exists beyond 32 V, the maximum voltage we applied.

Fig. 3.14 c) shows two non-local measurement traces for such a device. AMR measurements of the wider contacts (400 nm) are plotted above the transport data. The switching fields correspond quite well to the 20 mT expected for this strip width (cf. fig. 1.3 on p. 7). The AMR data for the narrower strips (not shown) are very noisy, thus we could not distinguish a clear field. As explained in section 1.2.6, we expect this sample to show very weak magnetic signals due to the low expected contact resistances. Indeed, we obtain a low resistance jump of ΔR_{nl} = 200 mΩ which almost disappears in the noise. Similarly low switches have been reported for transparent Co contacts [48].

3.4.4 Comparison with data from other barriers

A comparison of the non-local signals obtained from our Al_2O_3 samples with values from MgO and MoS_2 samples provides insight into additional possible contributions to the measured non-local offset voltages. This is treated in detail in appendix D (pp. 121).

3.4.5 Conclusion for the TiO_2-seeded ALD layers

We conclude that TiO_2 seeding yields slightly smoother layers than NO_2 seeding, which is supported by the somewhat lower roughness for TiO_2-Al_2O_3. The AFM images show that the oxide is smoother and that the edges are better covered with TiO_2 seeding. This fabrication method also yielded more homogeneous RA_{eff} products than for NO_2 seeding, although they are still spread over an order of magnitude. We were successful in fabricating spin-valve devices with these barriers and observed clear switches in the non-local resistance caused by an external magnetic field. Yet, we see that these spin signals are still somewhat low when comparing to results reported for functionalised Al_2O_3 on graphene [94] or spin injection with MgO [75, 104]. This can in part be explained by the large spacing between our injector and detector electrodes I_+ and V_+ and the small distance between V_+ and V_-.

Our measured two-terminal resistances, however, are still spread over an order of magnitude which suggests that the barriers are inhomogeneous. In most cases, we observe that also the TiO_2-seeded samples are unstable, since their behaviour spontaneously changed during measurements. Just as in the case of NO_2 seeding (cf. fig. 3.10 c), some TiO_2-seeded samples showed a spontaneous drop in the measured resistance, indicating a breakthrough of one of the barriers. All of the samples showed low lifetimes and stability, preventing us from collecting further data.

3.5 Summary

This chapter describes pioneering work to fabricate tunnel barriers made from ALD-grown aluminium oxide in order to achieve spin injection into few- and single-layer graphene. This method had not been used for this purpose in the group before. We tried two recipes to functionalise graphene for a successful ALD process. Based on the fabricated samples, we judged the quality of the oxide layers and their suitability as tunnelling barriers.

NO_2 functionalisation resulted in a rather rough growth of the oxide layers on graphene. Their coverage is not homogeneous, which can be seen in particular at the flake edges (cf. fig. 3.5 a and d). Our Raman measurements did not show a significant increase in the defect-related peaks, such as D and D', and we conclude that our graphene flakes are not negatiely affected by NO_2. $I(V)$ measurements revealed large resistances which, even for our thinnest barriers, are spread between 1 and 100 MΩ. These high values are not well-suited for spin injection, although we observed tunnelling signatures (cf. fig. 3.10). Our attempts to achieve spin injection with Py electrodes on NO_2-functionalised graphene was not successful because of the low sample stability.

Changing the functionalisation step from NO_2 deposition to seeding with an oxidised Ti submonolayer slightly improved the morphology and roughness of these oxide layers. The resistances were lower in value and spread, and we could observe clear and reproducible signatures of spin injection in non-local spin valves with spin signals ΔR_{nl} close to 10 Ω for the first time in our group. However, the low stability of the samples did not allow further insights.

Altogether, our samples with ALD-grown Al_2O_3 layers were mostly unstable, showed inhomogeneous behaviour and had a low lifetime, rather independent of our chosen seeding method. Other fabrication methods or other tunnel barrier materials may yield better results: Dlubak *et al.* [105] presented sputter-deposition and subsequent oxidation of aluminium as fabrication method, which yielded much smoother oxide layers on graphene than evaporated oxidised aluminium used e. g. by Tombros *et al.* [11]. An alternative functionalisation method for ALD-Al_2O_3 was published by Yamaguchi *et al.* [94] who describe working spin-valve devices with Al_2O_3 barriers. They coated their graphene flakes with perylene-tetracarboxylic acid (PTCA) prior to alumina ALD and were able to achieve spin injection with permalloy electrodes, extracting a spin relaxation time of τ_s = 175 ps, a spin diffusion constant of D_s = 0.1 m^2/s, a spin relaxation length of $\lambda_G = 4.2\ \mu$m and a spin polarisation of $P = 0.06$.

This rather low spin polarisation, together with our findings – especially the low sample stability – ultimately convinced us that Al_2O_3 is not sufficient for our purposes. Since we plan to fabricate a Cooper pair splitter with ferromagnetic detector electrodes, the spin polarisation should be as high as possible to produce reliable detectors. Reports show that MgO can fulfill this requirement, and values for P up to 30 % have been reported so far [48]. Consequently, we decided to change our tunnel oxide to MgO, the subject of the next chapter.

Chapter 4

MgO tunnel barriers

In chapter 3, we showed that we managed to fabricate tunnel barriers from ALD-grown Al_2O_3, but they are subject to instabilities, promise only low spin polarisation, and their fabrication is poorly reproducible. Therefore, we decided to try magnesium oxide as new barrier material. MgO offers great potential for spintronics in general: crystalline MgO barriers and crystalline contacts in magnetic tunnel junctions are expected to yield TMR values above 1000 % [106] which would enable a good on/off ratio in future spintronic devices. While these predictions have yet to be met, room-temperature TMR values of 220 % for sputter-grown crystalline MgO barriers were reported by Parkin *et al.* [107], essentially tripling the previous state of the art. More recently, even higher values of almost 1200 % at 4.2 K could be achieved in CoFeB-MgO-CoFeB structures [108], which is very close to the theoretical predictions [106].

MgO yielded very promising results in combination with graphene as well: Several groups observed successful spin injection into graphene, using tunnel barriers consisting of either directly deposited MgO [75], or of TiO_2-seeded MgO [48] which is reported to yield very smooth layers [96]. With this type of barrier, Han *et al.* [48] deduced spin polarisations as high as 26 - 30%. We decided to choose the combination graphene-MgO as a new route because it promises the high reported spin injection efficiency we need for the spin detectors in a future graphene-based Cooper pair splitter.

Section 4.1 provides a brief overview over the fabrication technique of our MgO barriers. In analogy to the Al_2O_3 barriers, we used Raman spectroscopy to investigate the influence of MgO on graphene (sec. 4.2) and atomic force microscopy to characterise MgO itself (sec. 4.3). The results of our charge and spin transport measurements are presented in section 4.4.

4.1 Fabrication

We exfoliated and deposited graphene onto Si/SiO_2 as described in chapter 2. The deposited flakes were cut into ribbons of 3 μm width and at least 10 μm

length by reactive ion etching. After cleaning the graphene ribbons in acetone, we transferred the samples into a vacuum oven and annealed them at up to 350 °C to remove resist residues. In a later stage of the experiments, we used an Ar/H_2 atmosphere at up to 350 °C for annealing (cf. fabrication summary in section 2.2).

4.1.1 Deposition of the MgO layer

The MgO barrier was grown on the annealed sample. While sputtering is usually a good way to deposit compound materials, Dlubak *et al.* [100] report that sputterin MgO onto graphene can damage the latter by turning it into amorphous carbon. To avoid this problem, we decided to use electron-beam evaporation of MgO single crystals to fabricate the MgO layer. The deposition took place in a UHV chamber[1] (base pressure $< 10^{-9}$ mbar) to ensure the cleanest possible growth conditions. This also helps to minimise O_2 loss during evaporation, since we did not apply an O_2 background pressure.

Wang *et al.* [96] managed to fabricate smooth MgO barriers by depositing a submonolayer of Ti on graphene and oxidising it prior to MgO growth. Even with a Ti thickness of as low as 1.2 Å before oxidising, they obtained an MgO layer with atomically smooth roughness. We chose to pursue the same idea for our tunnel barriers. To reduce surface diffusion of Ti on graphene, we cooled the sample to about -25°C. Choosing very low deposition rates of about 0.06 Å/s for both Ti and MgO allows good control over their respective thicknesses. Thickness and rate were measured with a quartz microbalance which can be calibrated for both materials. To obtain the low rates, we averaged the thickness increase over at least one minute before exposing the sample to the evaporated material.

After Ti deposition, without breaking the vacuum, we moved the sample to the load lock of the evaporator and oxidised Ti in an O_2 atmosphere. After transferring the sample back into the evaporation position in the UHV chamber, we deposited about 8 Å of MgO from an MgO target in the same evaporator at room temperature. On all devices, the MgO layer covered the whole sample surface and was not structured to avoid contamination with resist residues.

A technical detail allowed us to measure the thickness of both TiO_2 and MgO separately with an AFM (see section 4.3.1 below): The sample holder in the evaporator's main chamber has to be rotated away from the evaporation position in order to transfer the sample. When the sample is mounted back into the chamber and readjusted for MgO evaporation, its position is not exactly the same as for Ti deposition. This can slightly change the angle under which MgO is deposited onto the sample next to the clamps holding the wafer piece. As a consequence,

[1] BesTeC GmbH

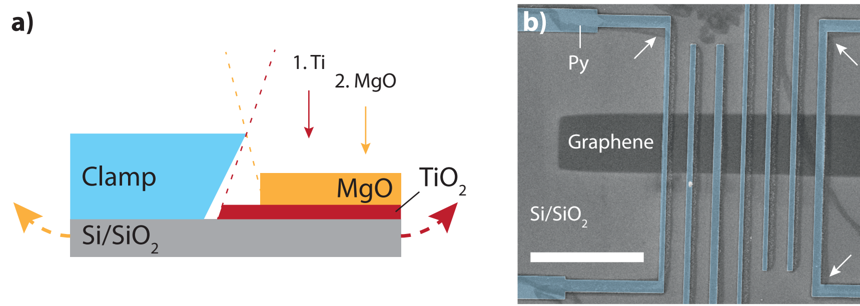

Figure 4.1: a) Small position changes of the sample holder (broken read and orange arrows) cause angle evaporation and lead to partly exposed TiO_2 layers. **b)** An MgO-graphene device with permalloy contacts. The parts of the Py electrodes which cross graphene have a well-defined width. The 90 ° kinks (for clarity, only some are highlighted with arrows) prevent magnetic domain movement from the large permalloy bonding pads to the electrodes. The ribbon-like shades on the substrate and next to the contacts come from lithography (see appendix A).

small sections of the TiO_2 layer may remain uncoated (cf. fig. 4.1 a) which allows to determine the thicknesses of both oxides (see section 4.3.1).

4.1.2 Lithography

In order to save time, we deposited the ferromagnetic electrodes, their leads and the bonding pads in the same lithography step (see section 2.3) onto our sample, i. e. they all consist of permalloy. The permalloy electrodes crossing graphene are designed such that they have different widths, between 300 nm and 120 nm, to ensure distinct magnetic switching fields (cf. fig. 1.3). To prevent the movement of magnetic domains from the pads into the strip, we introduced kinks of 90° in the parts of permalloy which were close to graphene (cf. fig. 4.1 b). The strips' switching fields can be determined with AMR measurements.

The contacts were written into a PMMA resist layer of 300 nm thickness using an electron microscope (cf. section 2.3) with an acceleration voltage of 30 kV. After the deposition of the electrodes, the devices were prepared for measuring as described in section 2.4 (p. 31).

4.2 Quality of graphene below MgO

We investigated the impact of an MgO top layer on graphene using Raman spectroscopy. Fig. 4.2 shows spectra of a graphene flake taken briefly after annealing

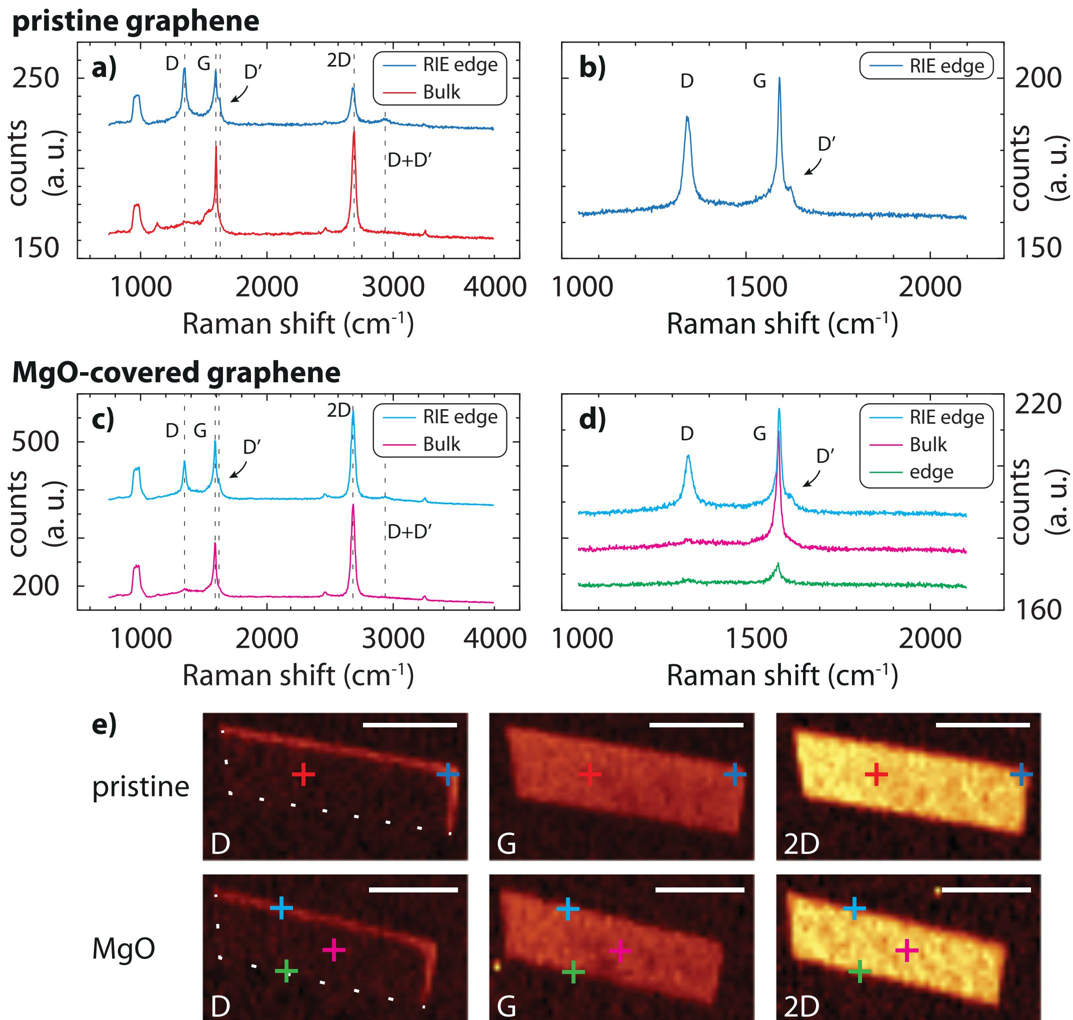

Figure 4.2: a) Raman spectra of pristine graphene taken on bulk and etched parts of graphene (see crosses in the "pristine" height maps in e). Both curves are normalised to the Si peak. **b)** High-resolution spectrum of the *D*, *G* and *D′* peak for the RIE-etched edge. Bulk data are not available. **c)** Raman spectrum of MgO-covered graphene taken on bulk and etched graphene (see crosses in the "MgO" row in e). **d)** Comparison of three high-resolution spectra around the *D* and *G* peak at three different locations (see e). **e)** Raman height maps of graphene's *D*, *G* and *2D* peaks. The intensities of the height maps in each row are normalised to the intensity of the respective *2D* peak. The flakes are outlined by the broken line in the *D* peak maps and the crosses show the locations where the spectra in a) – d) have been recorded. All scale bars corespond to 5 μm.

("pristine") and after MgO deposition, recorded at various locations on our samples which are indicated by the coloured crosses in fig. 4.2 e). On all our MgO samples where we performed Raman spectroscopy, we observed similar spectra.

The spectrum of the bulk of graphene does not exhibit a significant *D* peak (cf. fig. 4.2 a and c). At those edges where the graphene flake was etched, a large *D* peak can be seen in the spectra for both pristine and covered graphene (cf. spectra in fig. 4.2 a–d, and height maps in e). This peak originates from amorphous carbon at the damaged edges. To the right of the *G* peak, a small feature can be distinguished, the D' peak [69, 72], which is defect-related, just as the *D* peak. The sum D+D' is also highlighted in the spectra [69]. For comparison, the spectrum of a natural edge is plotted in 4.2 d) as well.

The extremely weak intensity of the *D* peak in the spectrum recorded in the bulk of MgO-covered graphene (fig. 4.2 b) shows that evaporated MgO is well-suited for the use with graphene. Additional unidentified peaks, as we could observe on our Al_2O_3 top layers (see fig. 3.7), did not appear in any spectrum of our diagnosed MgO samples.

4.3 AFM measurements on TiO_2-seeded and non-seeded MgO

As in the case of Al_2O_3 barriers, we used atomic force microscopy (AFM) to gather first informations about the oxide layers on graphene. The following section describes the calibration of the thickness monitor by comparing the intended barrier height (monitored with the evaporator's quartz microbalance) with barrier heights measured by AFM. Section 4.3.2 summarizes our findings of the investigation of the morphology of MgO on graphene, especially about the root-mean-square (rms) surface roughness R_q of the MgO layer on graphene and SiO_2.

4.3.1 Thickness of the oxide layers

Since we deposit and investigate very thin layers, we need to make sure that the thickness monitor is correctly calibrated. Small deviations can easily increase our barrier thickness which quickly leads to insulating barriers. As mentioned in section 3.3.2, it can be challenging to measure the thickness of an ultrathin layer. Using the sample holder in the UHV evaporator as shadow mask during the oxide deposition sometimes yields sharp steps in the oxide and can even separate TiO_2 from MgO (cf. figs. 4.1 a and 4.3). The thickness values obtained in this way are compiled in table 4.1.

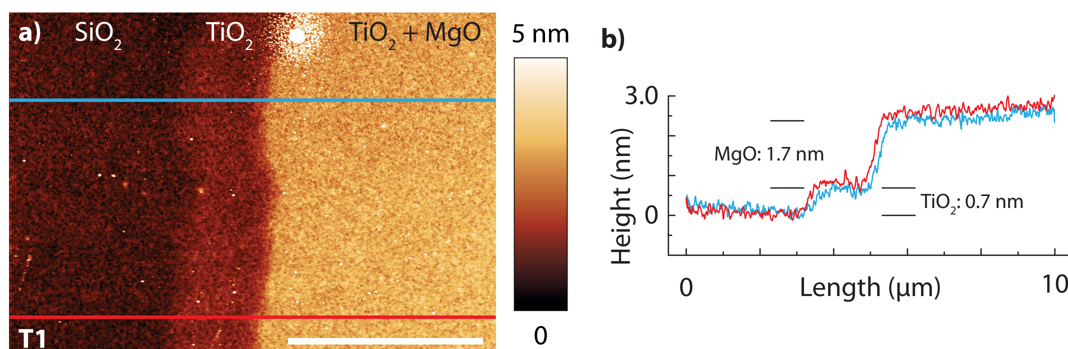

Figure 4.3: MgO and TiO_2 thickness in the beginning of the MgO study. **a)** Sample T1, coated with 1.2 Å of Ti (oxidised after deposition) and 1.6 nm MgO. Both values are taken from the quartz microbalance. The scale bar represents 4 μm. **b)** The profiles along the lines in a) show the height of the steps in the oxide.

On our first MgO samples, we observed that the AFM-measured thickness for MgO corresponded quite well to the thickness monitored with the microbalance: We obtained an AFM-measured thickness of 17 Å (16 Å according to the quartz crystal) on sample T1. The AFM profile curve in fig. 4.3 b) has a noise of about 2 Å which we can assume to be the error of the measured thickness. The monitored and measured thicknesses were about the same from which we concluded that the thickness monitor was well calibrated for the use of MgO.

Using the same error, the AFM measurements on TiO_2 yielded a thickness of (7 $\pm$ 2) Å which is about (5.8 $\pm$ 1.7) times the intended thickness of 1.2 Å of the Ti submonolayer. It is possible that a combination of the following considerations is responsible for the observed thickness increase:

- Material expansion: Ponomarenko *et al.* [109] report a thickness increase by a factor of 10 for oxidised Al in comparison to the originally deposited Al layer. For plasma-oxidised Ti thin films, Droulers *et al.* [110] have found a volume expansion of 1.1 to 1.4 when working with Ti films of > 15 nm. For equal expansion of height, width and length, the height of such a film would increase by about 10 %.

- It is possible that the thickness monitor did not yield precise values, especially for sub-nm thicknesses. The rate of 0.06 Å s^{-1} was averaged during slightly more than one minute, corresponding to a thickness increase of 4 to 5 Å, and averaging was always repeated at least once to ensure stable and reproducible growth conditions. Judging by the displayed thickness values, the error should not exceed 0.5 Å. However, the microbalance could still underestimate the total thickness of the Ti layer which was deposited to obtain the rate by 1 or 2 Å.

- The growth mode of Ti on SiO_2 could be responsible for the increased thickness: Judging by the colour scale in fig. 4.3, some areas appear to be quite

rough. We aimed at depositing a submonolayer, but Ti could have piled up and formed islands rather than a closed layer. When these islands are sufficiently high and close, the AFM tip cannot resolve the distance between them anymore and only the highest thicknesses will be measured.

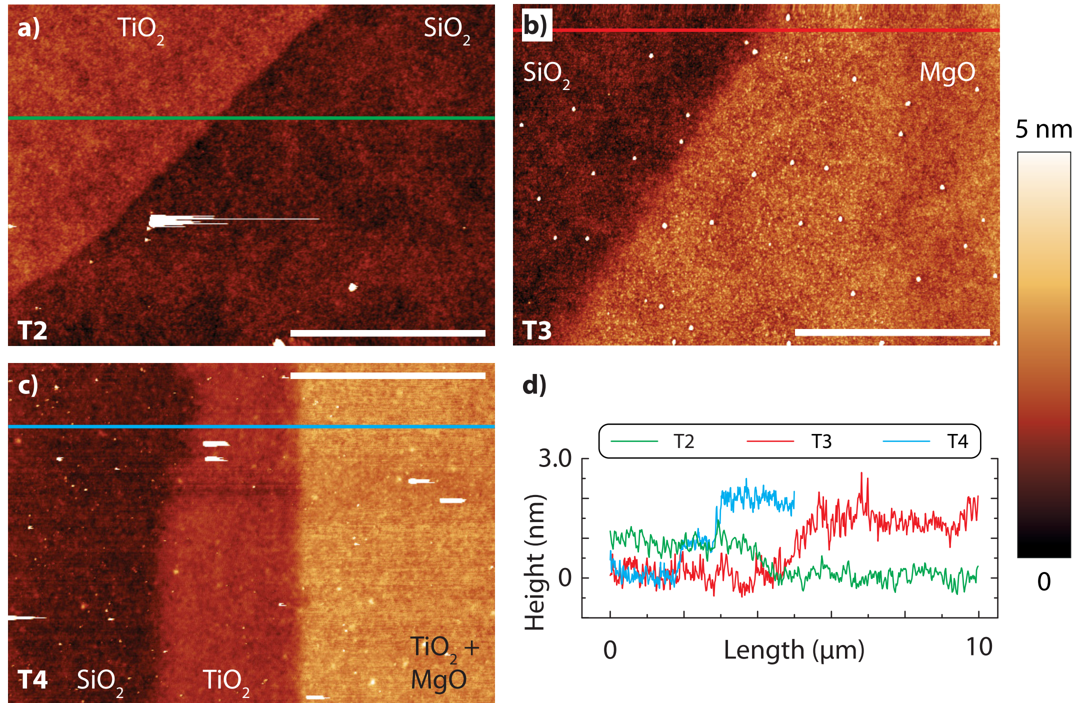

Figure 4.4: AFM-measurements conducted to determine the MgO and TiO_2 thicknesses later in the MgO study. **a)** T2: TiO_2 from 1.2 Å of Ti (monitored thickness). The scale bar shows 4 μm. **b)** T3: Unseeded MgO with a monitored height of 8 Å (scale bar 4 μm). **c)** Sample T4: 7 Å (according to the quartz) of MgO, seeded with oxidised Ti (1.2 Å by the quartz microbalance). The scale bar corresponds to 2 μm. **d)** Height profiles extracted from the AFM images (coloured lines) reveal an increase in bothTiO_2 and MgO heights in comparison to the beginning of the MgO study (cf. fig. 4.3). Note the different length scale in c).

In every batch, we attempted to prepare thickness test samples with steps as in fig. 4.3. On some of these test chips, we managed to obtain sufficiently sharp steps between all involved oxides, SiO_2-TiO_2 (T2), SiO_2-MgO (T3) and SiO_2-TiO_2-MgO (T4). These were fabricated a few months after the first thickness measurements and on the same wafer piece as our regular samples. Since we had already observed in our electric measurements that an increased amount of devices was insulating, the thickness of MgO was slightly reduced on T4 and we omitted the seeding step for T3 (see table 4.1). Figs. 4.4 a) – c) show AFM images from these samples. The profiles in fig. 4.4 d) were recorded along the coloured lines in a) – c).

Table 4.1 summarises the thickness and roughness values measured by AFM and also lists the quartz-monitored thickness for comparison. The MgO layers

Sample	Material	t_{quartz}	t_{AFM}	$t_{\mathrm{AFM}}/t_{\mathrm{quartz}}$	R_q
T1	TiO_2	1.2 Å	(7 ± 2) Å	5.8 ± 1.7	0.36 nm
	+ MgO	+ 16 Å	(17 ± 2) Å	1.1 ± 0.1	0.39 nm
T2	TiO_2	1.2 Å	(9 ± 4) Å	7.5 ± 3.3	0.27 nm
T3	MgO	8 Å	(13 ± 4) Å	1.6 ± 0.8	0.42 nm
T4	TiO_2	1.2 Å	(9 ± 4) Å	7.5 ± 3.3	0.19 nm
	+ MgO	+ 7 Å	(11.5 ± 4) Å	1.6 ± 0.9	0.25 nm

Table 4.1: Thickness t_{quartz}, t_{AFM} and roughness R_q of TiO_2 and MgO for figs. 4.3 (sample T1) and 4.4 (samples T2–T4). The errors were extracted from the noise of the AFM profiles in the corresponding figures.

on T3 and T4 (b and c) have different height, but their ratios of quartz- and AFM-measured thicknesses are consistent. The AFM-measured thicknesses deviate by slightly over 60 % from the quartz values which is much larger than in the beginning of the study. The AFM-determined thickness values of TiO_2 on samples T2 and T4 (fig. 4.4 a and c) were the same. Again, we could extract an error from the profile curves which is about 4 Å in this case. The AFM thickness values of T1, T2 and T4 were within this error margin, even within the 2 Å given above.

We believe that the MgO thickness changed over time (i. e., between T1 and T2–T4), even though this is partly masked by the larger error margins in table 4.1. This can possibly be explained by our observation that the composition of the crystals in the MgO target seems to change over time or with intensive use. Indeed, when refilling the MgO target, the old MgO crystals had not only changed into polycrystalline white powder, but some crystals had also accumulated some kind of dirt, visible as black spots on their surface. A possible reason is cross-contamination from a slightly defocused electron beam. The best results can be obtained with fresh MgO. Generally, it is advisable to occasionally recalibrate the quartz monitor by comparing the monitored thickness with AFM-measured values on suitable test samples.

4.3.2 TiO_2/MgO on graphene

By extracting the root-mean-square roughness values R_q, we can judge the homogeneity of the barrier and draw a comparison with the values we had obtained for Al_2O_3. These values can serve as benchmark for the smoothness of an MgO layer: the interatomic distance in MgO is 0.211 nm [96] and an R_q of the same magnitude would indicate a very flat and homogeneous oxide layer and act as lower boundary for the roughness. Several values of R_q extracted from

our AFM measurements are compiled in the tables 4.1 (TiO_2/MgO on SiO_2) and 4.2 (TiO_2/MgO on graphene, p. 66).

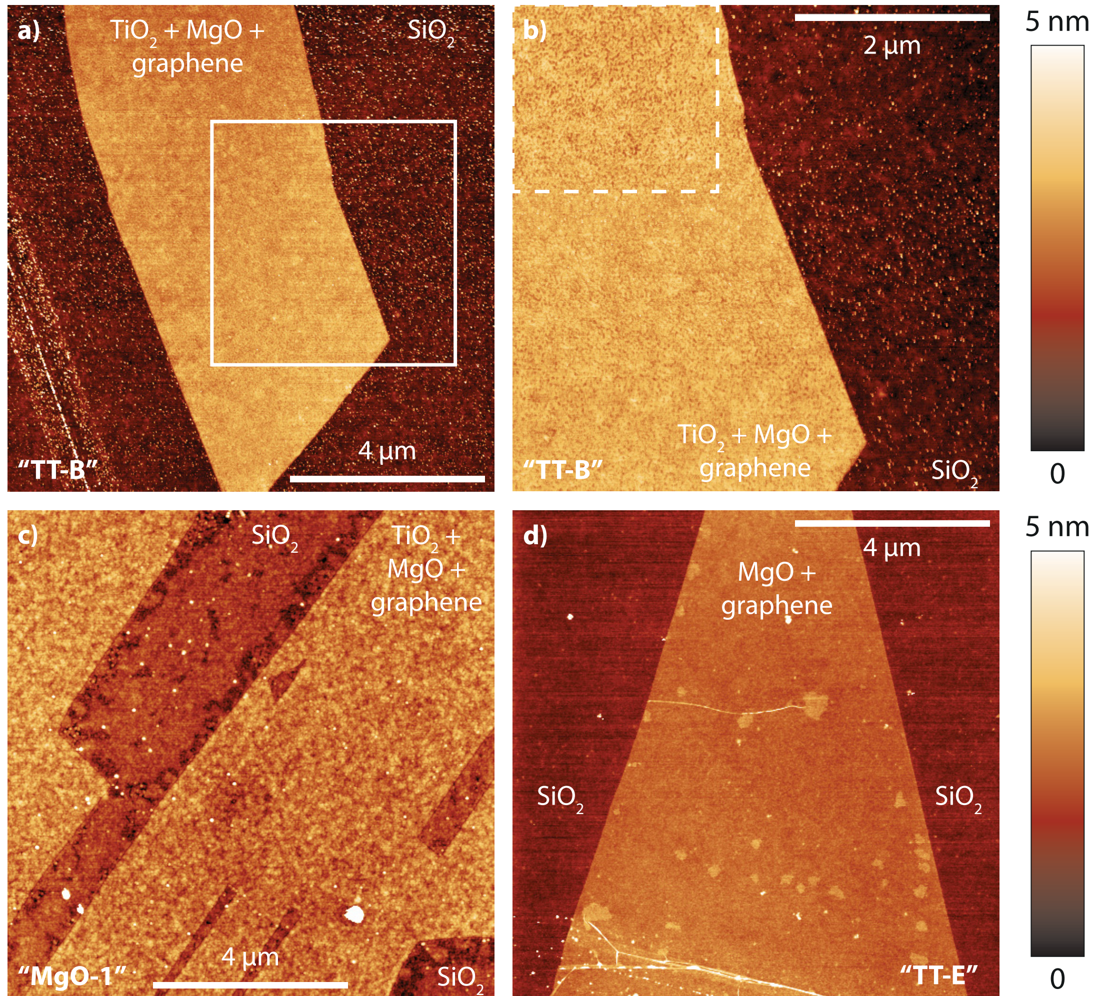

Figure 4.5: AFM images of graphene flakes with different seeding methods. **a)** 8 Å of MgO on graphene, seeded with 0.2 Å of Ti which was later oxidised. **b)** Close-up of the framed region an a). This region shows a higher roughness than the rest, possibly due to a cleaner AFM tip. **c)** 8 Å of MgO on graphene seeded with 2 Å of Ti (oxidised). **d)** 8 Å of unseeded MgO on slightly dirty graphene.

We experimented with various amounts of Ti and MgO. Fig. 4.5 a) shows a graphene flake after the deposition of 0.2 Å of Ti and, after oxidising Ti, 8 Å of MgO. The data highlighted by the white square were measured afterwards and are shown in b). The highlighted area in fig. 4.5 b) seems to have a slightly higher roughness of 0.34 nm instead of the 0.28 nm on the rest of the MgO-covered flake. This is most probably an artifact caused by a slightly dirty AFM tip, which made the oxide layer in some places appear smoother than it was.

Fig. 4.5 d) shows a thin graphene flake covered with unseeded MgO. A few patches of dirt can be seen on the surface, but the MgO layer is quite smooth and

Sample	Material	t_{quartz} (Å)	R_q: Graph.	R_q: SiO_2	fig.
"TT-B"	TiO_2 + MgO	0.2 + 8	0.30 nm	0.58 nm	4.5 a), b)
"TT-C"	TiO_2 + MgO	0.5 + 8	0.33 nm	0.99 nm	-
"MgO-1"	TiO_2 + MgO	2 + 8	0.34 nm	0.43 nm	4.5 c)
"TT-D"	MgO	8	0.43 nm	0.39 nm	-
clean "TT-D"	MgO	8	0.35 nm	-	-
"TT-E"	MgO	8	0.24 nm	0.29 nm	4.5 d)

Table 4.2: Roughness R_q extracted from AFM measurements on several graphene flakes covered with TiO_2-seeded and bare MgO (cf. fig. 4.5). The R_q for TT-D are quite high, because the sample had not been cleaned prior to MgO deposition and was dirty in some places. "Clean TT-D" denotes a cleaner region on TT-D, i. e. without obvious dirt.

we obtain an R_q of 0.24 nm. This value is even lower than for Ti-seeded MgO, although no special cleaning measures had been taken. Another sample with bare MgO, TT-D, had been covered with residues from a removed layer of resist. Naturally, its roughness is higher than that of the other flakes, but there is a large clean region with R_q as low as 0.35 nm. This is already very close to the value for atomically smooth barriers.

Several values for R_q from various MgO-covered graphene flakes with and without seeding are listed in table 4.2. We did not find a clear dependence of R_q on the TiO_2 content of the barrier comparable to the data in [96] but observed that the roughness values for MgO were below those of Al_2O_3, even if no special cleaning measures were taken. We conclude that MgO grows more conformally on graphene than Al_2O_3.

4.3.3 Conclusion

From height profiles recorded on suitably sharp steps from SiO_2 over TiO_2 to MgO with AFM, we found that the thickness of the MgO layer changes over time. While it deviated only marginally from its intended value in the beginning of the study, later measurements revealed an increase of abouth 50 % compared to the initial value. The thickness of the TiO_2 layer was almost by a factor of 6 higher than expected and it increased by about 30 % over time. Because of the strong dependence of the tunnelling current on the barrier thickness, this can easily insulate the injector contact from graphene. We observed this behaviour on several of our samples.

Comparing the root mean square roughness listed above with the values in table 3.1 and fig. 3.6 (pp. 41 and 42) reveals that the average roughness of MgO-

covered graphene was slightly lower than on our Al_2O_3-covered samples. The R_q on MgO can be fairly close to the reported roughness of 0.211 nm for atomically smooth MgO.

4.4 Transport measurements

This section describes the electrical characterisation of the tunnel barriers as well as magnetotransport measurements. We used the standard, zero-bias lock-in technique to investigate the tunnelling behaviour of the barriers. This method offers stronger noise suppression than DC measurements.

As already mentioned in section 4.3.1, barriers with an MgO layer thickness of 8 Å[2] which were seeded with a TiO_2 layer of 7 Å thickness as measured by AFM[3] – i. e. a total thickness of 15 Å – exhibited two-terminal resistances between 10^4 and 10^5 Ω and showed the best stability and yield. Later in the study, we also fabricated and measured unseeded, bare MgO barriers with a thickness of 13 Å[4] which showed lower resistances. Judging by these measurements, a good range for the total barrier thickness seems to be (15 ± 3) Å.

4.4.1 Electrical measurements

We measured most of our devices in a ^{4}He cryostat with variable temperature insert (VTI) and two superconducting magnets which enabled us to apply independent magnetic fields in two directions (B_y and B_z in our sample's frame of reference). The VTI can be cooled down to 1.6 K. We conducted two-terminal voltage bias measurements, using a Stanford Research SR830 lock-in amplifier as voltage source. The current through the device was amplified with an in-house-built IV converter and measured with the lock-in. We varied the backgate voltage with a Yokogawa YK7651 DC source.

On most of our MgO devices, we measure two-terminal resistances R_{2T} with an order of magnitude below those obtained on our Al_2O_3 devices (see section 3.3.6). This means that the resistance of graphene and the contacts could not be neglected anymore for the MgO devices, and that we were not able to estimate the resistance-area products $R_B A$ of our barriers as in section 3.3.6. Still, a certain trend can be read from comparing the R_{2T} and the involved junction areas, and we observed that higher contact areas almost always corresponded to lower resistances. This dependence and the measured values of R_{2T} which were

[2] quartz or AFM
[3] 1.2 Å according to the quartz microbalance, see table 4.1
[4] 8 Å according to the microbalance, see table 4.1

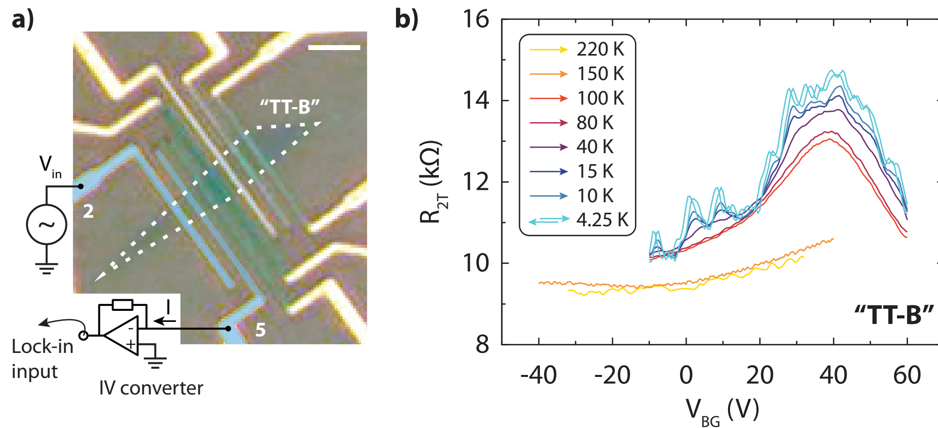

Figure 4.6: a) Optical micrograph of the graphene device on sample TT-B (see fig. 4.5 a) with sketch of the measurement setup for contacts 2 and 5 (highlighted in blue). The scale bar represents 5μm. **b)** Two-terminal resistances between contacts 2 and 5 with reproducible fluctuations. The arrows in the legend indicate the sweep direction of V_{BG}. To illustrate the reproducibility, both sweep directions for the 4.25 K trace are plotted.

mostly between 10^4 to 10^5 kΩ hint at tunnel barriers which may still contain pinholes. For transparent contacts, the two-terminal resistances would be much lower, so we can safely rule out this case.

One can make a few qualitative statements about the contribution of the tunnel barrier to the total resistance $R_{2\mathrm{T}}$ from its temperature dependence. We measured $R_{2\mathrm{T}}$ on the few-layer graphene flake shown in fig. 4.6 a). The traces of $R_{2\mathrm{T}}$ presented in b) were obtained on the junction 2-5 of the graphene flake. Most of them show a distinct Dirac point near 40 V which seems to move slightly to the left between 150 K and 100 K (orange and red curve).

The resistance curves show fluctuations similar to those we observed on our Al_2O_3 samples (cf. fig. 3.13 b) on p. 53. Here, they appeared below 40 K and were reproducible when sweeping the back-gate voltage in the opposite direction. At a base temperature of 4.25 K, the fluctuations in fig. 4.6 b) had an amplitude of about 0.2 e^2/h and, as in the case for Al_2O_3, could be charging of the barrier or universal conductance fluctuations. In the latter case, the phase coherence length L_φ of graphene would be of an order of magnitude of 1 μm, the distance between the contacts. This would require very clean or even suspended graphene.

Similar fluctuations with an even larger amplitude of e^2/h can be seen in the data presented in fig. 4.7 b). This sample was not cleaned prior to MgO deposition. The sample is quite dirty which would cause a short phase coherence length. This is a strong hint that e. g. charging of the MgO layer is a more probable cause for the fluctuations. A clear verdict is not possible from our data.

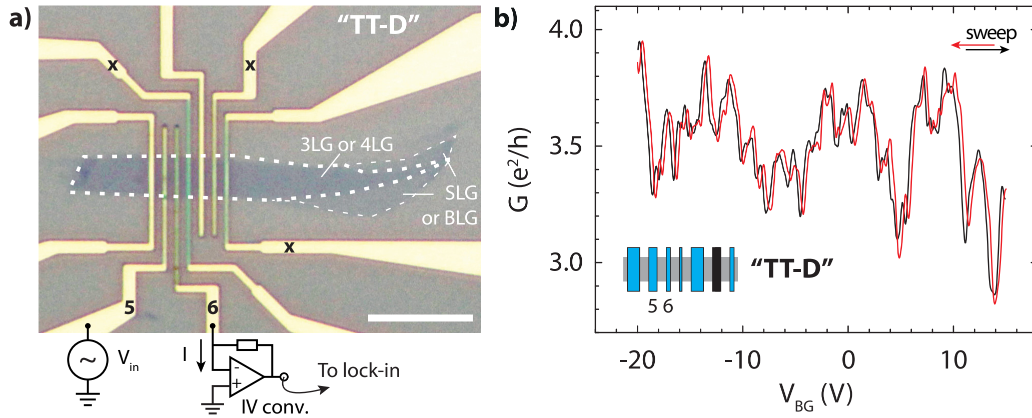

Figure 4.7: a) Device "'TT-D", later used for spin-valve measurements (section 4.4.2), fabricated with unseeded MgO. "x" denotes broken contacts. **b)** At a temperature of 5 K, the oscillations of the fluctuations in the two-terminal signals are as high as e^2/h.

4.4.2 Non-local spin-valve measurements

We were able to observe non-local spin signals in some of our samples. Fig. 4.7 a) shows an optical microscope image of a graphene spin-valve device on sample "TT-D" (cf. table 4.2 and fig. 4.8 a) below) where MgO was deposited onto multi-layer graphene without seeding. Bonding pads, leads and electrodes were fabricated from permalloy and written in the same lithography step to save time. The electrodes were designed with widths of 120 nm, 150 nm, 200 nm and 300 nm, but are expected to broaden a bit during lithography. While cooling the sample, some electrodes ceased to work and are labelled accordingly in the figure. The electric circuitry we used for the measurements is sketched in fig. 4.8 a) below.

We could determine non-local resistances on sample TT-D by applying a current and by measuring a non-local voltage. The voltage source of the SR830 lock-in amplifier in combination with a pre-resistor R_{pre} of usually 1 or 10 MΩ acted as current source with which we injected AC currents of about 300 nA. The non-local voltage signal was amplified with an instrumentation amplifier[5] and recorded with the SR830 (cf. fig. 4.8 a). On some measurements, frequency filters were used to reduce the offset signals.

Since most of the contact strips suitable for AMR measurements broke during cooling, we conducted a set of 15 consecutive measurements of R_{nl} in order to assign the coercive fields to the corresponding contacts in our magnetic measurements. The injector and detector circuits of this set are shown in 4.8 a). The data are presented in fig. 4.8 b) where the curves are offset from each other for clarity. Before every B_y sweep, all four ferromagnetic strips were magnetised at

[5] LI-75A by NF CORP., `http://www.nfcorp.co.jp/`

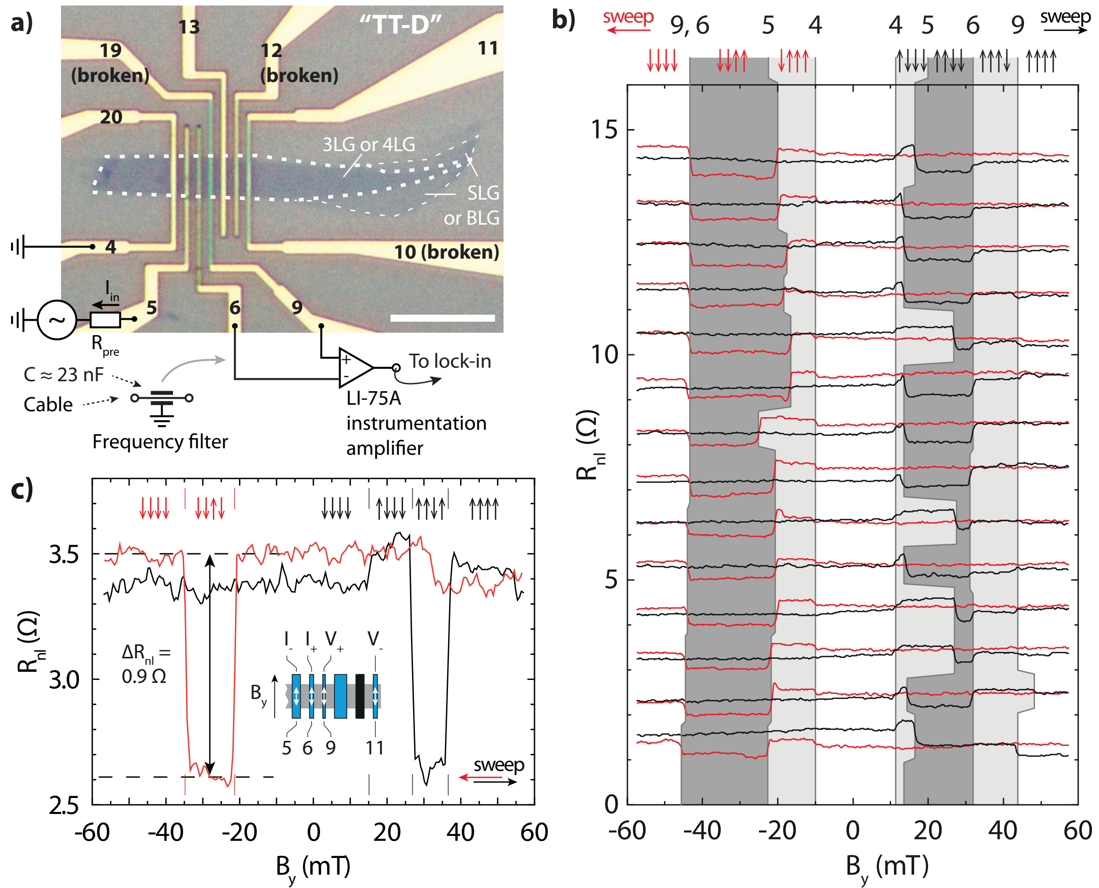

Figure 4.8: a) Optical micrograph of device "TT-D" consisting (cf. fig. 2.1) of a multi-layer graphene flake with an unseeded MgO barrier and permalloy contacts. Contacts 5 and 6 look damaged but were working fairly well (see also c). The sketched instruments represent the setup for the non-local measurements in b). Frequency filters were included in the lines in some measurements. The scale bar represents 10 μm. **b)** Set of 15 consecutive spin-valve curves measured with the contact configuration shown in a). The small black and red arrows symbolise the magnetisation of the electrodes. For both sweep directions, the leftmost arrow is contact 4, followed by 5, 6 and 9. **c)** Non-local resistance R_{nl} at 5 K as function of the magnetic field B_y. The contacts are shown in the inset. Note that the contacts are different from those in a) and b).

Fig.	Cont.	w (nm)	H_c^{exp} (mT)	$\underrightarrow{H_c}$ (mT)	$\underleftarrow{H_c}$ (mT)	Cont.
4.8 b)	4	300	24	12	-10	4
	5	200	39	15 … 27	-17 … -25	5
	6	150	60	32		6
	9	120	83	43	-45	9
4.8 c)	5	200	39	15	27	5
	6, 11	150	60	27		6, 11
	9	120	83	37	-35	9
4.9 a)	6	150	60	40	–	6
	9	120	83	48	–	9

Table 4.3: Coercive fields H_c of the contacts in figs. 4.8 b) and 4.9 a), b). w is the width of the contacts and H_c^{exp} the corresponding expected coercive fields (cf. fig. 1.3).

a field of -1 T (black curve) and 1 T (red curve). Note that the signals in b (and only there) are lowered due to a too low cut-off frequency on the amplifier. Still, we can draw some conclusions from the magnetic switching behaviour:

All data show clear and sharp jumps which are reproducible when repeated. It is easiest to identify the jumps which cause an antiparallel setting of polariser (contact 5) and analyser (contact 6). With values of $\Delta R_{\text{nl}} \approx 0.5\ \Omega$, these are the largest in the data, highlighted by the darker grey shading on the curves in fig. 4.8 b). In most cases, contact 5 reverses its magnetisation at an H_c of 14 mT, although the data also show occasional switches at 28 mT. This behaviour is more pronounced for positive B_y. For negative B_y, contact 5 jumps within a smaller range of H_c. In particular, for B_y near -10 mT, small switches can be seen in almost every red trace. These arise most probably from contact 4, although these coercive fields are clearly below those given in (fig. 1.3 b).

The data in fig. 4.8 c) were measured on a different junction after eliminating noise sources (e. g. ground loops) in the measurement setup. This also involved including the frequency filters sketched in fig. 4.8 a). As in the data for fig. 4.8 b), the strips were magnetised at -1 T (black curve) and 1 T (red curve). Two contacts, 6 and 11, had the same width and we expect to see only three jumps in the measurement traces. This is indeed the case for the black trace. The red curve is missing a jump around the expected fields, similar to some measurements in fig. 4.8 b). It is possible that three contacts switched at the same time, similar to the observations in b).

The switching fields H_c for the individual contacts turend out to be lower than the expected fields shown in fig. 1.3. This can be attributed to the broadening

of our contacts during lithography. The non-local signals R_{nl} of both curves are slightly offset from each other for $B_y < 15$ mT, possibly hinting at a residual magnetisation somewhere in the contacts. The data have an offset of about 3.1 Ω and show sharp jumps with ΔR_{nl} of about 1 Ω. Other spin-valve data we recorded show different offsets (cf. section 4.4.3).

4.4.3 Spin precession measurements

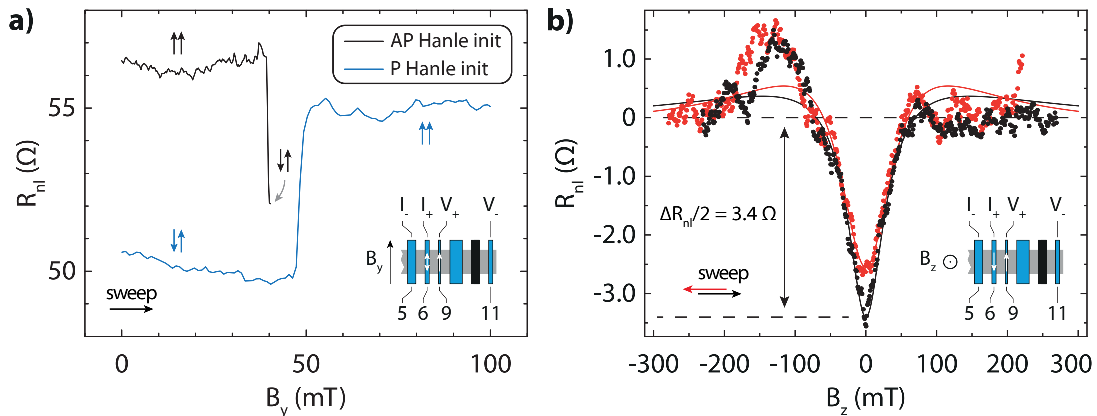

Figure 4.9: a) Initialisation of polariser and analyser contacts in antiparallel (AP; black trace) and parallel (P) configuration for spin precession measurements. The sketch in the inset shows the involved contacts. The blue trace was recorded shortly after the AP Hanle measurement, therefore I_+ and V_+ are still in AP alignment for $B_y = 0$. **b)** The points show Hanle spin precession curves for AP alignment of injector and detector at 5 K. The lines are fits to the Hanle curves, obtained with eqn. (1.18). The colours correspond to the sweep directions of the magnetic field B_z. As in a), the inset shows the contacts.

We conducted Hanle precession measurements to investigate the spin precession in our device. The inset of fig. 4.9 a) shows a sketch of the involved contacts: Like in the non-local spin-valve measurements (data in fig. 4.8 c), we applied a bias current of about 300 nA between contacts 6 (injector) and 5 (ground). The non-local voltage was measured between 9 and 11. First, the contacts I_+ (6) and V_+ (9) were magnetised in antiparallel orientation by sweeping the external field B_y to about 40 mT. The black trace in fig. 4.9 a) shows the non-local resistance which was recorded during this initial magnetisiation step. Immediately after the non-local resistance jump $\Delta R_{nl} = 4.5$ Ω appeared, we reduced B_y to zero and performed a B_z sweep. Fig. 4.9 b) shows two measured precession curves which correspond to two consecutive B_z sweeps in opposite direction. The blue curve in fig. 4.9 a) corresponds to the initialisation trace for the parallel (P) magnetisation of the electrodes. Because the parallel data are affected by strong noise and signal jumps caused by an external source, they are not shown.

The spin-valve signals in fig. 4.9 a) are discussed first: In comparison to the data in fig. 4.8 c), the offsets are almost 20 times as high (55 Ω here vs. 3 Ω above), the spin signals ΔR_{nl} about five times (4.5 Ω and 5 Ω here in comparison to 1 Ω in fig. 4.8 c), although the same contacts were used. This can be explained by the following observation:

The data in fig. 4.8 c) were recorded after the spin-valve data in 4.9. We observed that the two-terminal resistances $R_{4,5}$, $R_{5,6}$ and $R_{6,9}$ decreased over time by at least a third: $R_{5,6}$ and $R_{6,9}$ decreased from 15 and 19 Ω, measured briefly before the Hanle measurements, to about 10 Ω, measured briefly after the spin-valve measurements. Similarly, $R_{4,5}$ decreased from 4.5 Ω to 3 Ω. The bias currents we injected into graphene (up to 900 nA) seem to have caused a gradual degradation of the barriers, rendering them more transparent over time.

The two AP precession curves shown in fig. 4.9 b) were corrected by subtracting a linear offset. They display the expected dip arising from antiparallel alignment of the spins for $B_z = 0$. Yet, the traces are not symmetric around $B_z = 0$. The maximum near $B_z = -150$ mT appears for both sweep directions and is therefore not a part of the precession signal, but rather some background. Its origin and the nature of its B_z dependence are not clear from our data, but the permalloy bonding pads and leads on our device could contribute to the spin precession signal in an unpredictable way. One can observe that the minimum of the Hanle curve is a bit deeper than one would expect from the non-local jump. If the proper background were known, we would expect the data in the figures 4.9 a) and b) to be even more consistent. Note that we also recorded precession curves in P magnetisation, but the sample showed instabilities, and random jumps appeared in the signal. Hence, we could not suppress the background by combining the two curves.

Fig. 4.9 b) shows the AP Hanle data together with the fit according to eqn. (1.22). The value of ΔR_{nl} used in this formula was taken from the minima of the Hanle curve. We found that the best fit reproduced the dip but failed to fully capture the signal for larger field values. Fitting yielded the spin relaxation time τ_s and the spin diffusion length D. Since the spin transport was diffusive in our device, the spin relaxation length is $\lambda_G = \sqrt{D\tau_s}$. For the black Hanle curve, we obtained $D = (48.1 \pm 3.2)$ cm^2 s^{-1} and $\tau_s = (239 \pm 11)$ ps from which we calculated a spin relaxation length of $\lambda_G \approx (1.071 \pm 0.060)$ μm. The parameters for the red curve are $D = (22.8 \pm 1.7)$ cm^2 s^{-1} and $\tau_s = (134.9 \pm 0.035)$ ps which led to a spin diffusion length of $\lambda_G \approx (0.554 \pm 0.035)$ μm. The errors for D and τ_s were determined by the program MATHEMATICA[6] which was also used to fit the data. All these values are compiled in table 4.4 below.

Altogether, the values obtained for the red curve are quite different from those corresponding to the black curve. This is reflected in the fit curves, where the red

[6] Version 8, WOLFRAM INC.

one exhibits a stronger shoulder near -100 mT. Our values of D are about an order of magnitude lower than than those obtained by other groups [11, 48], which is most probably caused by insufficient cleaning of our graphene. The largest spin relaxation times reported in the literature are in the ns range [41, 74, 75]. Judging by the results presented in [48], our spin relaxation time is closer to the value they report for pinhole-dominated spin injection than for the tunnelling regime. As described in section 1.3.7, this could be an effect of contact-induced spin relaxation when the injector (I_+) and/or detector (V_+) electrodes are too strongly coupled to graphene, or if the coupling of reference (V_-) or ground (I_-) contacts to graphene is too weak.

After calculating λ_G from the fit parameters, it is possible to determine P_T, the polarisation of the injected spins at the interface. The device has a simple rectangular geometry, hence we may use $\sigma_G = L/(R_G W)$ and rewrite eqn. (1.15) in order to determine P_T:

$$P_T = \left(\frac{\Delta R_{\mathrm{nl}}}{R_G} \frac{L}{\lambda_g} e^{L/\lambda_g} \right)^{1/2} \tag{4.1}$$

This equation requires the knowledge of the ohmic resistance[7] of graphene, R_G, which we did not measure directly on this device. However, with the data from this particular device, we can give at least a crude estimate for R_G from the two-terminal resistances $R_{2\mathrm{T}}$: Along with ΔR_{nl}, we measured $R_{2\mathrm{T}}$ on a Py-graphene-Py junction between neighbouring strips (electrodes 6 and 5 for the data in fig. 4.9 a). The resulting value is the sum of the resistances of the two permalloy wires ($R_{\mathrm{Py},1} + R_{\mathrm{Py},2}$), of the MgO barriers at the junctions (R_B) and of graphene (R_G), i. e.

$$R_{2\mathrm{T}} = R_{\mathrm{Py},1} + R_B + R_G + R_{\mathrm{Py},2} \tag{4.2}$$

Most of our two-terminal resistances were above 10 kΩ, except for one pair (contacts 4-5 in fig. 4.9 a) where we found a considerably lower value of 4.5 kΩ. We assume this to be a pinhole-dominated or transparent junction with a low R_B and use this value of $R_{2\mathrm{T}}$ to estimate an upper boundary for R_G. Since all junctions have approximately the same geometry, this estimated R_G from junction 4-5 can be used to calculate a range for the degree of spin polarisation in the junction 5-9 within the range of the possible values of R_G.

Writing $R_G < R_{2\mathrm{T}} - R_{\mathrm{Py},1} - R_{\mathrm{Py},2}$ gives a maximum limit of graphene's resistance. The permalloy strip of contact 4 which was connected to bonding pads at both ends had an end-to-end resistance of $R_{\mathrm{strip}} = 1.4$ kΩ. Since contact strip 4 is the widest permalloy strip in the junction, this value serves as lower boundary for the total resistance of the permalloy leads on contacts 5 and 9, i. e. $R_{\mathrm{Py},1} + R_{\mathrm{Py},2} \gtrsim R_{\mathrm{strip}}$. Subtracting R_{strip} from $R_{2\mathrm{T}}$ gives an upper boundary for graphene's resistance of 3.1 kΩ.

[7] as opposed to the spin resistance R_G^s used in eqn. (1.12). Note that R_G is not the sheet but the bulk resistance.

	Black curve	Red curve
D $(\mathrm{cm^2\,s^{-1}})$	48.1 ± 3.2	22.8 ± 1.7
τ_s (ps)	239 ± 11	134.9 ± 7.5
λ_G (μm)	1.071 ± 0.060	0.554 ± 0.035
$R_G(\Omega)$	$500 \ldots 3100$	
P_T	$7.2\% \pm 18.0\%$	$13.6\% \pm 33.8\%$

Table 4.4: Fit parameters D and τ_s for the black and red Hanle curves in fig. 4.9 and the values for the spin polarisations P_T derived with eqn. (4.1) and the corresponding estimates for R_G.

Based on our observations and measurements on other devices, we choose a lower boundary of $R_G \geq 500\ \Omega$, yielding an interval of $500\ \Omega < R_G < 3.1\ \mathrm{k}\Omega$. The contacts 5 and 6 are at a distance of $L_{5-6} = 1\ \mu$m from each other which, for this particular geometry, yields a conductivity of $81\ \mu\mathrm{S} < \sigma_G < 500\ \mu\mathrm{S}$ or $2.1\,e^2/h < \sigma_G < 12.9\,e^2/h$. With this estimate for σ_G, the value $\Delta R_{\mathrm{nl}} = 6.8\ \Omega$ (cf. fig. 4.9 b) and graphene's channel length of $L_{5-9} = 1\ \mu$m for the Hanle measurements, eqn. (4.1) yields $7.2\ \% < P_{\mathrm{black}} < 18.0\ \%$ for the fit parameters of the black curve. For the red curve, we obtain $13.6\ \% < P_{\mathrm{red}} < 33.8\ \%$. The knowledge of R_G and R_B would reduce the large possible range of the results.

The discrepancy between the obtained fit parameters for the black and red data set is quite strong and certainly a consequence of the noisy data which also contain a few unexpected features, notably the maximum near -150 mT (cf. fig. 4.9 b) which is not related to spin precession. Both of this makes fitting very challenging and the only possibility to check the parameter consistency is to observe how well the fit corresponds to the minimum of the Hanle curve. Unfortunately, this is ambiguous: There is a large tolerance in respect to the parameters: τ_s and D obtained from fitting the black data also reproduce the red data set quite nicely. Other combinations of τ_s and D can also be found which yield P_T roughly between 5 % and 30 %.

Values for P_T obtained with eqn. (4.1) can be used as benchmark for the barrier quality. In the case of Co, Han *et al.* [48] give polarisations of about 1 % for transparent contacts, between 2 % and 15 % for pinhole-dominated barriers and polarisations about 30 % for tunnelling from Co into graphene. There are currently no values available for pinhole-dominated and transparent barriers in combination with permalloy contacts, but it is known that permalloy has a tunnelling spin polarisation between 45 % and 48 % [27, 28]. Our values for P_T are well below this, which would mean that the transport through the barriers on this device was pinhole-dominated.

4.4.4 Single magnetic switches

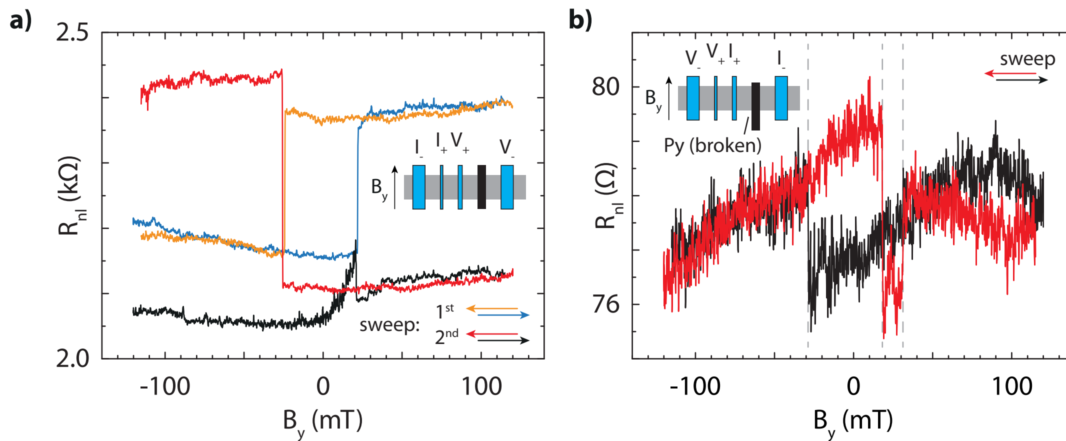

Figure 4.10: Single magnetic switches in the non-local MgO spin valves. **a)** Single jumps for a device with TiO_2-seeded MgO. The non-local signals are unusually high compared with our other devices. **b)** The same device with inverted contact configuration. The jumps are highlighted by the broken lines. The measurement frequency was much lower than in a), hence the increased noise. One of the jumps in the black traces is missing.

Some of our measured spin-valve signals exhibited only a single switch per B_y trace instead of the expected two or more: Fig. 4.10 shows two consecutive sweeps with a very large spin signal. All two-terminal resistances on this device had values between 10 and 100 kΩ. The blue and orange curve each show a single jump. It is probable that the magnetisation of one of the involved ferrocontacts had been pinned and remained in this state while B_y was varied. Between the first sweep (orange and blue curve) and the second one (black and red curve), B_y was increased to about 2 T which seems to have reversed the pinning, since the black and red curve now show opposite behaviour to the blue and orange curve. This behaviour could not be reversed in further measurements.

Exchanging current and voltage path yielded the curve in b). The noise is much higher, but two switches can be seen in the red trace. The strong discrepancy between the figures a) and b) might be explained by inhomogeneous barriers. There is also an additional, broken contact in the spin valve which could influence the measurements, e. g. by reflecting the diffusing spins back to the detector electrode V_+, thus increasing the measured non-local signal.

4.4.5 Comparison with data from other barriers

Further analysis, in particular of the measured offset voltages, can reveal more information about the data and the system. A comparison of the non-local values

from our MgO samples with those obtained from Al_2O_3 and MoS_2 samples are presented in appendix D (pp. 121).

4.4.6 Conclusion of the electrical measurements

We conducted electrical and magnetic transport measurements on both TiO_2-seeded and unseeded MgO samples. A common feature in both types of our samples was the existence of reproducible conductance fluctuations in back-gate traces. These fluctuations appeared at fairly low temperatures and were of an order of magnitude of $G \lesssim e^2/h$ (see figs. 4.6 b) and 4.7 b). They could also be observed in our Al_2O_3 samples (see fig. 3.13 b). Currently, we do not have enough data to determine their origin.

The magnetic measurements displayed clear jumps in the non-local resistance when sweeping B_y. We gathered enough data to assign jumps to the contact geometries (see also fig. 4.8 b)). Spin precession measurements for antiparallel magnetisation of our contacts showed a signal which corresponded approximately to the model (1.17) for small values of B_z. The curves had a distinct, reproducible background which was asymmetric in respect to the applied B_z field. Our fits to these data reproduced the minimum R_{nl} values near zero field well and yielded spin relaxation times of an order of magnitude of 100 ps and diffusion constants between 20 and 50 $cm^2\ s^{-1}$. These translate to spin diffusion lengths of $\sim 1\ \mu m$ which is in the range of the dimensions of our devices. However, due to the noisy data and the large background, the spin polarisation P_T had to be estimated with the formula (4.1). The resulting value is clearly below those P_T corresponding to true tunnelling transport, but can only be limited to a certain range due to numerical uncertainties.

4.5 Summary

We replaced Al_2O_3 by MgO as material for our tunnel barriers and successfully achieved spin injection into graphene for the first time in our group. We fabricated two variants of MgO barriers, with and without TiO_2 seeding. The AFM images in figs. 3.11 a) and b) show that MgO can form layers on graphene which are much smoother and less grainy than the Al_2O_3 layers we fabricated earlier. This is also reflected in the roughness values which we extracted from the AFM data (tables 4.2 and 4.1). The roughness of our oxides is already quite close to 0.21 nm, the inneratomic distance between the Mg and O atoms in an MgO crystal [96]. We deduce from our AFM and transport measurements that an oxide thickness of about 15 Å seems to be best suited for spin injection experiments.

Our Raman data show that the MgO deposition did not introduce notable defects to graphene (fig. 4.2). Hence, our evaporated MgO can in principle form a good interface with graphene without damaging it.

Electric measurements yielded a broad range of two-terminal resistances R_{2T} which covered a range from a few kΩ to being fully insulating. We found values of R_{2T} between 10 and 100 kΩ best suited for spin injection measurements, consistent with the literature (see e. g. Seneor *et al.* [10]). Lower R_{2T} hint at transparent barriers, higher R_{2T} are increasingly difficult to measure. Particularly, devices in which R_{2T} was larger than 100 kΩ showed more signs of electrostatic discharges, which usually destroyed contacts and nearby graphene.

We conducted magnetic spin-valve measurements with TiO_2-seeded and unseeded MgO layers and investigated lateral spin transport by reversing the contacts' magnetisation as well as by precession. Using the parameters extracted from the precession data and a conservative estimate for R_G, we obtained a spin polarisation between 5 % and 30 %, which is roughly comparable with reported results for pinhole-dominated barriers. The large range is due to the uncertainty of the fit which resulted from the considerable background on the Hanle data. In some measurements, we observed single jumps of the non-local resistance which were probably caused by the pinned magnetisation of an electrode.

Since we observed that the fabrication of our oxide layers was not well reproducible – a large number of devices turned out to be fully insulating without any changes made to the recipe – we decided to investigate the thickness of the deposited oxide layers more closely. We found out that the actual thickness of the deposited MgO had eventually become higher than the value given by the thickness monitor. We also found out that the quality of our MgO targets in the UHV evaporator degraded over time which could also have caused a change in the composition of our barrier.

The poor reproducibility of the fabrication and the unpredictable oxide thickness were quite large drawbacks of this method. As a consequence, we decided to pursue an entirely new approach by replacing the oxide with a layered material such as BN or MoS_2. These materials are ideally monocrystalline and have a well-defined thickness.

Chapter 5

Graphene spin valves with MoS_2 tunnel barriers

We learned from our previous experiments (chapters 3 and 4) that it is difficult to grow sufficiently conformal oxide tunnel barriers. There is, however, a promising alternative: Briefly after the first experiments on graphene, research turned towards similar layered layered materials which can be semiconducting or insulating. By exfoliation, these materials can be thinned down to yield two-dimensional crystalline pieces of largely homogeneous thickness which can be transferred onto graphene. They offer the possibility to easily tune the barrier thickness and thus its resistance by selecting a flake of suitable thickness for the transfer. Examples are hexagonal boron nitride (h-BN) or transition metal dichalcogenides [53, 111, 112], e. g. molybdenum disulfide (MoS_2), molybdenum diselenide ($MoSe_2$), tungsten disulfide (WS_2) etc. Most of these materials have already been known to exist in low-dimensional forms such as nanotubes [113–117]. for quite some time.

This chapter summarises our efforts to use exfoliated materials, in particular MoS_2, as tunnel barriers on graphene. Our choice of MoS_2 over h-BN is explained in section 5.1. Section 5.2 gives a brief overview over the basic properties of MoS_2. Section 5.3 describes fabrication and transfer of thin MoS_2 crystallites. 5.4 summarises our characterisation of MoS_2 by Raman spectroscopy, AFM and electric transport measurements. Electronic and magnetic transport measurements on graphene-MoS_2 sandwich structures are presented in section 5.5.

5.1 Boron nitride vs. MoS_2

Hexagonal boron nitride, h-BN, is an insulator with a band gap between 3.2 eV and 5.8 eV [118, 119], and it is isoelectronic with graphene. Having almost the same lattice constant as graphene makes it a very good match. Like graphene, h-BN is composed of several van-der-Waals-bound layers which can easily be separated e. g. by shearing. Because of this property, thick flakes of exfoliated

BN are primarily used as dry lubricant in industrial processes [120]. Recently, its feasibility as substrate, e. g. for graphene [68, 121], or as gate insulator [122] has been demonstrated as well. An h-BN substrate, or even encapsulation with h-BN [123, 124], strongly increases the mobility of devices based on exfoliated and CVD-grown graphene.

H-BN would also be a very good choice as tunnel barrier for spintronic applications. Spin injection into graphene through a BN barrier was reported very recently by Yamaguchi *et al.* [125], and tunnelling experiments were conducted as well [126]. However, the fabrication of such devices is very challenging: Tunnelling is only possible if the BN layer does not exceed a certain thickness, Britnell *et al.* [126] state that tunnelling through h-BN crystals which are thicker than 6 layers is suppressed. On the other hand, very thin exfoliated h-BN pieces are very difficult to detect by optical microscopy due to BN's large band gap which makes reproducible fabrication extremely complex. A novel approach could be the all-CVD fabrication of a spintronics device [127], but this is outside the scope of this thesis. We have therefore decided to use a different layered material which is easier to handle. This chapter focuses on molybdenum disulfide (MoS_2) which we used as tunnel barrier for spin injection experiments in graphene.

MoS_2 is easily visible with an optical microscope and it is much simpler to distinguish between areas of different thickness. Recently, it has received much attention [128] because several of its properties are relevant for technical applications, e. g. a large on-off ratio measured in FETs made from single-layer MoS_2 [128], room temperature mobilities of 700 cm^2 / (V s) [129], photoluminescence [130] or its tuneable bandgap (see below).

In technical applications, MoS_2 and other layered materials are mainly used as dry lubricants, a benefit which originates from their layered structures. Recently, MoS_2 has been demonstrated to be suited for mesoscopic applications as well, e. g. for integrated circuits [131] and as highly sensitive photodetector [132, 133]. Furthermore, it can easily be combined with graphene [132, 134, 135].

5.2 Material properties of MoS_2

5.2.1 Structural properties

Monolayer MoS_2 consists of Mo and S atoms arranged in a tri-layer (see fig. 5.1). In bulk MoS_2, also known as *molybdenite*, many of these layers are stacked on top of each other. Like in graphene, van-der-Waals forces hold the layers together which makes it easy to peel them apart with the same technique graphene is cleaved. Hence, exfoliation [53] and CVD fabrication [136] can yield very thin,

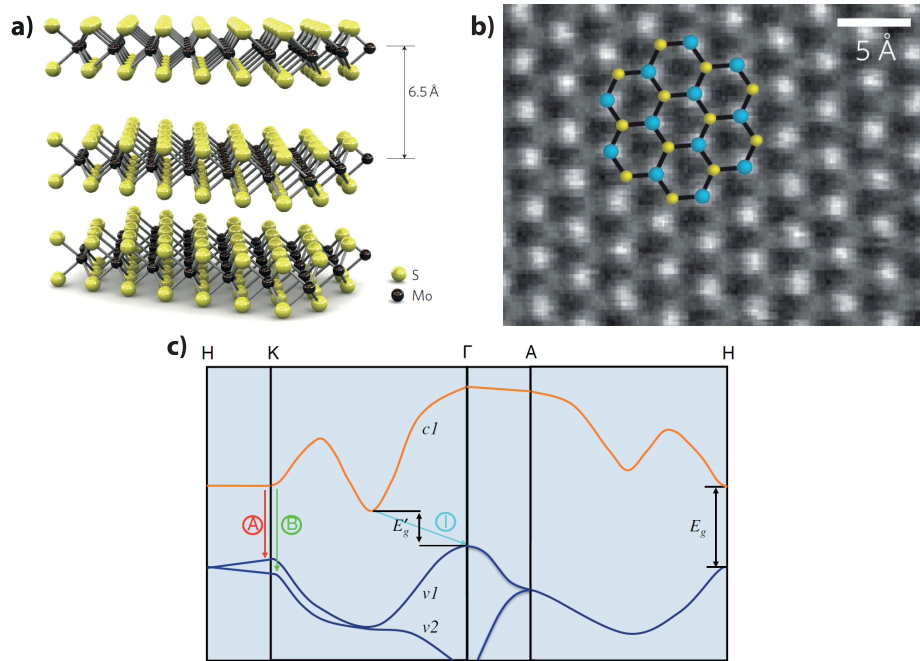

Figure 5.1: a) Sketch of the layered structure of crystalline MoS_2 with an interlayer distance of 6.5 Å. From [128]. **b)** TEM image of high-quality, CVD-grown MoS_2 with an overlaid sketch of the crystal structure (Mo: blue spheres). The hexagonal symmetry is clearly visible. From [136]. **c)** Calculated electronic structure of MoS_2. $c1$ is the lowest conduction band and $v1$ and $v2$ are split valence bands. For thick MoS_2, the energy gap is indirect and has a magnitude of E_g'. E_g at the H point is the direct gap which becomes relevant in monolayer MoS_2. From [137].

i. e. two-dimensional, crystals. The thickness of an MoS_2 monolayer were measured to be 6.75 Å by Benameur *et al.* [111].

5.2.2 Electronic properties

Unlinke graphene, MoS_2 is a semiconductor. It is a striking feature that monolayer MoS_2 is a direct semiconductor, whereas bilayer and thicker MoS_2 are indirect semiconductors [130]. Fig. 5.1 c) shows a part of the band structure of MoS_2. The band gap changes with the number of layers, from $E_g' \approx 1.29$ eV in bulk MoS_2 to $E_g \approx 1.8$ eV for suspended single-layer MoS_2 [137].

Single-layer MoS_2 was reported to undergo a metal-insulator transition at low temperatures for certain gate voltages [138] and a superconducting phase was found at very high charge carrier densities [139]. Since molybdenum has a high atomic weight, MoS_2 should show a larger spin-orbit coupling than graphene. While this may affect the spin transport in MoS_2 itself, there may be no influence on spins tunnelling through multilayer MoS_2.

The electron affinity of MoS_2 is about 4 eV [140]. According to the Schottky-Mott rule, Schottky barriers will be formed at the interface to a metal contact unless the work function of the contact is smaller than 4 eV or larger than 5.3 eV (or 5.9 eV for single-layer MoS_2). *Ab-initio* calculations conducted by Popov *et al.* [141] suggest that using Ti as contact material results in an ohmic contact at the MoS_2-Ti interface. Qiu *et al.* [142] reported a small Schottky barrier of 65 meV if Ti is used as contact material, and Das *et al.* [129] conducted an even more extensive study with four different contact materials. Taking into account Fermi level pinning at the MoS_2-metal interfaces, they obtain a Schottky barrier height of 150 meV for Ni.

In our experiments, we contacted multilayer MoS_2 flakes with permalloy strips. The work function of permalloy is reported to be 5 eV, similar to Ni [143], hence we do expect Schottky barriers at the MoS_2-permalloy interface. This should, in fact, support spin injection: If the energy of the electrons is kept sufficiently low, they cannot access the conduction band of MoS_2. If the MoS_2 layer is thin enough, we expect them rather to tunnel through the dichalcogenide into graphene. This might also prevent the spin-orbit coupling in $MoS_2$from acting on the electrons.

5.3 Fabrication

5.3.1 Exfoliation of MoS_2

We purchased MoS_2 crystals from SPI supplies[1] and exfoliated it with the same NITTO tape we also use for graphene (see chapter 2). The exfoliated MoS_2 crystals are pressed onto transfer wafers shown in the first picture of fig. 5.2.

The transfer wafers consist of our standard Si substrate with about 300 nm of SiO_2 and are spin-coated with a layer of a water-soluble PVA solution (2 %) as sacrificial layer. After baking for 3 minutes at 75 °C, the PVA layer is spin-coated with a thin PMMA membrane of about 150 nm thickness. The thickness values of these layers are chosen such MoS_2 is easily visible. After baking the PVA/PMMA stack again at 75 °C for 3 minutes, the exfoliated MoS_2 flakes can be deposited with the tape.

It should be noted that the yield of the exfoliation method is not easy to predict. While it was high in the beginning of this study, showing about one well-suited MoS_2 flake per transfer wafer, it eventually decreased. We tried to increase the yield by e. g. heating the Nitto tape. However, most of these methods damage the PMMA membrane carrying the MoS_2 flakes by causing it to ripple or to

[1] SPI SUPPLIES INC., `http://http://www.2spi.com/`

crack. This makes it hard or even impossible to achieve a clean transfer. Using a different kind of tape[2] deposited a greater amount of MoS_2 on the wafers, but destroyed the PMMA membrane and made a transfer impossible.

5.3.2 Transfer technique

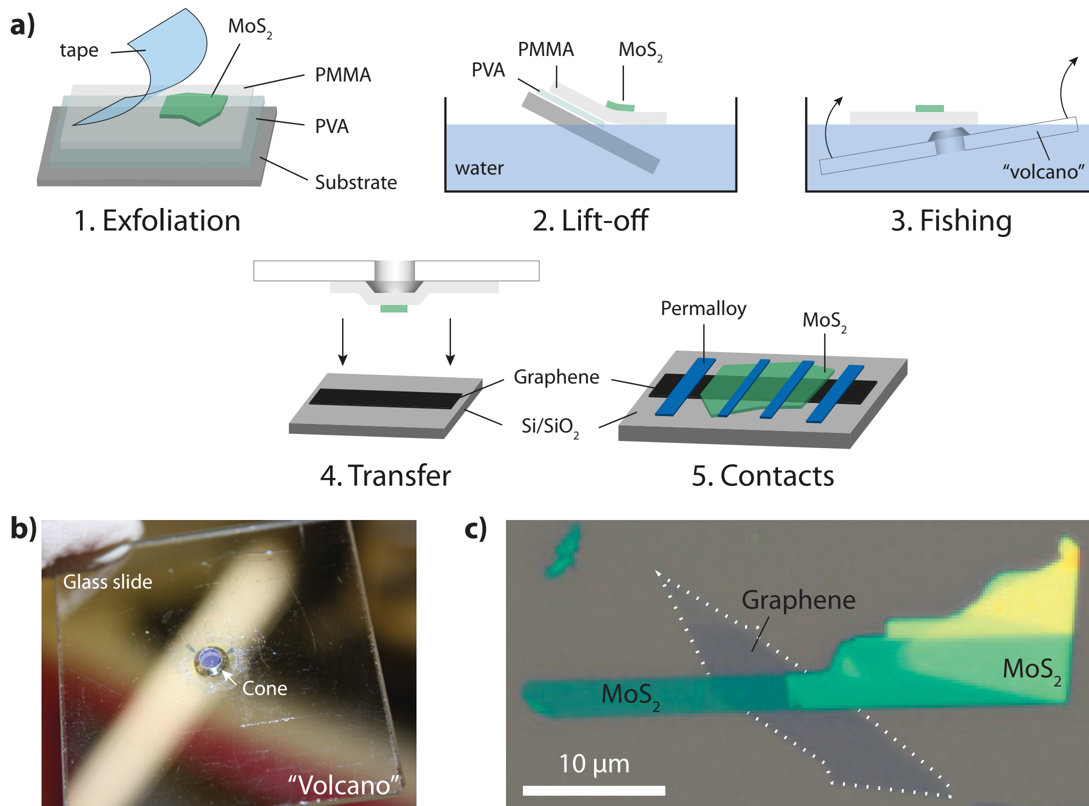

Figure 5.2: a) Technique for transferring MoS_2 crystals onto graphene. **b)** Photography of the "volcano": A cone-shaped metal ring is glued to the centre of the glass slide. Both the cone (or, "crater") and the glass slide have a hole which allows the water underneath the PMMA membrane to drain. The PMMA membrane (blueish reflection in the image) is stretched across the hole in the glass slide and the cone. **c)** Optical micrograph of the MoS_2-graphene stack of device "GMoS-03_C" after transferring the dichalcogenide.

To deposit MoS_2 onto graphene, we are using a dry-transfer technique adapted from the group of K. Ensslin (ETH Zürich). The process was optimised by A. van der Torren in our group and is illustrated in fig. 5.2 a). The exfoliated MoS_2 crystals are deposited onto a transfer wafer. The substrate is dipped into deionised water which dissolves the PVA sacrificial layer (picture 2 in fig. 5.2) and causes the PMMA membrane to float on the water. The membrane can be fished out

[2]Water-soluble wave solder tape by 3M Corporation

with a transfer tool ("volcano"), a glass slide and a crater-shaped metal ring, both with a hole for draining water. The metal ring keeps the area of the membrane holding the MoS_2 flake over the hole.

After drying, the glass slides with the MoS_2 flakes are mounted into a transfer microscope with the MoS_2 flake facing down (picture 4, microscope not shown). The wafer holding the graphene flake onto which the MoS_2 piece is going to be transferred is mounted onto a fine-tunable $X - Y$ table, taken from a disused mask-aligner, which allows precise control over the alignment of the two flakes. When a suitable position is found for the two flakes, the glass slide holding MoS_2 is gently lowered onto the graphene wafer until volcano and wafer are in contact. The alignment can (and mostly needs to be) corrected during the approach. Initially, the graphene wafer is heated to 120 °C, thus causing the PMMA membrane to relax before touch-down. After touch-down, the sandwich of volcano and graphene wafer is heated to 150 °C for about 5 minutes. Heat and pressure cut the PMMA membrane along the rim of the heated metal ring. After heating, the volcano is lifted off and the wafer holding the graphene-MoS_2 stack (picture 5 in fig. 5.2) is further annealed at 120 °C in air. The remains of the membrane are dissolved in acetone. To further clean the surface, the samples with graphene and MoS_2 are further annealed in 20 sccm H_2 at about 300 °C (cf. section 2.2).

Whenever the PMMA membrane holding the MoS_2 flakes is strained, e. g. by improperly handling the volcano, folds and ripples are introduced in both PMMA and the MoS_2 flake. As a consequence, the transfer becomes less precise and the MoS_2 flake will not lie flat on graphene. We found that it is best to place the membrane in such a way on the crater that the MoS_2 piece is close to its edge. In this position, the membrane is better supported and not sagging as much as in the centre, allowing better targeting during alignment.

5.3.3 Lithography

On all samples, permalloy was used as material for the ferromagnetic contacts. A substantial improvement over the PMMA-based lithography could be achieved by using a different resist, ZEP502A[3], which was introduced during the course of this study. The dirt which can be seen next to our contacts in some SEM images (see e. g. fig. 5.7 below or fig. 2.1 on p. 30) is most probably caused by PMMA/permalloy residues resulting from too little undercut in the resist. ZEP is a highly sensitive resist which yields a good undercut. The recipe was developed by Jörg Gramich and Julia Samm in our group. Replacing PMMA with ZEP yielded much cleaner results.

[3]Fabricated by ZEON CORPORATION, `http://www.zeonchemicals.com`

Later in the study, we chose to deposit permalloy onto the graphene-MoS_2 devices in the last fabrication step to prevent the permalloy electrodes from oxidising prematurely which is not only caused by the prolongued exposure to air, but also when baking additional resist layers on the sample. This required three electron-beam lithography steps:

1. Write and deposit thin ($\leq$ 10 nm) strips of a non-magnetic metal which connect both the ferromagnet and the actual leads. We chose palladium, since it grows very conformally, also along MoS_2 edges, and is also still continuous at such a low thickness. The low thickness prevents breaking of the ferromagnetic contacts at the step which is formed at the Pd edges.
2. Write and deposit the leads and bonding pads onto the thin Pd patches. Any metal suitable for wirebonding can be chosen here.
3. Write and deposit the permalloy electrodes onto the other side of the thin Pd patches.

Note that some devices presented in this chapter (e. g. in sections 5.4.4 and 5.5.2) were fabricated using a two-step lithography process and with PMMA resist, some devices with ZEP. A brief comment about the fabrication is given for every device described in this chapter.

5.3.4 Thermal expansion of the graphene-MoS_2 stacks

Fig. 5.3 illustrates an issue which we often encountered on the graphene-MoS_2 heterostructures: In all images in the figure, cracks can be seen, e. g. in the permalloy electrodes (panels a and c) or in MoS_2 next to the permalloy electrodes (panels b and c). The width of these cracks is of an order of magnitude which ranges between 10 and 100 nm. The cracks are most probably caused by shearing forces arising from the different thermal expansion of the three materials MoS_2, permalloy and graphene, either during fabrication when the substrate is cooled for the deposition of permalloy, or while cooling the devices to low temperatures for the measurements. Steps, e. g. when a permalloy electrode is deposited onto palladium (three-stage lithography process), or folds in graphene (fig. 5.3 c-II) can also break the electrode.

MoS_2's linear coefficient of the thermal expansion between 300 K and 10 K is $\alpha_a = 0.49 \cdot 10^{-5}\ K^{-1}$ (lateral expansion) and $\alpha_c = 1.86 \cdot 10^{-5}\ K^{-1}$ (vertical expansion) [144]. Experimental values of the linear thermal expansion of permalloy are only available for high temperature ranges [145–147]. Low-temperature values for α_{Py} are only given numerically in [148]. For this temperature range, we can extract a value of $\alpha_{Py} \approx 1.0 \cdot 10^{-5}\ K^{-1}$ for the alloy $Ni_{77.6}Fe_{22.4}$ which comes closest in composition to our permalloy.

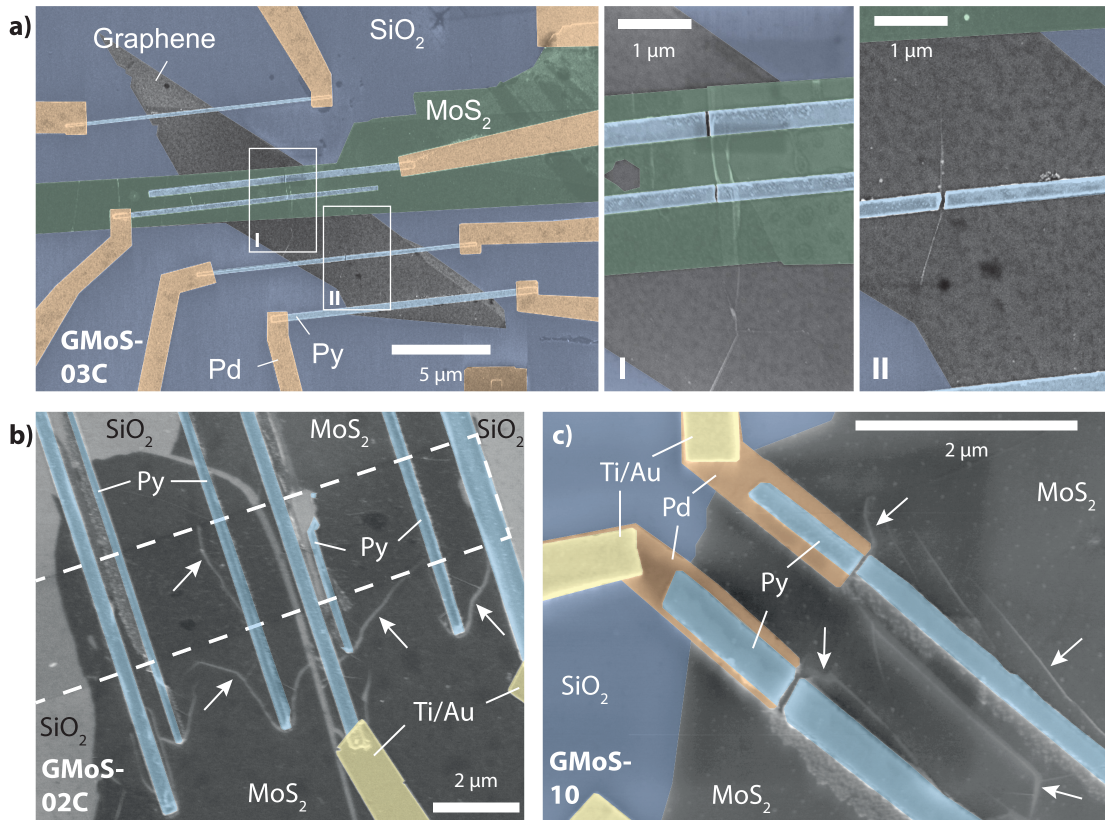

Figure 5.3: a) Left panel: Coloured SEM image of a graphene-MoS_2 heterostructure (device "GMoS-03_C, see also fig. 5.2) with permalloy/Pd contacts, prepared in a two-step lithography process using ZEP520A. The middle and right panel (I and II) are magnifications of the outlined regions and show broken permalloy contacts at folds in MoS_2 and graphene. **b)** MoS_2 flake (dark) on graphene (outlined). The permalloy electrodes (blue) were contacted with Ti/Au (yellow). The arrows mark some of the strain-related cracks. **c)** Permalloy contacts on MoS_2 with strain-related cracks (arrows). Here, MoS_2 was not coloured to improve the contrast. This device was fabricated using the three-step lithography process described in section 5.3.3.

The largest temperature difference in our devices occurs while cooling the temperature from room temperature to about 2 K. In this range, permalloy contracts twice as much as MoS_2. This can also be approximately quantified for our system: The permalloy strips have a length of about 20 μm at room temperature. Using the value of α_{Py} given above, the ferromagnetic strips will shrink by about 60 nm when cooling to 2 K. Hence, MoS_2 will shrink by about half this value, i. e. by 30 nm. This should leave gaps of 30 nm width in the MoS_2 layer. Indeed, we observed such gaps with widths between 10 and 100 nm. We found that the cracks appear less often if we deposit permalloy onto a substrate which is not cooled during evaporation. Especially the interruptions of the permalloy strips on the edges of the Pd patches (see fig. 5.3 c) can be avoided in this way.

5.4 Characterisation of MoS_2

5.4.1 Raman spectroscopy on a graphene-MoS_2 heterostructure

We conducted Raman spectroscopy on a sample prepared by transferring MoS_2 onto few-layer graphene with the method described in section 5.3.2. After removing the transfer resist, we recorded Raman spectra (see fig. 5.4 a–d) of bare MoS_2 (blue crosses in fig. 5.4 e), MoS_2 on graphene (red crosses) and uncovered graphene (black or white crosses in the figure) using an excitation laser with a wavelength of 532 nm.

MoS_2 lying on graphene and bare MoS_2 yielded similar spectra (cf. fig. 5.4 a), notably features characteristic for MoS_2, the in-plane Raman mode (E^1_{2g}) and the out-of-plane mode (A_{1g}): Both peaks are at their expected Raman shifts of 408.7 cm^{-1} for the out-of-plane Raman mode (A_{1g}) and at 383.7 cm^{-1} for the in-plane mode (E^1_{2g}) [149–151]). In addition, a large background signal with a maximum near 3000 cm^{-1} can be distinguished, which originates from MoS_2, because it is not present in bare graphene.

The spectra of bare graphene show the well-known characteristic *G* and *2D* peaks (cf. fig. 5.4 c) and d). Since we have used few-layer graphene of presumably three layers, the *2D* peak is broadened. The *G* peak has a small shoulder on the left side the origin of which is unclear. Splitting of the *G* peak has been observed on strained graphene sheets [152]. In our case, this strain could come from deposition on SiO_2. The *2D* signal of MoS_2-covered graphene is slightly blue-shifted in comparison to bare graphene. This effect, however, is similarly small as the shift in fig. 4.2.

A *D* or any other defect-related peak, arising from disordered graphene, is not visible in the spectra. This is the case for all our samples, hence we conclude that the transfer method does not damage graphene and yields samples of suitable quality for further experiments.

5.4.2 AFM characterisation of bare MoS_2

Freshly exfoliated MoS_2 flakes exhibited a very clean surface in our experiments, very much like graphene. Such a surface of an MoS_2 flake, which is sitting on the PVA/PMMA transfer stack, can be seen in fig. 5.5. Roughness data extracted from AFM measurements reveal that the surface of MoS_2 is very smooth in comparison to the values we had obtained previously on Al_2O_3 and MgO.

The values in table 5.1 show that thinner MoS_2 is slightly rougher. This is probably caused by the substrate: Thinner flakes are less stiff and thus more subject to

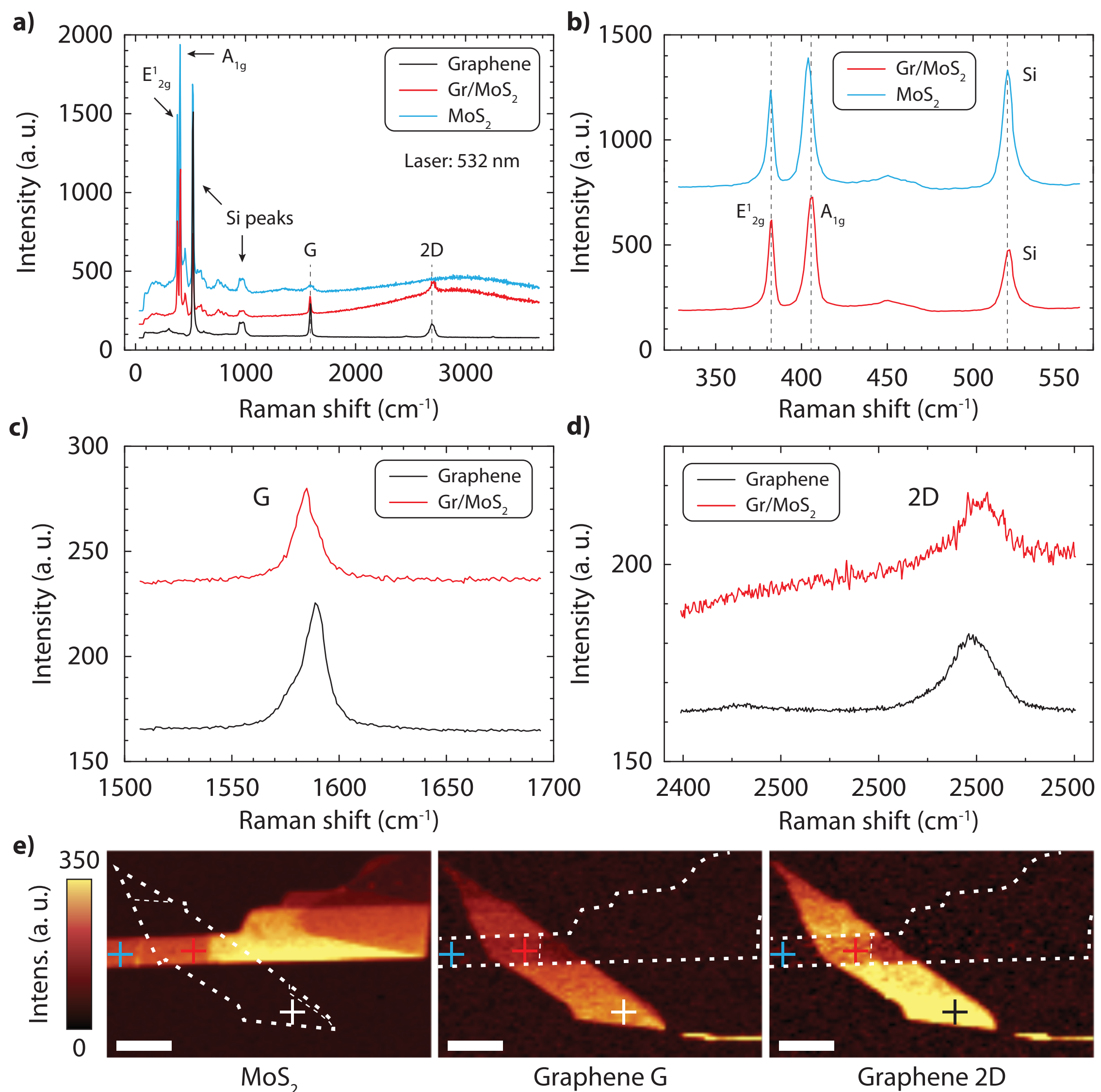

Figure 5.4: Raman spectroscopy of bare and MoS_2-covered graphene excited with a laser wavelength of 532 nm. All spectral curves in a) – d) are offset for clarity. Figs. 5.2 c) and 5.3 a) show the same device. **a)** Full spectra for three positions of the graphene-MoS_2 stack. A strong background appears at higher Raman shifts in the graphene-MoS_2 spectrum. **b)** High-resolution spectrum of the characteristic MoS_2 peaks. **c)** Spectrum of graphene's *G* peak. The *G* peak of MoS_2-covered graphene is slightly shifted compared to bare graphene. **d)** High-resolution spectrum of graphene's *2D* peak with background from MoS_2. **e)** Raman height maps of the MoS_2 and graphene peaks. The outline highlights the graphene flake in the left panel and MoS_2 in the others, the thin dashed lines show changes in the thickness of graphene and MoS_2. The intensities are normalised to the *2D* height map. Due to a focus drift arising from the piezo actuators, the intensities are higher at the bottom of the images. The scale bars represent 5 μm.

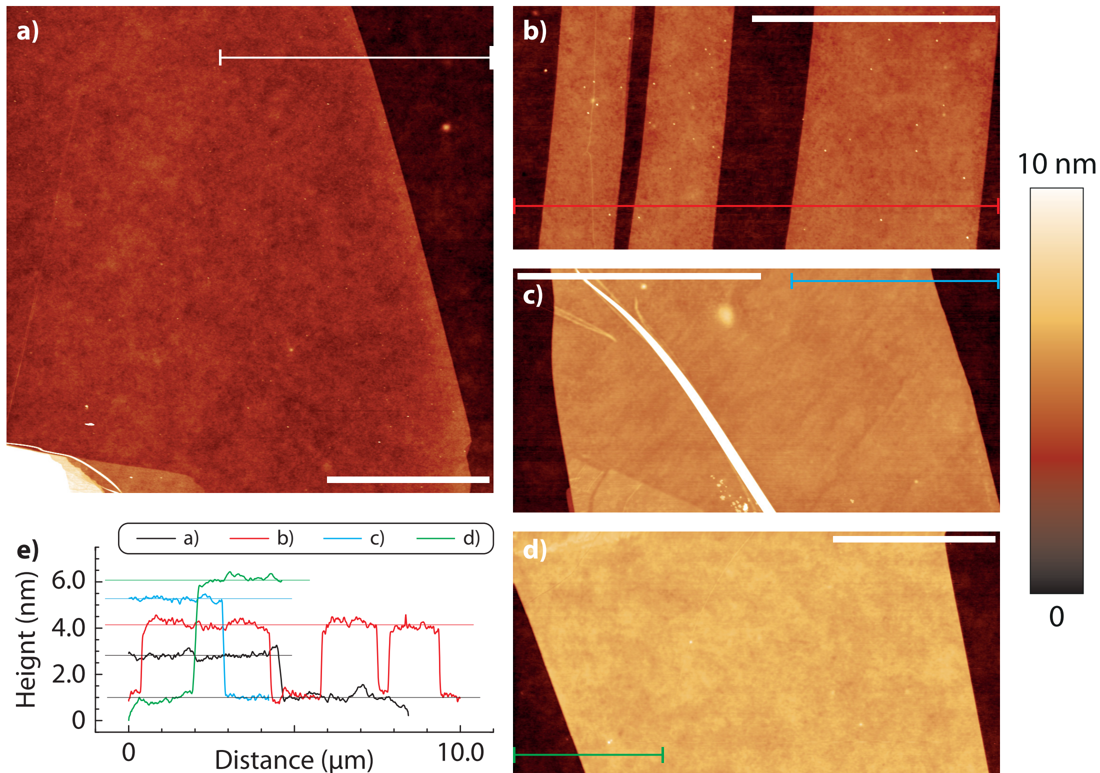

Figure 5.5: AFM images of several freshly cleaved MoS_2 flakes on the transfer wafers. The profiles in e) were recorded along the coloured lines (the black curve corresponds to the white line in a). All scalebars represent 5 μm.

corrugation imposed by the PMMA transfer membrane. However, a possible influence from the AFM tip on the roughness values cannot be excluded: Because of its finite radius, the MoS_2 layers might appear smoother than they are.

5.4.3 AFM measurements on MoS_2 on graphene

Our AFM measurements on the graphene-MoS_2 stacks revealed that bubbles in the MoS_2 layer were present on almost all our fabricated samples (see fig. 5.6). They usually form immediately after depositing the MoS_2 flake onto graphene with the transfer microscope. It is possible that the surface of MoS_2 or PMMA is not perfectly flat and causes these bumps e. g. by trapping air or water between MoS_2 and graphene.

Fig. 5.6 shows the situation before and after transferring MoS_2 onto graphene: An optical micrograph of the pristine MoS_2 flake, residing on its transfer stack, is presented in the left figure in panel a) and the corresponding AFM image in panel b). The flake is very clean, without obvious damages or dirt. The right figure in panel a) and the AFM image in c) illustrate the situation after transferring

R_q MoS_2 (nm)	R_q SiO_2 (nm)	# layers	figure
0.32 nm	0.32 nm	2 or 3	5.5 a)
0.33 nm	0.29 nm	4 or 5	5.5 b)
0.20 nm	0.29 nm	6 or 7	5.5 c)
0.21 nm	0.33 nm	7 or 8	5.5 d)

Table 5.1: Root-mean-square roughness R_q and thickness of several MoS_2 flakes before transfer.

MoS_2 onto graphene: Bubbles are well visible in the right optical image in a); they formed immediately after touching graphene with MoS_2. The AFM profile shows the height of the bubbles which is 32 nm after transfer and even rises to 44 nm after annealing in H_2 (cf. section 5.3.2). Furthermore, the AFM scans reveal that the bubbles moved between MoS_2 and graphene and also merged into larger ones during an additional Ar/H_2 annealing step (identical to the one described in section 5.3.2). Comparing fig. 5.6 c) and d) reveals that this happened exclusively between MoS_2 and graphene.

We observed on several of our samples that the bubbles can easily grow to the same height as the permalloy contacts. Since permalloy is a brittle material, interruptions of the contact (cf. fig. 5.3) can easily be caused when a ferromagnetic electrode is deposited onto such a hillock on MoS_2. Variation of the device temperature, e. g. when cooling the sample before the deposition of permalloy or when cooling the devices in the cryostat, can also lead to broken contacts due to different thermal contractions (see section 5.3.4). Even if the contacts remain intact, the bubbles can cause the electrodes to bend which affects their magnetic domain structure. We found that it is almost impossible to avoid the bubbles when designing the contacts, due to their amount. Further annealing has only a small effect, if any. In some cases, a few bubbles will merge into a bigger one or even collapse, which leads to holes in the MoS_2 layer and thus to an increased risk of transparent contacts between permalloy and graphene.

We believe that the reason for the formation of the MoS_2 bubbles is based on the fact that both materials are hydrophobic and thus bind well to each other: If air or water are trapped between graphene and MoS_2, MoS_2 inflates and the bubbles cannot relax due to the strong binding. Making graphene hydrophilic would reduce these strong forces and should also reduce the amount of bubbles or prevent their formation. Our group is currently looking into possibilities to make graphene hydrophilic which should prevent the strong binding and thus reduce the amount of bubbles, or prevent them altogether.

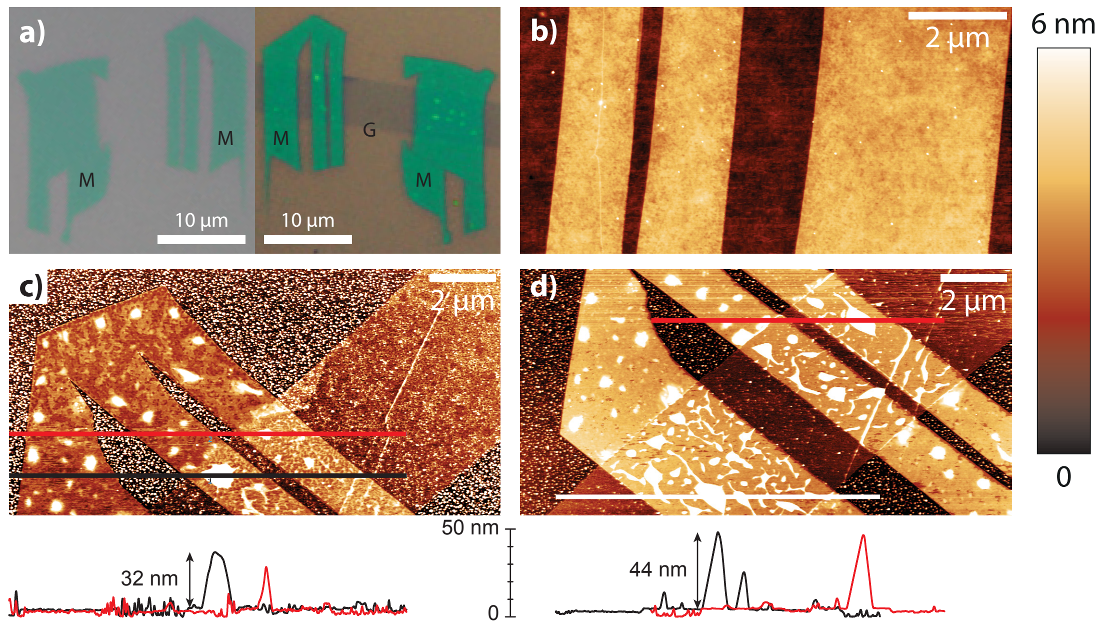

Figure 5.6: a) MoS_2 (M) before (left panel) and after transfer (right) onto graphene (G). The bright spots on MoS_2 in the right panel are bubbles which have formed between the two thin layers (see c and d). Note that the left panel shows the surface of MoS_2 which was later brought in contact with graphene, whereas the right panel shows the opposite surface. **b)** AFM image of the as-cleaved MoS_2 flake in a) on the PVA-PMMA stack. **c)** The same MoS_2 flake, transferred onto graphene and AFM-imaged after dissolving the covering transfer PMMA membrane. The profiles below were taken along the lines with corresponding colours and show the highest bubbles on MoS_2. **d)** The same MoS_2-graphene stack after an additional annealing step. Exclusively on graphene, the bubbles moved around, merged and increased in size during this treatment. The height scale is the same for c) and d).

5.4.4 Transport measurements on bare MoS_2

Since we want to use MoS_2 as a tunnel barrier on graphene, we need to verify that there is no lateral transport through MoS_2 itself, which would run in parallel to graphene. This unwanted transport would reduce the amount of injected spins in graphene and strongly reduce the expected spin signals. Due to band alignment of permalloy and MoS_2, we expect a Schottky barrier at the permalloy-MoS_2 interface (see section 5.2.2). Assuming similar Fermi level pinning for permalloy and Ni, we expect electron injection rather than hole injection [129] for sufficiently high charge carrier energies. If the Schottky barrier is high enough, the electrons will tunnel through MoS_2 into graphene if the MoS_2 layer is sufficiently thin. Hence, we have to choose experimental conditions in our spin injection measurements which favour tunnelling transport.

Using the exfoliation and transfer methods described in section 5.3.2, we transferred thin MoS_2 crystals onto SiO_2 – direct exfoliation onto SiO_2 yielded a low

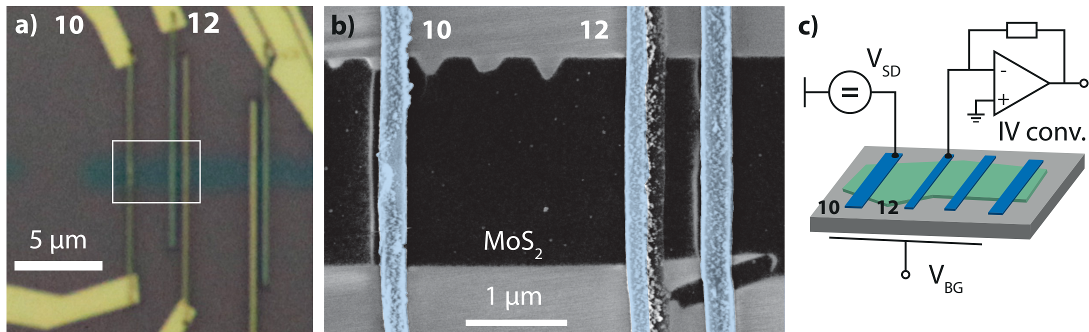

Figure 5.7: a) Optical image of the MoS_2 device with permalloy contacts, out of which contacts 10 and 12 have been working. The permalloy strips were contacted with palladium. The area in the white rectangle was imaged by SEM after the transport measurements (see b). **b)** SEM image of the region in a). The contacts (blue) appear bent because of charging. The dirt next to contact 12 comes from PMMA resist. **c)** Sketch of the device with measurement circuit.

amount of thin flakes and thick flakes deposited in this way could not be thinned down as easily with tape as graphene. The transfer method offered a much better yield. We defined permalloy contacts by electron-beam lithography and fabricated them by electron-beam deposition. In a second lithography step, the permalloy electrodes were contacted with palladium after removing oxidised permalloy at the Py-Pd contact by Ar sputtering. Note that we fabricated these particular devices with a PMMA resist (the three-step process described in section 5.3.3 was introduced shortly afterwards).

We conducted two-terminal $I - V$ measurements on these MoS_2 transistors (cf. fig. 5.7) by supplying a DC bias voltage with a YOKOGAWA YK7651 voltage source and measuring the current with a KEITHLEY 2000 multimeter. The current was amplified with an in-house-built IV converter. The $I(V)$ curves (e. g. fig. 5.8 a) displayed non-linear behaviour. This confirms our expectations that Schottky barriers would form at the interfaces between MoS_2 and permalloy. Our results also revealed that it is not possible to access the valence band, i. e. we could not achieve hole transport in our samples. Das *et al.* [129] observed the same behaviour for high-work function materials, for example Ni and Pt, and concluded that the Fermi levels of the metals are pinned close to the conduction band of MoS_2. For Ni contacts to MoS_2, they determind Schottky barrier heights of 150 meV. From our barriers, we extracted values which are lower, about 20 meV. The extraction of these values is described in detail in appendix B.

The transport over or through a Schottky barrier is described by thermionic emission and thermally assisted tunnelling (the mechanism behind thermionic field emission; cf. section 1.4.1). Thermionic emission allows charge carriers to overcome the barrier if their temperature is high enough. Thermally assisted tunnelling takes place in a barrier which has a triangular shape because of an applied bias or gate. Hot electrons have sufficient energy to tunnel through the

thinner sections of the barrier. Lowering the temperature and conducting zero-bias measurements (e. g. with a lock-in amplifier) will minimise this contribution. Our data exhibit the same trend.

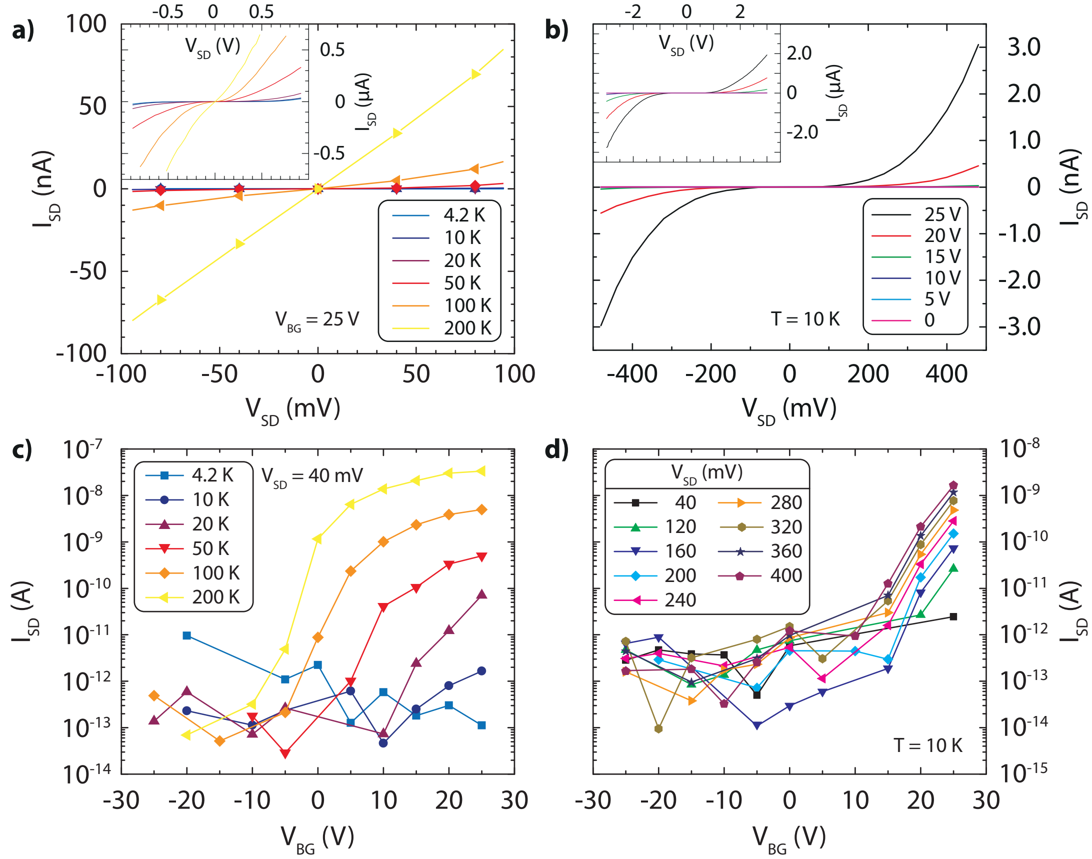

Figure 5.8: Transport measurements on the MoS_2 device from fig. 5.7. **a)** $I-V$ measurements for a fixed back-gate V_{BG} and several temperatures. Most of the current vanishes below 50 K (inset: wider data range). **b)** $I-V$ measurements for fixed temperature and several back-gate voltages. Here, the current essentially vanishes below V_{BG} = 20 V (inset: wider data range). **c)** Temperature-dependent transfer curves at low bias show that transport is only possible for high temperatures or back-gate voltages. **d)** At low temperatures, bias voltages above 40 mV are needed to achieve transport.

Fig. 5.8 a) shows $I(V)$ curves measured in the MoS_2 device in fig. 5.7, taken at various temperatures and at a fairly high back-gate voltage of 25 V. Below 50 K, there is no significant transport anymore. The inset shows that a high bias of 500 mV would be required to establish a current. This essentially yields a set of constraints for our measurements. Lowering the temperature is very easy, since the sample can be cooled down to 1.6 K in the variable temperature insert (VTI) of our ^{4}He cryostat.

From the figures 5.8 c) and d), we learn that no transport takes place in MoS_2 for certain values for the temperature, the back-gate voltage and the bias volt-

age. Especially for back-gate voltages below 15 V and temperatures below 20 K, the figures show only noise coming from the IV converter. These constraints should prevent both thermionic emission and field emission through the Schottky barrier into MoS_2. Hence, we can easily choose suitable conditions for our experiments by conducting zero-bias measurements with a lock-in amplifier at low-temperatures.

It is easily possible to vary the band bending of MoS_2 with the back-gate voltage and to increase electron emission by the temperature. This can enable or disable charge injection into the semiconductor, thus essentially switching between tunnelling or transport through MoS_2. Hence, the applied back-gate voltage could be an interesting experimental handle to increase or decrease the spin injection into graphene.

5.4.5 Conclusion

Our methods for the characterisation of MoS_2 – Raman spectroscopy, AFM and transport measurements – demonstrate that MoS_2 is quite promising as tunnel barrier on graphene: The Raman measurements show that graphene is not strongly influenced by the top layer. No *D* peak appears after transfer, and there is merely a slight change in the *G* and the 2*D* peak.

We learned from AFM measurements that the exfoliation of MoS_2 yields flat and homogeneous thin crystals. Depositing MoS_2 onto graphene, however, seems to cause the formation of bubbles in MoS_2, in the most extreme case with a height of over 100 nm (not shown). The bubbles, as well as folds and ripples, can cause interruptions of the permalloy contacts, as presented in fig. 5.3, when the ferromagnet is deposited. It could also happen that the bubbles break at some point during fabrication, leaving parts of graphene unexposed, which causes direct contacts between permalloy and graphene. We managed to fabricate graphene-MoS_2 devices despite the bubbles, but are currently exploring methods to prevent them from forming in the first place.

Our transport measurements conducted on bare MoS_2 revealed that Schottky barriers are formed at the permalloy contacts. We found that we can easily gate MoS_2 to the electron transport regime, but cannot observe hole transport, in correspondance with the literature. While simple band structure considerations suggest that permalloy, due to its work function, should be a hole injector, it is apparently Fermi level pinning which aligns the metal and MoS_2 such that the observed electron injection is favoured [129].

Keeping the energy of the charge carriers low enough such that they cannot enter the conduction band of MoS_2, which can easily be achieved by measuring with a low bias voltage at low temperatures, should enable tunnelling through MoS_2

when we place a thin layer of the semiconductor on graphene. The Schottky barrier height can be tuned with back-gate and temperature such that the influence of the barrier resistance on spin transport through graphene can be investigated.

5.5 Electrical measurements on graphene-MoS_2 stacks

5.5.1 Determination of the contact resistance

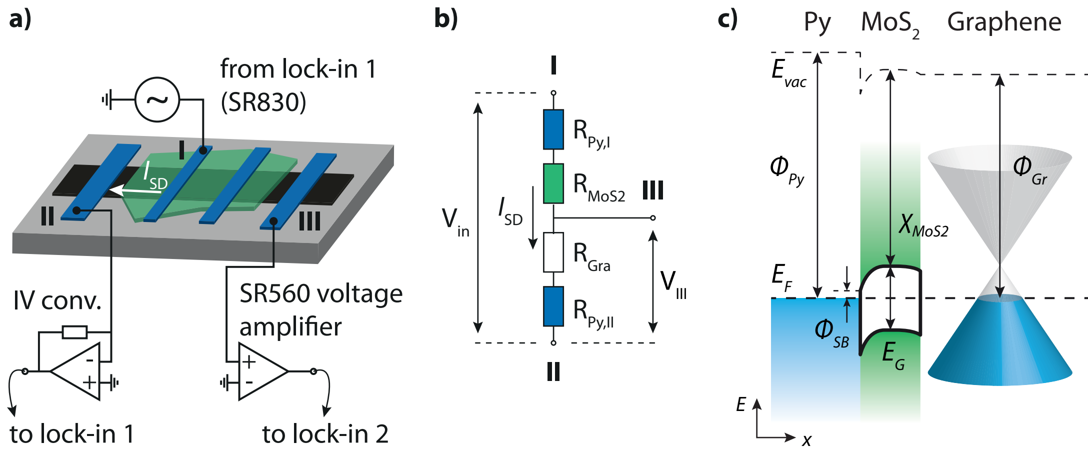

Figure 5.9: Three-terminal measurement technique. **a)** Drawing of a graphene-MoS_2 device with direct contacts to graphene and contacts on MoS_2 on graphene. A current I_{I-II} flows between contacts I and II, and contact III probes the potential of graphene where the current is injected. **b)** Resistor model for the three-terminal measurements. Here, we assume that the contact injects the current I_{I-II} homogeneously into the graphene strip and that there is no lateral transport in MoS_2. **c)** Band scheme of permalloy-MoS_2-graphene, schematically taking Fermi level pinning at the Py-MoS_2 interface into account.

Due to the Schottky barriers at the permalloy-MoS_2 interface (see section 5.4.4), we do not expect charge injection into the conduction band of MoS_2 for low T and V_{SD}. In this regime, the electrons tunnel through sufficiently thin MoS_2 layers, and we should be able to see transport taking place uniquely in graphene for values of V_{BG} which correspond to MoS_2's transport gap.

Using three-terminal measurements, it is possible to gain information about both the contact resistance and graphene's resistance in our devices. The measurement scheme is illustrated in fig. 5.9 a): We applied a voltage V_{in} between source (contact I) and drain (II) with the voltage source of a lock-in amplifier[4]. The

[4]Stanford Research SR830

current I_{SD} was amplified with an in-house-built I-V converter at contact II and measured with the same lock-in. At contact III, we measured V_{III}, the electrostatic potential of graphene below MoS_2, where the current was injected into graphene. V_{III} was amplified with a voltage preamlifier[5] and measured with a second lock-in amplifier which we frequency-synchronised with the first one. With the assumption that the barrier is homogeneous and that there is no lateral transport through MoS_2, we defined the contact resistance R_C and the resistance of graphene, R_G (see fig. 5.9 b) in the following way:

$$R_C := R_{\mathrm{Py,I}} + R_{\mathrm{MoS_2}} = \frac{V_{\mathrm{in}} - V_{\mathrm{III}}}{I_{\mathrm{SD}}} \tag{5.1}$$

$$R_G := R_{\mathrm{Gra}} + R_{\mathrm{Py,II}} = \frac{V_{\mathrm{III}}}{I_{\mathrm{SD}}}, \tag{5.2}$$

with

$$R_{\mathrm{2T}} = R_C + R_G = \frac{V_{\mathrm{in}}}{I_{\mathrm{SD}}}. \tag{5.3}$$

Note that the contact resistance R_C below contact I is a sum of the actual resistance of the MoS_2 barrier, $R_{\mathrm{MoS_2}}$, and a contribution $R_{\mathrm{Py,I}}$ from the permalloy lead of contact I. If our assumptions about the transport through MoS_2 are correct, $R_{\mathrm{MoS_2}}$ should be the tunnelling resistance through the barrier. However, since the Schottky barrier can be thermally activated, it will have a different temperature dependence than the resistances of our oxide barriers (cf. section 1.4). The measured resistance R_G consists of the permalloy lead of contact II and the resistance of graphene.

5.5.2 Contact resistances in graphene-MoS_2 heterostructures

One of our graphene-MoS_2 devices is shown in the coloured SEM image in fig. 5.10 a). The device was fabricated from single-layer graphene covered with a fairly thick (estimated 10 layers) MoS_2 flake by transfer. We deposited permalloy contacts which were written into PMMA resist in a single lithography step. Contacts 7, 9, 10, 17 and 20 were deposited directly onto graphene. We also placed several contacts on MoS_2. Contacts 11/5, 12, 2 and 1/16 were deposited to form a non-local spin valve, but some of them broke when the device was cooled down or while measuring.

After cooling our device to 2 K, we conducted three-terminal measurements on the remaining working contacts. Examples are presented in Fig. 5.10 b) and c). Panel b) shows the back-gate dependence of the contact resistance R_C measured

[5]Stanford Research SR560

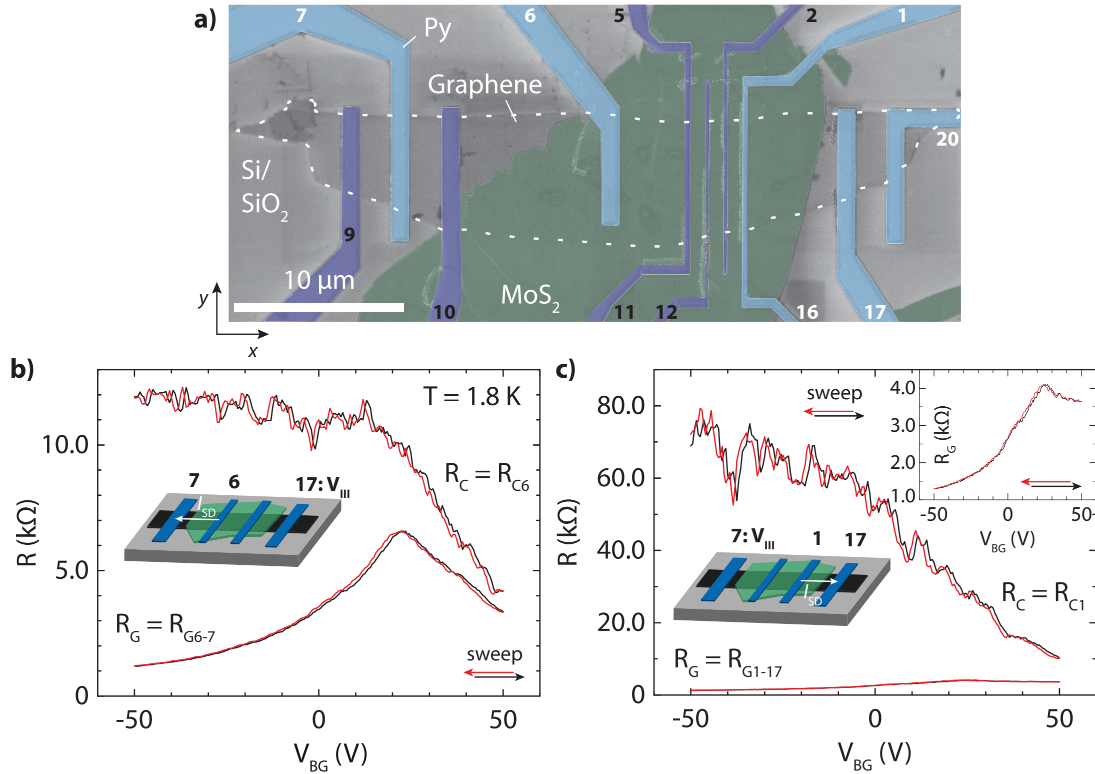

Figure 5.10: Three-terminal back-gate measurements on a graphene-MoS_2 sandwich (device "GMoS-01"). **a)** False-colour SEM image of the device. MoS_2 is green, permalloy blue or purple, and both graphene (outlined) and the substrate are uncoloured. The purple contacts with the black numbers had initially been working at room temperature but broke down during cool-down or during the low-temperature measurements. **b)** Low-temperature back-gate sweep with V_{2T} applied between 6 and 7 and V_{III} measured at 17. R_C and R_G differ strongly in the hole transport regime, R_C displays reproducible fluctuations. **c)** Three-terminal measurements with a different injection contact. The resistances of graphene and MoS_2 can be separated as well and the contact resistance displays fluctuations similar as in b).

on the source contact 6, as well as R_G of the graphene piece between source and drain contacts 6 and 7, where 7 lies directly on graphene. In c), R_C of contact 1 and R_G between 1 and 17 are presented in dependence of the back-gate voltage V_{BG}. V_{BG} was varied from negative to positive values (black curves) and back (red curves). R_C in panel c) is much higher than on the other junction in panel b). This is due to the smaller cross-section area of contact 1 and graphene.

The back-gate sweeps reveal that R_C and R_G, which were obtained as described in 5.5.1, show different behaviour: Similar to fig. 5.8 c), R_C is more or less constant for V_{BG} below a certain threshold ($\sim$ 15 V for the graphene-MoS_2 device) and drops to lower values above a V_{BG} about 20 V. This shows that graphene does not screen the electric field and that we can gate MoS_2 through graphene. R_G displays a clear Dirac point in these measurements at about 25 V, i. e. graphene is strongly *p*-doped. Furthermore, the resistance traces of graphene show less fluctuations than the contact resistances. This clear separation of R_C and R_G justifies our method described in section 5.5.1.

We observed that an MoS_2 top layer can dope the graphene sheet underneath. Fig. 5.11 shows a graphene-MoS_2 device, contacted with permalloy, where MoS_2 is covering some of graphene's surface. The Dirac points of the conductivities measured between the contact pairs in a) correspond to various back-gate voltages. Some of them are also shallower than others. This is a sign that doping is not equal for the measured graphene pieces, but it rather seems to be caused by dopants which are distributed differently between different contact pairs. These can be for example impurities residing on the surface of MoS_2.

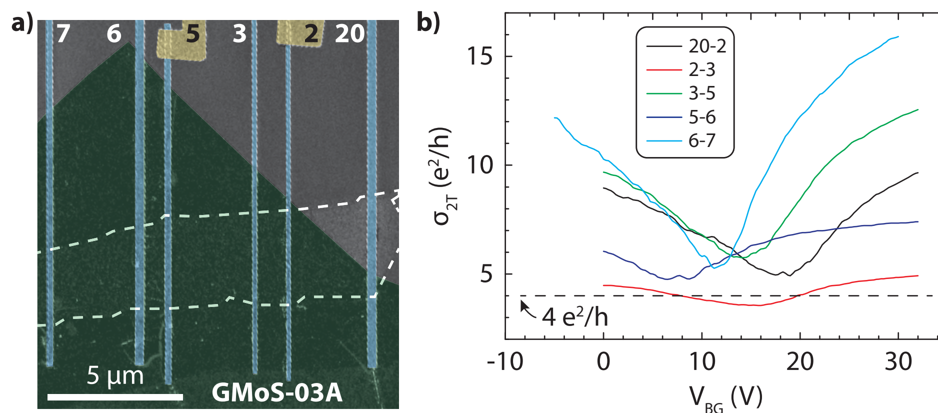

Figure 5.11: a) Graphene-MoS_2 device GMoS-03A contacted by permalloy (blue) and Ti/Au (yellow). The outline of graphene is given by the broken line. MoS_2 is coloured green. **b)** Two-terminal conductivities measured at the contact pairs in a). The Dirac points are at different values for V_{BG}, hinting at doping introduced by MoS_2.

5.5.3 Conductance fluctuations

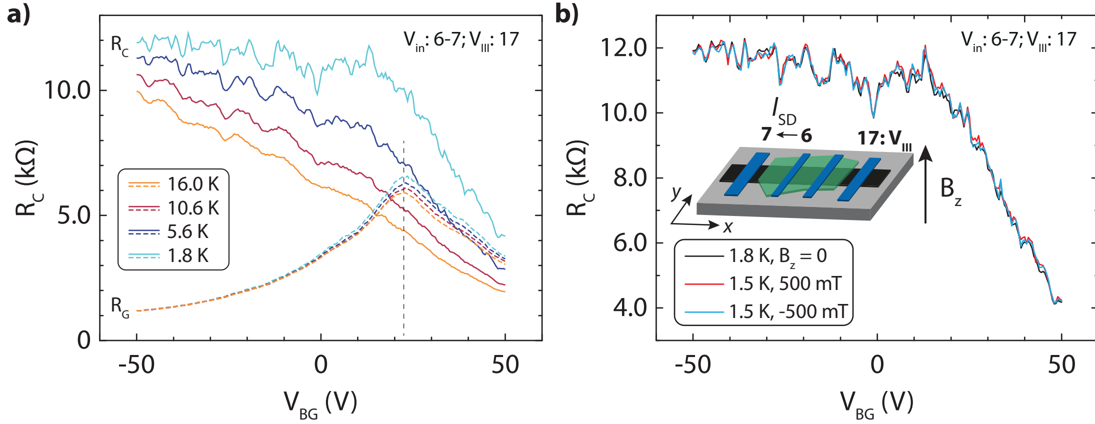

Figure 5.12: Device GMoS-01: A more detailed analysis of the resistance fluctuations on contact 6 from fig. 5.10 a). **a)** Temperature dependence of the back-gate measurements for R_C (solid curves) and R_G (broken curves). The curve of R_C at 1.8 K was already presented in fig. 5.10. The daashed line marks the Dirac point. **b)** A perpendicular magnetic field $B_z = \pm 500\ mT$ has no influence on the fluctuations.

The back-gate scans presented in fig. 5.10 display large temperature-dependent fluctuations of R_C which can arise from the MoS_2 layer or from the part of graphene directly below the contact – due to the clear separation of R_G and R_C, transport in the graphene piece between source and drain contacts can be excluded as cause for the fluctuations. We investigated their temperature dependence (fig. 5.12 a) and tested whether an external B_z field applied perpendicular to the sample has any influence on them (fig. 5.12 b).

The temperature dependence of the back-gate measurements shows that the fluctuations have largely disappeared when heating to 16 K. This is comparable to the situation in MgO, where the fluctuations are washed out but can still be discerned at 15 K. Similar to the measurements on bare MoS_2 in section 5.4.4, the resistance of MoS_2 decreases with increasing temperature. R_C depends almost linearly on the back-gate voltage. There are also several values where the curves for R_C and R_G for a particular temperature are crossing. At these points, the MoS_2 barrier becomes less resistive than the graphene strip.

We could not observe any magnetic-field dependence of the resistance fluctuations for $|B_z|$ as high as 500 mT. On the other hand, since we clearly separated the resistances of graphene and MoS_2, and since we observe the fluctuations only in the latter, this is not surprising. Fig. 5.13, however, illustrates that the resistance fluctuations are specific to a particular contact: Fig. 5.13 a) shows the V_{BG} dependence of the source-drain current flowing between contacts 6 and 17 (black trace) and 6 and 7 (red), both obtained in separate measurements. In both

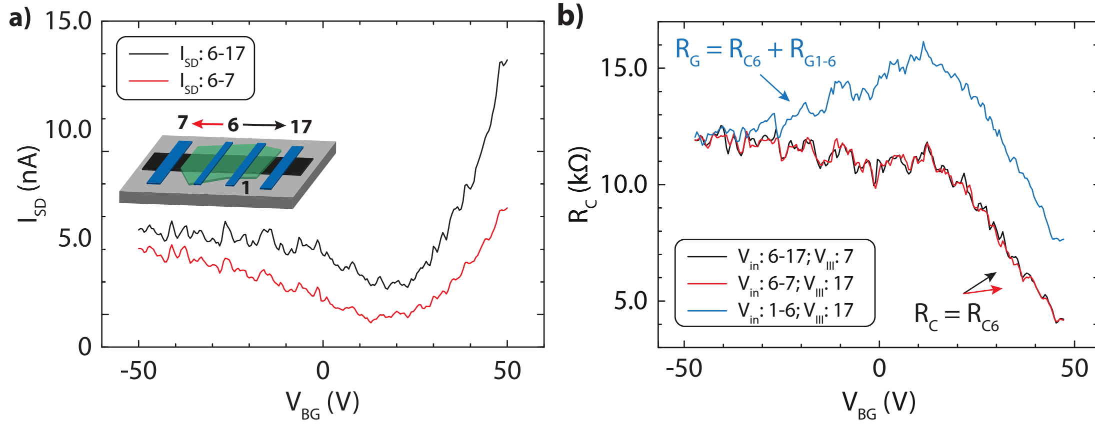

Figure 5.13: Closer examination of the resistance fluctuations on device GMoS-01. **a)** Both back-gate dependent traces for the source-drain current between contacts 6-17 (black arrow and curve) and 6-7 (red) display the same fluctuations. The dip is the Dirac point of the graphene sheet below MoS_2. **b)** Comparison of MoS_2 resistances extracted from three-terminal measurements. The blue curve shows the sum of the resistances of the graphene piece between contacts 1 and 6 and the MoS_2 layer's resistance below 6. All those values have the same value for negative back-gate voltages. In addition, all three curves show a similar fluctuation pattern for V_{BG} up to $\sim$ 15 V.

cases, an AC bias voltage was applied to contact 6[6]. Both traces show a dip near V_{BG} = 20 V which can be identified as the Dirac points in the respective parts of graphene. Far away from the Dirac point, at low V_{BG}, both curves show the same fluctuations. Since the highest resistor in the series – cf. fig. 5.9 b) – is the resistance of MoS_2, i. e., the contact resistance of contact 6, it defines the fluctuations. Hence, they most probably have their origin in MoS_2 or in the interfaces between permalloy and graphene.

Other data also show that the fluctuations are linked to a particular source contact: Fig. 5.13 b) displays three separately obtained resistance traces which all involve contact 6. The black and red curves were obtained from the traces in a) by using eqn. (5.1) on the measured data of V_{in} and I_{SD}. Here, contact 6 was used as source. For the blue curve, contact 6 served as drain, contact 1 as source. In this case, the three-terminal measurements yield the contact resistance $R_{C,1}$ of contact 1 (not presented) and, as shown in the figure, the resistance $R_G = R_{G,6-7} + R_{C,6}$ of the graphene piece between 1 and 6 in addition to the contact resistance of MoS_2 below contact 6. For negative gate voltages, all traces are subject to the same fluctuations. This further backs our observation that these fluctuations come from MoS_2 itself or from the layer interfaces.

[6] R_C and R_G in fig. 5.10 b) were calculated from the data of the red curve in fig. 5.13 a)

5.5.4 Conclusion

By choosing suitable experimental conditions, such as low temperatures around 2 K and using a lock-in amplifier for zero-bias AC measurements, we found that we could indeed measure the resistances of graphene and MoS_2 separately in some of our devices. In these situations, we observed a clear Dirac point in graphene (cf. e. g. fig. 5.10 a and c). The resistance of graphene also displayed very weak fluctuations, in contrast to the contact resistance.

Using three-terminal measurements, we investigated the resistance fluctuations which were of similar appearance to those we had found previously on our Al_2O_3 and MgO samples. They depended on the temperature of the device, but a perpendicular magnetic field B_z as high as 500 mT did not influence them. Upon comparing several data sets, we found that the fluctuations were linked to a specific contact and could be caused at the interface between permalloy, MoS_2 and graphene or in MoS_2 itself.

Back-gate scans of the currents and resistances for several contact configurations from separate measurements revealed that identical fluctuations appeared when the same contact was used as either source or drain. We can interpret these fluctuations as a signature of this particular contact or the part of MoS_2 through which the electrons move or tunnel.

5.6 Spin-valve measurements

5.6.1 Three-terminal measurements

On device "GMoS-01" (see fig. 5.10), we investigated the dependence of the three-terminal resistances on a magnetic field B_y applied in parallel to the permalloy contacts. These data are plotted in fig. 5.14.

When applying a voltage between contacts 6 (source) and 7 (drain) on the device, we observed large reproducible jumps of the contact resistance R_C of about 200 Ω when sweeping a magnetic field B_y (black and red curves in fig. 5.14 a). Apart from a small B_y offset of about +4 mT, the switches are symmetric about $B_y = 0$. To illustrate the reproducibility, three consecutive trace pairs are plotted in the figure. Panel 5.14 c) shows another set of such pairs for a voltage applied between 6 (source) and 17 (drain) with very similar results. The source contact was the same in both sets of traces. With a distance of about 10 μm, the other contacts are too far away to play a significant role. This rules out spin transport and the signal could have its origin in the contact resistance.

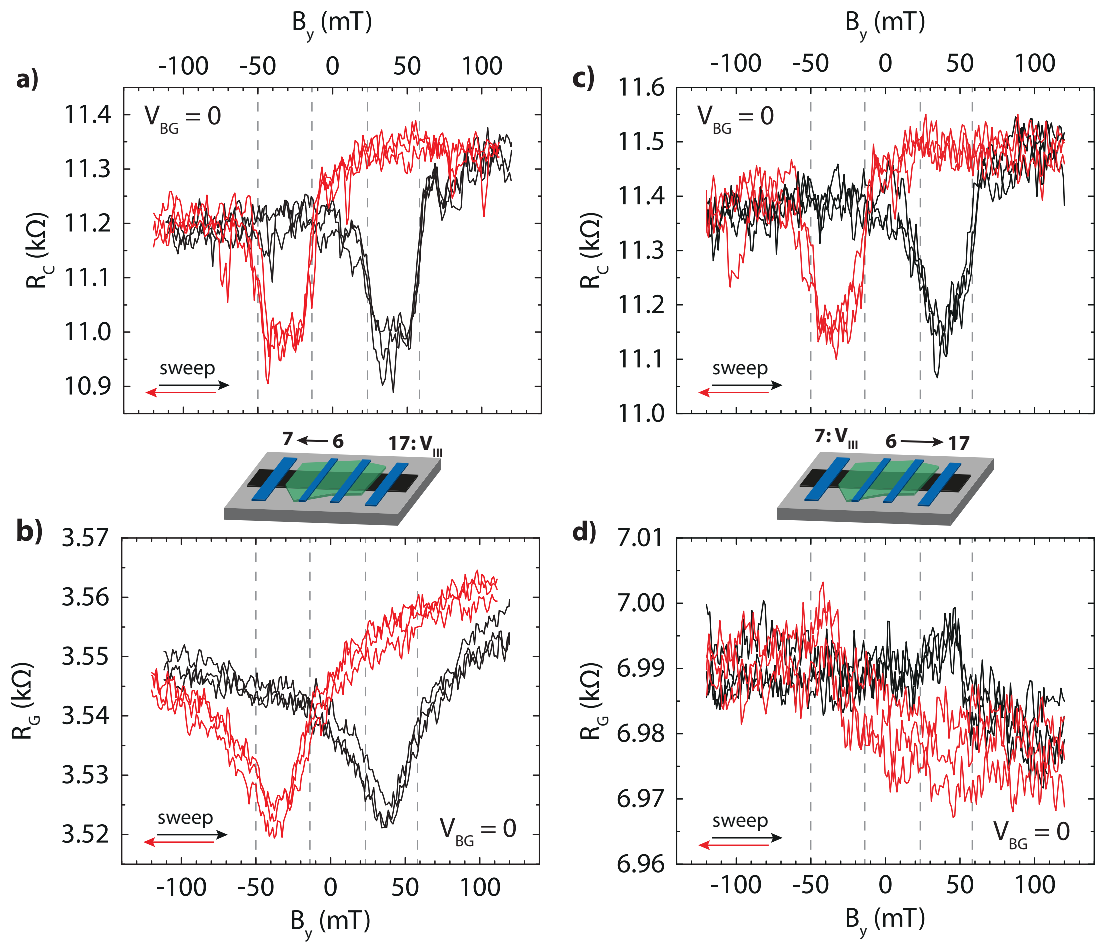

Figure 5.14: B_y dependence of the contact resistance R_C and graphene's resistance R_G obtained by three-terminal measurements (cf. fig. 5.9). The device sketches between the graphs show the used contact scheme. **a)** Three consecutive trace pairs (sweep and back-sweep of B_y) of R_C of contact 6. An AC voltage V_{in} = 100 μV was applied between 6 and 7. R_C exhibits distinct and reproducible jumps of about 200 Ω. **b)** R_G of the graphene piece between contacts 6 and 7 also shows a reproducible and B_y-dependent signal, albeit with a small change of about 30 Ω. The dashed lines correspond to the jumps in a). **c)** Results for R_G for opposite direction of current flow, i. e. with an AC bias of 100 μV applied between contacts 6 and 17. **d)** R_G of the graphene piece between contacts 6 and 17. The resistance is higher than in b) and the magnetic dependence somewhat resembles a TMR signal. The dashed lines correspond to the jumps in c).

A clear and reproducible effect can also be seen in the resistance curves R_G in b) and, to a small extent, in d). The traces in d) do not resemble the dips from b) at all, but seem to show small upward jumps. It is not clear what causes the magnetic switches in both R_C and R_G. The involved contacts 6, 7 and 17 are about 1 μm wide from which we would expect switching fields below 20 mT (cf. fig. 1.3). It is possible that this particular contact configuration of the permalloy electrodes, which are partly aligned in a 45° angle to the external B_y field (see fig. 5.10 a), is responsible for these switches.

The curves presented in fig. 5.14 were recorded with zero applied back-gate. At other values for V_{BG}, the magnetic signal disappeared or showed a hysteresis-like curve similar to fig. 4.10. Recording a new trace at $V_{BG} = 0$ showed the large jumps from figs. 5.14 a) and c) again.

5.6.2 Four-terminal non-local measurements

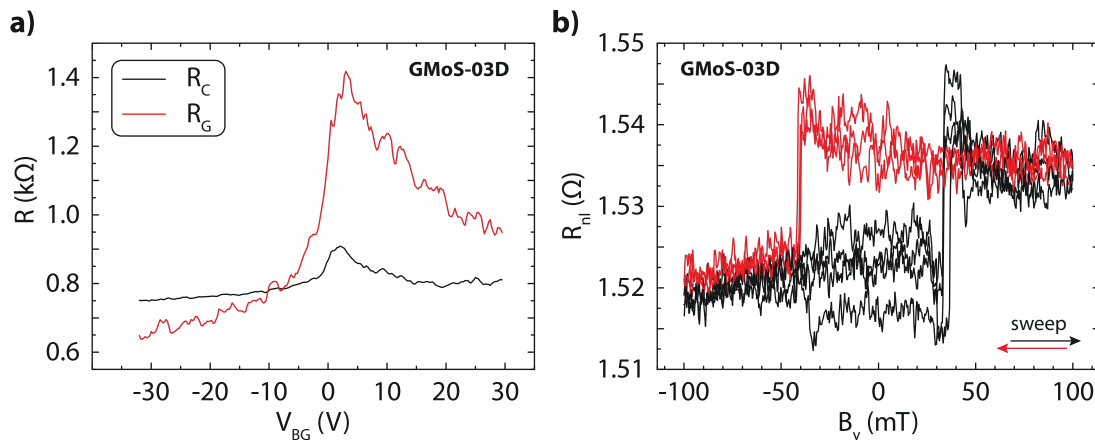

Figure 5.15: a) Three-terminal measurement of R_C and R_G on very thin (i. e., transparent) MoS_2 on graphene on device GMoS-03D. The device was prepared alongside the one shown in fig. 5.11 a) and looks similar. **b)** Non-local magnetic measurement on the same device. The jumps of ΔR_{nl} of about 200 mΩ are well reproducible.

We fabricated non-local spin valves by placing MoS_2 flakes of varying thickness on graphene. Fig. 5.11 a) on p. 98 shows such a device where several ferromagnetic strips were placed on MoS_2 sitting on graphene. The ferromagnetic permalloy strips were written by electron beam lithography using ZEP520A resist and deposited by electron beam evaporation. In a second step, the strips were contacted by palladium after sputtering away oxidised permalloy.

In all of these samples, we observed that the contact resistance, when measured with the method described in section 5.5.1, was considerably lower than in our

first device presented in section 5.5.2. It is very likely that our MoS_2 flakes contained cracks or even pinholes which caused direct contacts between permalloy and graphene, resulting e. g. from the different thermal expansion of permalloy and MoS_2, as discussed in section 5.3.4. As an example for the low resistances, fig. 5.15 a) shows R_C and R_G from device “GMoS-03D”, calculated with the method of section 5.5.1. Both R_C and R_G have low values around 1 kΩ. The maximum near $V_{BG} = 5$ V in both curves could mean that there was no tunnelling transport, but rather a direct contact between permalloy and graphene.

We recorded non-local spin signals on device “GMoS-03D” with these low contact resistances. All of them showed single jumps similar to those observed previously in devices with MgO barriers (see section 4.4.4). These might correspond to a ferromagnetic electrode with a pinned magnetisation. The non-local resistances jumps ΔR_{nl} are very low, which is most probably a consequence of the low contact resistances. In some curves, additional smaller jumps can be seen, e. g. the ones at about 45 mT in fig. 5.15 b). It is possible that there are several magnetic domains along the injector or detector contact of the spin valve which are switching at different B_y. Since only few of the contacts were working, the jumps could not independently verified by AMR measurements.

5.6.3 Comparison with data from other barriers

A comparison between the magnetic data from this section with data from the TiO_2-MgO or bare MgO and the Al_2O_3 barriers is presented in appendix D.

5.6.4 Conclusion

While we were not able to obtain “textbook” non-local spin-valve signals similar to those we observed on our MgO samples (see fig. 4.9), we managed to reproduce large B_y-dependent resistance switches of about 200 Ω in three-terminal measurements. Especially the resistance jump near 50 mT cannot be explained by a change in magnetisation, because the involved contacts are over 1 μm wide and would thus be expected to switch at much lower fields. Since we know the resistances of graphene (R_G) and the injector contact (R_C) very well from our electrical three-terminal measurements, we know that the switch occurs in the contact resistance. This is a very interesting result which justifies further investigations.

Non-local resistances in other graphene-MoS_2 devices did not exhibit these strong switchings, but were, in fact, very low. This can be explained by low contact resistances, most probably caused by holes and fissures in the MoS_2 flakes. A

rippled transfer PMMA membrane (cf. section 5.4.3) or different thermal expansion of the involved materials (cf. section 5.3.4) could be responsible for these damages.

5.7 Summary

In order to avoid the deposition of oxides onto graphene, which can be difficult to control, we changed our barrier material to MoS_2, a layered dichalcogenide. There are several other possible candidates which can be exfoliated like graphene to yield large flakes of uniform thickness, notably the insulator hexagonal boron nitride (h-BN). However, MoS_2 offers a much better visibility with an optical microscope and thus also the possibility to reproducibly select flakes of similar or equal thickness. The flakes were transferred onto graphene using a transfer microscope which was built in our group and allows good alignment between the MoS_2 and the graphene flake.

Structural investigations, conducted by Raman spectroscopy and AFM measurements, showed that MoS_2 itself is indeed homogeneous over large distances and that it does not damage graphene. However, we observed that large bubbles, which could easily achieve heights of 30 nm, can form on MoS_2 when it is placed on graphene. We presume that strong binding forces between the two layers prevent a homogeneous deposition. While not harmful to graphene, the bubbles can lead to breaks in the permalloy contacts. If these breaks occur on graphene, as e. g. seen in fig. 5.3, the permalloy strip cannot be used as contact anymore in most cases. Its broken end will cause magnetic stray fields which can destroy the polarisation of the injected spins. Furthermore, these cracks also increase the risk of direct contacts between MoS_2 and graphene.

Electrical measurements on MoS_2 confirmed that Schottky barriers are forming at the interface with permalloy. In agreement with similar experiments reported in the literature [129], we found that we could only access the electron transport regime in our experiments, a consequence of Fermi level pinning in MoS_2. With our usual experimental conditions, i. e. a base temperature of 4 K and the choice of zero-bias measurements, we observed that the Schottky barrier in our permalloy-MoS_2 devices was high enough to prevent charge carrier injection into MoS_2. The dependence of the Schottky barrier height (i. e., the contact resistance) on the device temperature or an applied back-gate voltage should give an interesting experimental handle, since it allows to investigate the dependence of the spin injection on the contact resistance.

Using three-terminal measurements, we observed on device GMoS-01 that we could indeed influence the contact resistance in graphene-MoS_2 devices separately from graphene's resistance when varying the back-gate voltage. This was

not only visible in the different back-gate dependences of R_C and R_G, but also from the very pronounced reproducible fluctuations in the contact resistance. Like the oscillations we observed in our samples with MgO and Al_2O_3 barriers, they smoothen out with at increased temperatures. For magnetic fields B_z = 500 mT perpendicular to graphene, no change in the oscillations was visible. In fact, they seemed to arise from the contact itself, because we always observed the same fluctuations when the same contact was present in the measurement as either source or drain. The bulk of graphene, on the other hand, never showed such fluctuations, at least not of significant amplitude.

In our magnetic measurements, we observed unusually large switches on device GMoS-01. Because of the particular configuration of the contacts in the system, we can exclude a spin-valve effect. More data is necessary to fully explain our results. We designed samples with non-local spin valve geometries as well and measured non-local signals with single jumps and a hysteretic behaviour, hinting at an electrode with pinned magnetisation. The very low spin signals are a consequence of the low contact resistances most probably caused by pinholes or transparent contacts.

Initially, the fabrication of the MoS_2-graphene samples showed a higher yield in working devices than the oxide deposition. However, two limiting factors presented themselves; apart from the aforementioned bubbles, the exfoliation yield of the MoS_2 flakes can vary greatly between exfoliation processes and might depend on the used bulk MoS_2 piece. An improvement of the exfoliation method could help tackling this problem.

Chapter 6

Summary and outlook

During the course of this thesis we explored several methods to create high-quality tunnelling barriers on graphene which allow for efficient spin injection. Ideally, tunnelling barriers are very thin, yet very homogeneous insulators. Achieving both of these aims at the same time is not a straightforward task: Thin layers tend to be very inhomogeneous, especially on graphene substrates which have a very high surface energy.

As our first choice, we decided to grow barriers from aluminium oxide, a widely used high-κ oxide in the semiconductor industry, using atomic layer deposition for well-controlled growth. Because of its highly inert nature, graphene required a pre-treatment prior to the deposition. We compared results for both NO_2 deposition and TiO_2 seeding and found the latter to be the better alternative in terms of oxide homogeneity, barrier resistance and overall device stability. Our AFM measurements showed that the NO_2-initiated growth yielded barriers with higher roughnesses than for TiO_2 seeding. We deduced from these results that the latter are more homogeneous. Raman spectroscopy revealed that the deposited NO_2-Al_2O_3 did not introduce damages to graphene.

We observed non-linear $I - V$ characteristics of our tunnelling devices, as well as tunnelling resistances which were increasing with decreasing sample temperature. Especially the latter is a signature for tunnelling-dominated transport. RA products obtained on NO_2-functionalised graphene were spread over more than an order of magnitude, which corresponds well to the high roughness observed with AFM. On the TiO_2-seeded barriers, we could measure clear and reproducible spin signals. Due to the limited stability of our samples and a high inhomogeneity in the RA products, we decided to change the barrier material.

During the last years, MgO has emerged as well-suited tunnel oxide for the spin injection into graphene. We fabricated graphene spin-valves with tunnelling barriers from TiO_2-seeded and also bare MgO and characterised them with various methods. Raman spectra of graphene covered with electron-beam-deposited MgO showed that the oxide does not cause defects. AFM measurements on both seeded and bare MgO layers revealed an overall lower roughness than on our Al_2O_3 layers. The measured resistance values were also more uniform for

MgO than for Al_2O_3. We were able to conduct non-local spin-valve measurements and also observe spin precession in graphene. From the available data, we could extract a rough estimate of the spin polarisation P_T, between 5 % and 30 %. Compared with the literature, this large value range corresponds to transparent or pinhole-dominated barriers.

The thickness of the MgO layers is very hard to control. We observed that the actual thickness of the deposited MgO seems to increase over time, which is very likely caused by cross-contamination in the evaporator. Given the strong dependence of the barrier resistance on its thickness, small variations can quickly create fully insulating oxides, as observed in our case. This and the general lack of sample reproducibility caused us to choose an altogether new approach.

Using crystalline, thin layered materials such as h-BN or MoS_2 can avoid most of the problems described above: Due to their high crystalline order, these thin layers are expected to show a much higher homogeneity than in-situ-grown oxides. Within certain boundaries, their thickness can also be controlled by selecting suitably thin flakes. For our subsequent experiments, we chose MoS_2 as tunnel barrier because it can be exfoliated like graphene and is better visibile in an optical microscope than h-BN.

MoS_2 was transferred onto graphene, followed by the usual lithographic fabrication of the electrodes. We observed temperature-dependent and B-field-independent conductance fluctuations in MoS_2, similar to the ones previously seen in Al_2O_3 and MgO. Using three-terminal measurements, we were able to trace their origin to the contacts. Their independence of an external B field excluded UCF in graphene as explanation. Hence, charging effects in the barrier were probably responsible for this behaviour. The three-terminal measurements also demonstrated that we did not observe transport in the MoS_2 parallel to graphene: The resistances of both graphene and MoS_2 could be well separated and both showed their characteristic conductance traces in back-gate scans (Dirac point for graphene, Schottky characteristics for MoS_2).

Three-terminal spin-valve measurements showed comparably large spin signals of about 200 Ω on one particular sample. Their precise origin could not be found, but the particular shape of the ferromagnetic contacts may be responsible for these signals. Non-local spin-valve measurements on other fabricated devices showed single magnetic jumps, similar to the ones observed in our samples with oxide barriers. The spin signals were quite low, probably caused by shorts between the contacts and graphene. As of this date, other MoS_2-related spin-valve measurements have not been reported in the literature yet.

Depositing MoS_2 on graphene can also lead to the formation of large and numerous bubbles. They appear immediately after transfer and could be observed on almost all our samples. A possible explanation is that both graphene and MoS_2 are hydrophobic and thus strongly bond to each other. An MoS_2 layer

which has ripples from an insufficiently flat transfer PMMA membrane cannot smoothen because of the strong bonding. Further experiments on this improved heterostructure will ultimately show if MoS_2 is a feasible tunnelling barrier for graphene-based spintronics and will offer better control over the barrier homogeneity and thus higher degrees of spin polarisation upon injection.

Appendix A

Lithography issues

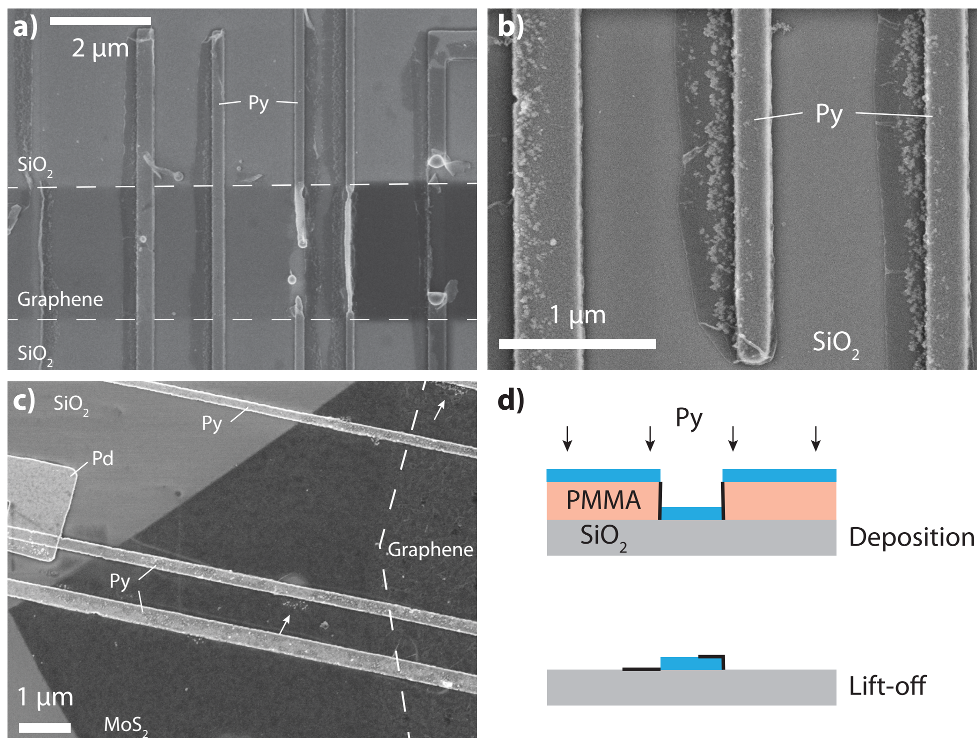

Figure A.1: a) and **b)** SEM images of permalloy strips on SiO_2 and graphene. The shades next to and on the Py contacts are residual dirt which remained on the sample after lift-off. The dirt appears when PMMA is used as electron-beam resist and is caused by an insufficient undercut (see d). **c)** A more sensitive resist, ZEP520A, yields much cleaner strips with only little residual dirt, highlighted by the arrows in the figure. **d)** Origin of the dirty ribbons: In a resist (pink) with a small undercut or even rectangular walls, material (black) is deposited on the walls as well and remains on the surface after lift-off.

In several cases, our permalloy strips seemed to be accompanied or covered by dirt which is shaped like a ribbon. Figs. A.1 a) and b) show images of such strips. We could observe that the width of the dirt ribbons corresponded in most cases to the chosen thickness of our PMMA resist (see A.1 d). The dirt ribbons only

appeared after permalloy deposition and were also observed earlier in our group (see Aurich [17]).

We concluded that the PMMA resist does not form a sufficiently large undercut. In this case, the hot, deposited permalloy comes into contact with the resist wall and cross-links it or even bonds to it. Especially the latter case can affect spin transport in graphene when it is spread over the graphene flake because this mixture of permalloy and PMMA is expected to have magnetic properties.

Julia Samm and Jörg Gramich from our group have found a way to circumvent this problem by choosing a different resist. ZEP520A[1], diluted with anisole, is more sensitive to electron-beam irradiation than PMMA, which leads to a larger undercut. After using this resist for lithography we have not observed dirt next to the contacts anymore (see fig. A.1 c).

[1] ZEON CORPORATION, `http://www.zeonchemicals.com`

Appendix B

Schottky barriers at the permalloy-MoS_2 interface

From temperature-dependent source-drain measurements (fig. 5.8), we calculated the activation energy of the Schottky barriers. Our data show signatures of thermionic emission similar to the data in [142]. Since we expect the behaviour of the Schottky barrier to be governed by the Richardson equation (cf. section 1.4.1),

$$J_n \propto T^2 \exp\left(\frac{q\varphi_B}{k_B T}\right), \tag{B.1}$$

the data are plotted as Arrhenius-like plots $\ln(I_{\mathrm{SD}}/T^2)$ vs. $1/T$ in fig. B.1 a) and c). Thermionic emission corresponds to high temperatures which are shaded grey in the figure. Note that for higher source-drain voltages the current does not follow a strictly linear behaviour at high T anymore: In the data in fig. B.1 a) and c), one can observe that the curves $\ln(I_{\mathrm{SD}}/T^2)$ vs. $1000/T$ have maxima which can best be seen in fig. B.1 c). Above certain values for V_{SD}, the current does not follow the Richardson characteristic anymore. We restricted the analysis to the negative slopes in the data.

This slope does not yet yield the height of a Schottky barrier, ϕ_{SB}, but a barrier of reduced height $\varphi_B = \phi_{SB} - \Delta\phi$. The barrier height is lowered by the electric field E_{SD} from the source-drain voltage V_{SD} by image forces (*Schottky effect* [83]). The reduction is given by $\Delta\phi = \sqrt{\frac{e^2 E_{\mathrm{SD}}}{4\pi\epsilon_0}}$. Hence, values φ_B obtained from the Arrhenius plots have to be extrapolated to $V_{\mathrm{SD}} = 0$ to yield ϕ_{SB}. We extracted ϕ_{SB} for several back-gate voltages in this way. Two exemplary extrapolations for backgate voltages V_{BG} of 25 V and 20 V are shown in fig. B.1 b and d). The comparison of all back-gate-dependent values is presented in e).

We see that our ϕ_{SB} are below the barrier height of 150 mV given in the paper by Das *et al.* [129] who state that the true Schottky barrier height can be given if tunnelling is fully suppressed. This is the case if V_{BG} is chosen such that the MoS_2 transistor is exactly in the flat-band condition (see fig. B.1 f) which marks the transition from tunnelling to pure thermionic emission. It is very probable that our gate voltages do not correspond to this condition yet.

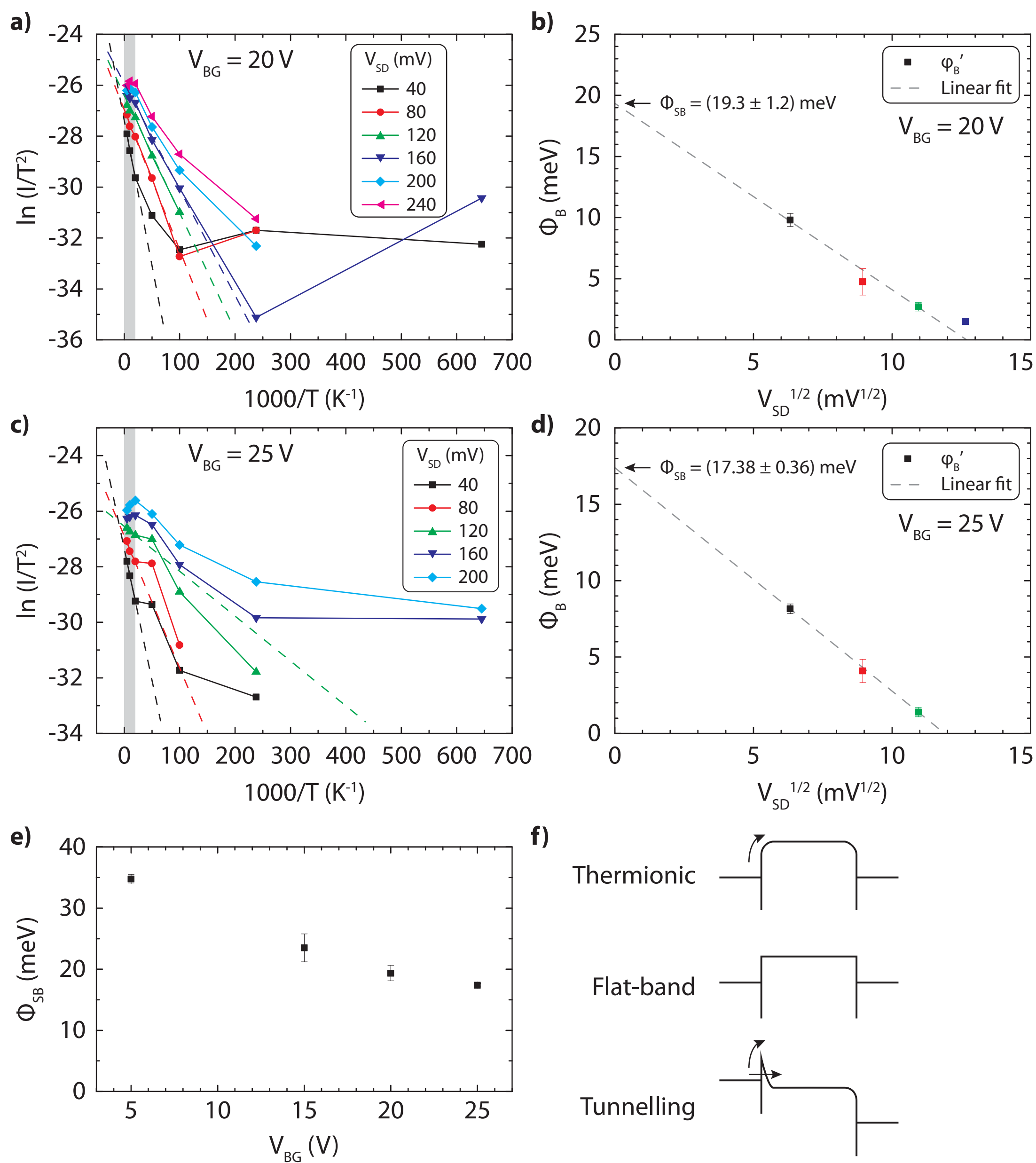

Figure B.1: Extraction of the Schottky barrier height. **a)** $\ln(I_{SD}/T^2)$ for different temperatures at V_{BG} = 20 V. The lines are linear fits in the high-temperature regime for $V_{SD} \leq 160$ mV. **b)** Effective barrier heights extracted from the linear fits in a), in dependence of $\sqrt{V_{SD}}$. The colour of the data points correspond to their V_{SD}, the error bars originate from the fits in a). **c)** and **d)** show corresponding data for V_{BG} = 25 V, where values for $V_{SD} \leq 120$ mV were extracted. **e)** Back-gate dependence of the extracted barrier heights ϕ_{SB} as intercepts from the linear fits in b) and d). The intercept error was used for the error bars in e). **f)** Band structures in the thermionic, flat-band and tunnelling regimes (adapted from [129]).

Appendix C

Offset voltages in non-local measurements

In an ideal spin-valve measurement, both voltage probes are on the same electrostatic potential ϕ_0, but have slightly different chemical potentials due to the relaxation of the injected spins. This results in a non-local voltage signal which is symmetric about the reference potential ϕ_0 and which can assume the values $V_{\mathrm{nl,P}}$ for parallel electrode magnetisation and $V_{\mathrm{nl,AP}}$ for the antiparallel case. Ideally, we measure $V_{\mathrm{nl,P}} = -V_{\mathrm{nl,AP}}$. In our measurements, we observed that our values for $V_{\mathrm{nl,P}}$ and $V_{\mathrm{nl,AP}}$ were centered around an offset voltage $V_{\mathrm{off}} > 0$ (see fig. C.1), and we have begun to investigate the cause of these offsets.

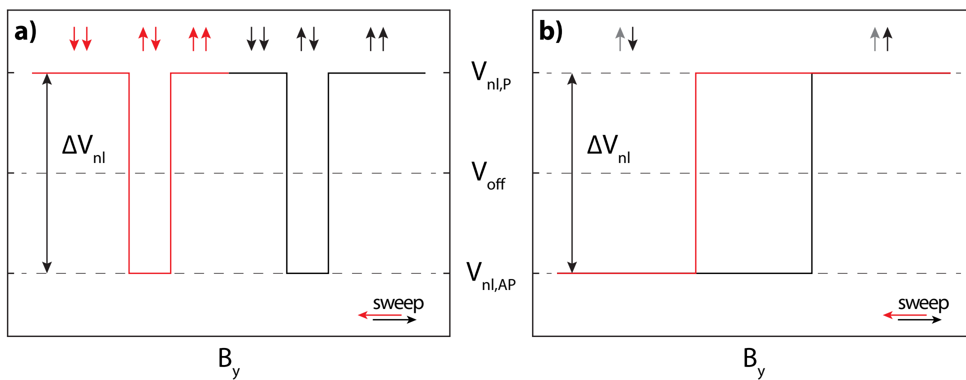

Figure C.1: Sketch of a non-local measurement for two sweep directions of B_y. a) represents the expected case described in section 1.2.6, b) the case of an electrode with pinned magnetisation, symbolised by the grey arrow. In our measurements, $V_{\mathrm{nl,P}}$ and $V_{\mathrm{nl,AP}}$ were centered around an offset voltage $V_{\mathrm{off}} \neq 0$.

C.1 Common-mode signal from the voltage amplifier

A possible source for offset voltages are common-mode signals from the voltage amplifiers. The output voltage of an instrumentation amplifier is the sum of the differential and the common-mode signal:

$$V_{\text{out}} = G_B \left[\underbrace{\gamma_{\text{diff}}(V_A - V_B)}_{\text{Differential signal}} + \underbrace{\gamma_{\text{cm}} \frac{V_A + V_B}{2}}_{\text{Common-mode signal}} \right] \tag{C.1}$$

V_A and V_B are the input signals (V_+ and V_- of the non-local measurements). G_B is the buffer gain of the amplifier (see below) and γ_{diff} its differential gain which is essentially 1 in the used amplifier models. γ_{CM} is the common-mode gain of the instrumentation amplifier and ideally 0 in order to fully suppress the undesired common-mode signal. Due to technological reasons, its values are slightly above zero and the resulting CM signal could be responsible for the offset voltages in our measurements.

The common-mode signal can be measured by applying the same voltage to both inputs A and B, thus subtracting the differential signal. In this case, the common-mode voltage reads:

$$V_{\text{out}} = V_{\text{CM}} = G_B \gamma_{\text{CM}} V_A \tag{C.2}$$

for $V_A = V_B$. Our amplifiers are designed such that their values for γ_{CM} are very low which gives themn the ability to reject the common-mode signal to a certain extent. This ability is specified by the *common-mode rejection ratio*, CMRR:

$$\text{CMRR}_{\text{dB}} = 20 \log_{10} \frac{\gamma_{\text{diff}}}{\gamma_{\text{cm}}} = 20 \log_{10} \frac{1}{\gamma_{\text{cm}}}. \tag{C.3}$$

We used the following amplifiers for the spin-valve measurements[1]:

- An SR830[2] lock-in amplifier, mainly used for the Al_2O_3 devices where $G_B = 1$ (fixed) and CMRR = 87 dB (manual: 100 dB)
- An LI-75A[3] preamplifier, mainly used for the MgO devices where $G_B = 100$ (fixed) and CMRR = 109 dB (manual: 120 dB)
- An SR560[4] preamplifier, mainly used for the MoS_2 devices where $G_B = 1 \ldots 50000$ and CMRR = 92 dB (manual: 90 dB)

[1]The usage of different amplifiers for different barrier materials is pure coincidence

The test circuit which we used to measure the different V_{CM} is sketched in fig. C.2 a). To simulate the conditions of our non-local measurements, we supplied both inputs with voltages comparable to those applied to our samples. The resulting common-mode signals are shown as joined data points in fig. C.2 b).

In addition to the common-mode voltages, the offset voltages extracted from the non-local measurements are plotted in the graph as well: The black filled squares correspond to the SR830 lock-in and stem exclusively from samples with Al_2O_3 barriers, the red filled circles are from MgO barriers and were measured with the LI-75A amplifier. The blue triangles come from MoS_2 and were obtained with the SR560 preamplifier. If the common-mode voltage of these amplifiers is responsible for the observed offset values, the data points from these the spin-valve measurements (Al_2O_3, MgO and MoS_2 barriers) should coincide with the common-mode signals. The arrow is explained in section C.2.

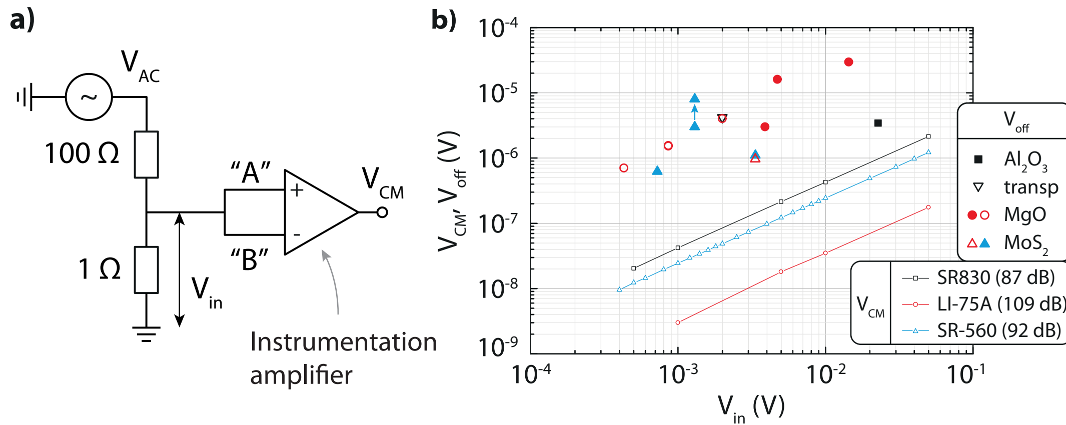

Figure C.2: a) Setup for the measurement of the common-mode voltage. The same input voltage V_{in} is applied to the inputs of the voltage amplifier. **b)** Offset voltages V_{off} from non-local measurements and common mode signals V_{CM} from the used amplifiers as a function of the applied bias V_{in}. The shape of the symbols represents the tunnel barrier material and their colour corresponds to the voltage amplifier used for measuring.

The figure shows that the measured common-mode signals are generally lower than the data points. The smallest difference could be observed for the Al_2O_3 data point. We conclude that the common-mode signals cannot explain the offset values and that other influences must be responsible.

[2]Stanford Research
[3]NF Corporation
[4]Stanford Research

C.2 Thermoelectric contributions from Joule or Peltier heating

A small feature in fig. C.2 b) could be a hint that the base temperature of the sample seems to play a certain role for the V_{off} as well: The blue arrow in fig. C.2 b) shows an increase in V_{nl} when the base temperature raised from 3 K to 10 K. Hence, there could be thermal contributions to the signals.

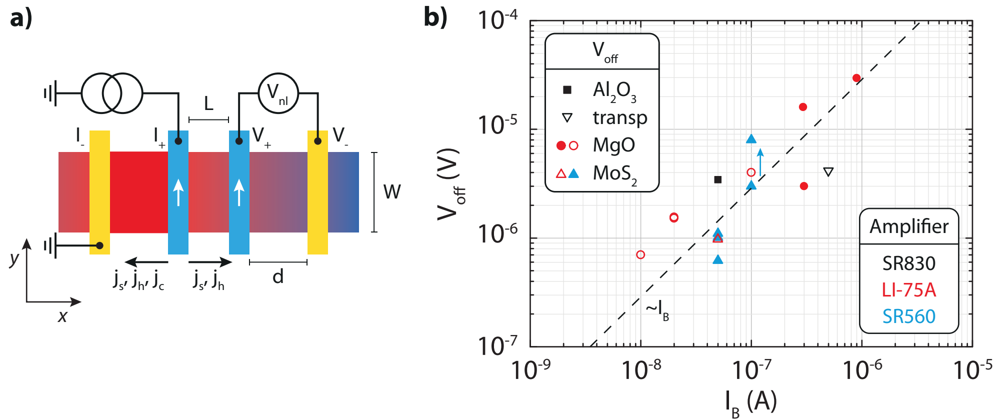

Figure C.3: a) Sketch of a non-local spin-valve device consisting of two ferromagnetic inner and two non-magnetic outer contacts on graphene. Between V_+ and V_-, pure spin and heat currents j_s and j_h are flowing because the spin injector electrode also acts as resistive heater. The colour symbolises the temperature gradient. **b)** Offset voltage as a function of the bias current I_B. Colour and shape of the symbols correspond to fig. C.2 b). The black broken line is a guide to the eye, indicating a linear dependence. The arrow denotes the change of the non-local voltage when the base temperature in the cryostat was raised from 3 K to 10 K.

The bias current I_B flowing between contacts I_+ and I_- does not only cause a non-local spin current but also a temperature gradient $\frac{dT}{dx}$ along the x direction through Joule and possibly also Peltier heating. This T gradient causes electrons to diffuse from the hot to the cold part of the sample which establishes an electric field $\frac{dV}{dx}$ in the direction of and proportional to $\frac{dT}{dx}$.

Peltier heating caused by a heat flow $\Delta T \propto \dot{Q} \propto I$ depends linearly on the current. Since fig. C.3 b) suggests a possible linear dependence of V_{off} on the bias current I_B, this mechanism could be a possible explanation. More data values need to be recorded to verify this assumption.

The temperature gradient caused by Joule heating is proportional to the heating power P given by the injected current and the two-terminal resistance:

$$\Delta T \propto I_B^2 R_{2\mathrm{T}} = P \tag{C.4}$$

The proportionality constant of the gradients is the *Seebeck coefficient* S which, in the case of linear gradients, can be written as

$$S = \frac{\Delta V}{\Delta T}. \tag{C.5}$$

These two equations yield an expression for the proportionality between heating power and thermovoltage:

$$\Delta V = S\Delta T \propto I_B^2 R_{2\mathrm{T}} = P \tag{C.6}$$

The square of I_B results in a signal $I_B^2 \propto \sin^2(\omega t)$ which is only present at an excitation frequency 2ω. Measuring at higher harmonics can reveal additional effects caused by Joule heating [153].

C.3 Conclusion

A certain voltage offset which is present in our non-local measurements could not be explained by the common-mode signal of the voltage amplifier, but may be caused by Peltier heating at the injection electrodes. A closer investigation of the interplay between charge, spin and heat currents could lead to very insightful follow-up experiments in the field of *spin caloritronics* [154].

Appendix D

Correlation between contact resistances and non-local signals

Chapters 3, 4 and 5 of this thesis describe our attempts to fabricate non-local spin-valve devices with Al_2O_3, MgO and MoS_2 tunnel barriers, as well as the optimisation of the barriers. We measured non-local resistance jumps on several devices and managed to give a rough estimate for our spin polarisation for an MgO sample which lies between 5 % and 30 %, assuming fully tunnelling barriers. Since the AFM surface maps of the oxides (figs. 3.11 and 4.5) still showed inhomogeneities and since we observed cracks and bubbles in the MoS_2 layer, we are convinced that the barriers in our devices are pinhole-dominated.

In light of the possibility of spin relaxation at the contacts [41], it can be very instructive to compare the obtained values for ΔR_{nl} and to relate them to the resistance of the tunnel barrier at the injection and detection contacts. In analogy to Seneor *et al.* [10], we use eqn. (1.12) to find a relation between the non-local resistance jump ΔR_{nl} and the barrier resistance R_B. Written as a reduced spin signal (RSS), i. e. in the form $\frac{\Delta R_{\mathrm{nl}}}{R_G^s}$, the left-hand side is a function of the reduced barrier resistance (RBR), $\frac{R_B}{R_G^s}$. The function only depends on two parameters, the ratio of the lengths of graphene channel and spin relaxation length L/λ_G and the polarisation P_T of the injected spins. In this form, eqn. (1.12) reads:

$$\frac{\Delta R_{\mathrm{nl}}}{R_G^s} = 4e^{-\ell} \frac{P_T^2 \left(\frac{R_B}{R_G^s}\right)^2}{\left(1 - P_T^2 + 2\frac{R_B}{R_G^s}\right)^2 - \left(1 - P_T^2\right)^2 e^{-2\ell}} \quad \text{where} \quad \ell := \frac{L}{\lambda_G} \tag{D.1}$$

In order to compare our data with this model, we have to bring them into the form RSS vs. RBR as well. Since we could not obtain all necessary parameters, we will have to make assumptions about some of them, e. g. the resistances of graphene and permalloy, R_G and R_{Py}. Together with the measured two-terminal resistances $R_{2\mathrm{T}}$, these allow us to estimate the barrier resistance:

$$R_B = \frac{R_{2\mathrm{T}} - R_G}{2} - R_{\mathrm{Py}}. \tag{D.2}$$

R_G (kΩ)	R_{Py} (kΩ)	ℓ	$\Delta\ell$
1.8 ± 1.3	1.4 ± 0.4	1.5	1

Table D.1: Ranges for several parameters in eqn. (1.12). The assumptions are very general and thus produce large error margins.

This formula gives the average barrier resistance of injector and detector. We assumed the same estimates for R_G and R_{Py} as in section 4.4.3. The error of the measured R_{2T} is much smaller than these margins and can be neglected here. There are several other parameters to consider: As stated in section 1.2.6, eqn. (1.12) depends on the polarisation of the injected spins P_T and the spin resistance of graphene $R^s_G = \frac{\lambda_G}{\sigma_G W}$. The latter requires the knowledge of the conductivity of graphene, the channel width and the spin diffusion length λ_G (or, the dimensionless parameter ℓ, see eqn. (D.1)). Since most of our devices have rectangular graphene transport channels, we can write $R^s_G = R_G/\ell$. All parameters are compiled in table D.1. The TMR polarisation P_T for permalloy is reported to lie between 45 % and 48 % [27–29].

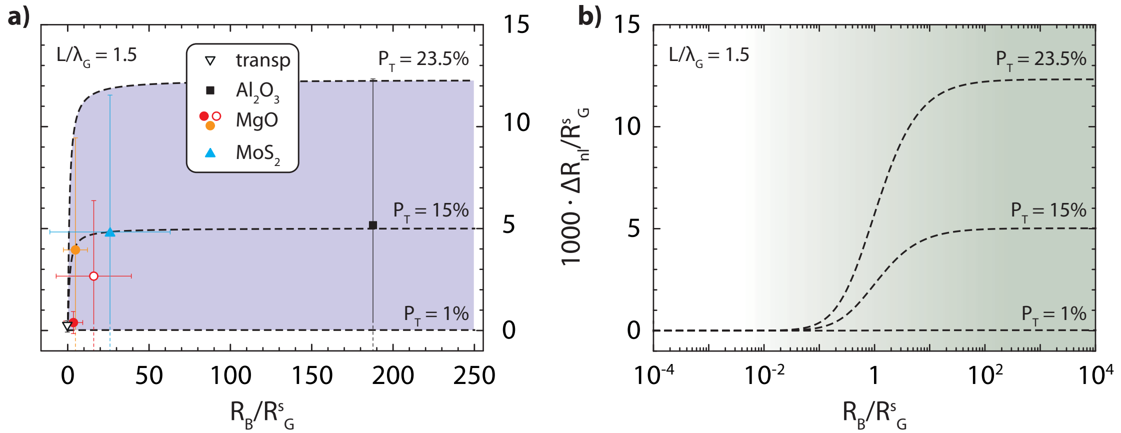

Figure D.1: Reduced spin signal as a function of the reduced barrier resistance. **a)** The data points were extracted from spin-valve measurements on TiO_2-Al_2O_3, MgO and MoS_2 barriers and transparent contacts. They should be regarded as quantitative indicators because of the large error bars which stem from the large error margins in table D.1. The orange data point denotes the Hanle data from section 4.4.3, the red circle with the white filling corresponds to single jumps on another MgO barrier sample. The error bars originate from the very cautious estimates for R_G, R_{Py} and ℓ. The model curves in both panels were plotted from eqn. (D.1) and correspond to different values of P_T. **b)** The logarithmic plot of the model curves in a) illustrates the contact relaxation (white) and channel relaxation (green) regions. Only one data point from the Al_2O_3 samples is in this region.

In addition to the data points, fig. D.1 b) shows RSS-vs.-RBR curves for several values of P_T. These mark more or less the maximum and minimum range of

all the data including the error bars. This range is very large because of our necessarily generous assumptions about the data points. Hence, this analysis should be regarded as qualitative rather than quantitative.

The modeled curves provide a good overview over three regimes of the barrier resistances. The region near $R_B = 0$ corresponds to very transparent barriers, and we can expect a sizeable contribution of spin relaxation at the contacts for devices with resistance ratios in the range $R_B/R_G^s < 0.1$. Our data point for transparent barriers lies essentially at zero. On the right-hand side, above $R_B/R_G^s \approx 50$, the maximum spin signal can be achieved and it saturates with increasing barrier resistances. Between transparent and tunnelling barriers, there is a transition regime where the spin signals strongly depend on the contact resistance. This can be interpreted as regime for pinhole-dominated tunnelling.

From the data points and the curves, we can see that most of our data points are grouped in the intermediate or transparent barrier regime. Only the black square, taken from the TiO_2-Al_2O_3 sample (black filled square) seems to correspond to a true tunnel barrier. We conclude that we mostly produced barriers which exhibit pinhole-dominated transport or were even transparent.

Bibliography

[1] G. A. Prinz, *Magnetoelectronics*, Science **282**, 1660 (1998).

[2] S. A. Wolf, *Spintronics: A spin-based electronics vision for the future*, Science **294**, 1488 (2001).

[3] I. Žutić, J. Fabian, and S. Das Sarma, *Spintronics: Fundamentals and applications*, Rev. Mod. Phys. **76**, 323 (2004).

[4] S. Bader and S. Parkin, *Spintronics*, Annu. Rev. Cond. Mat. Phys. **1**, 71 (2010).

[5] M. N. Baibich, J. M. Broto, A. Fert, F. N. Van Dau, and F. Petroff, *Giant magnetoresistance of (001)Fe/(001)Cr magnetic superlattices*, Phys. Rev. Lett. **61**, 2472 (1988).

[6] G. Binasch, P. Grünberg, F. Saurenbach, and W. Zinn, *Enhanced magnetoresistance in layered magnetic structures with antiferromagnetic interlayer exchange*, Phys. Rev. B **39**, 4828 (1989).

[7] D. Loss and D. P. DiVincenzo, *Quantum computation with quantum dots*, Phys. Rev. A **57**, 120 (1998).

[8] K. S. Novoselov, A. K. Geim, S. V. Morozov, D. Jiang, Y. Zhang, S. V. Dubonos, I. V. Grigorieva, and A. A. Firsov, *Electric field effect in atomically thin carbon films*, Science **306**, 666 (2004).

[9] A. K. Geim and K. S. Novoselov, *The rise of graphene*, Nat. Mater. **6**, 183 (2007).

[10] P. Seneor, B. Dlubak, M.-B. Martin, A. Anane, H. Jaffres, and A. Fert, *Spintronics with graphene*, MRS Bull. **37**, 1245 (2012).

[11] N. Tombros, C. Josza, M. Popinciuc, H. T. Jonkman, and B. J. van Wees, *Electronic spin transport and spin precession in single graphene layers at room temperature*, Nature **448**, 571 (2007).

[12] E. I. Rashba, *Theory of electrical spin injection: Tunnel contacts as a solution of the conductivity mismatch problem*, Phys. Rev. B **62**, R16267 (2000).

[13] G. Schmidt, D. Ferrand, L. W. Molenkamp, A. T. Filip, and B. J. van Wees, *Fundamental obstacle for electrical spin injection from a ferromagnetic metal into a diffusive semiconductor*, Phys. Rev. B **62**, 4790 (2000).

[14] J. Stöhr and H. C. Siegmann, *Magnetism – From fundamentals to nanoscale dynamics* (Springer, 2006).

[15] M. Getzlaff, *Fundamentals of magnetism* (Springer, 2008).

[16] H. Ibach and H. Lüth, *Solid state physics* (Springer-Verlag, 2009).

[17] H. Aurich, *Carbon nanotube spin valve with optimized ferromagnetic contacts*, Ph.D. thesis, Universität Basel (2012).

[18] H. J. van Leeuwen, *Problèmes de la théorie électronique du magnétisme*, J. Phys. Radium **2**, 361 (1921).

[19] L. Bergmann and C. Schaefer, *Lehrbuch der Experimentalphysik – Band 6: Festkörper*, 2nd ed., edited by R. Kassing (de Gruyter, 2005).

[20] I. I. Mazin, *How to define and calculate the degree of spin polarization in ferromagnets*, Phys. Rev. Lett. **83**, 1427 (1999).

[21] E. C. Stoner and E. P. Wohlfarth, *A mechanism of magnetic hysteresis in heterogeneous alloys*, Phil. Trans. R. Soc. A **240**, 599 (1948).

[22] W. Thomson, *On the electro-dynamic qualities of metals: Effects of magnetization on the electric conductivity of nickel and of iron*, Proc. R. Soc. A **8**, 546 (1857).

[23] H. Aurich, A. Baumgartner, F. Freitag, A. Eichler, J. Trbovic, and C. Schönenberger, *Permalloy-based carbon nanotube spin-valve*, Appl. Phys. Lett. **97**, 153116 (2010).

[24] T. McGuire and R. Potter, *Anisotropic magnetoresistance in ferromagnetic 3d alloys*, IEEE Trans. Mag. **11**, 1018 (1975).

[25] V. D. Nguyen, C. Naylor, L. Vila, A. Marty, P. Laczkowski, C. Beigné, L. Notin, Z. Ishaque, and J. P. Attané, *Magnon magnetoresistance of NiFe nanowires: Size dependence and domain wall detection*, Appl. Phys. Lett. **99**, 262504 (2011).

[26] D. Preusche, S. Schmidmeier, E. Palleecchi, C. Dietrich, A. K. Hüttel, J. Zweck, and C. Strunk, *Characterization of ferromagnetic contacts to carbon nanotubes*, J. Appl. Phys. **106**, 084314 (2009).

[27] J. S. Moodera, J. Nassar, and G. Mathon, *Spin tunnelling in ferromagnetic junctions*, Annu. Rev. Mat. Sci. **29**, 381 (1999).

[28] B. Nadgorny, R. Soulen, M. Osofsky, I. Mazin, G. Laprade, R. van de Veerdonk, A. Smits, S. Cheng, E. Skelton, and S. Qadri, *Transport spin polarization of Ni_xFe_{1-x}: Electronic kinematics and band structure*, Phys. Rev. B **61**, R3788 (2000).

[29] D. J. Monsma and S. S. P. Parkin, *Spin polarization of tunneling current from ferromagnet/Al_2O_3 interfaces using copper-doped aluminum superconducting films*, Appl. Phys. Lett. **77**, 720 (2000).

[30] S. Dubois, L. Piraux, J. M. George, K. Ounadjela, J. L. Duvail, and A. Fert, *Evidence for a short spin diffusion length in permalloy from the giant magnetoresistance of multilayered nanowires*, Phys. Rev. B **60**, 477 (1999).

[31] S. Steenwyk, S. Hsu, R. Loloee, J. Bass, and W. P. Jr., *Perpendicular-current exchange-biased spin-valve evidence for a short spin-diffusion lenght in permalloy*, J. Magn. Magn. Mater. **170**, L1 (1997).

[32] R. K. Kawakami, K. McCreary, and Y. Li, "Nanoelectronics and photonics: From atoms to materials, devices, and architectures," (Springer, 2008) Chap. Fundamentals of spintronics in metal and semiconductor systems, p. 59.

[33] N. F. Mott, *The electrical conductivity of transition metals*, Proc. R. Soc. A **153**, 699 (1936).

[34] N. F. Mott, *The resistance and thermoelectric properties of the transition metals*, Proc. R. Soc. A **156**, 368 (1936).

[35] M. Jullière, *Tunneling between ferromagnetic films*, Phys. Lett. A **54**, 225 (1975).

[36] M. Johnson and R. H. Silsbee, *Coupling of electronic charge and spin at a ferromagnetic-paramagnetic metal interface*, Phys. Rev. B **37**, 5312 (1988).

[37] C. Józsa, T. Maassen, M. Popinciuc, P. J. Zomer, A. Veligura, H. T. Jonkman, and B. J. van Wees, *Linear scaling between momentum and spin scattering in graphene*, Phys. Rev. B **80**, 241403 (2009).

[38] R. Fiederling, M. Keim, G. Reuscher, W. Ossau, G. Schmidt, A. Waag, and L. W. Molenkamp, *Injection and detection of a spin-polarized current in a light-emitting diode*, Nature **402**, 787 (1999).

[39] Y. Ohno, D. K. Young, B. Beschoten, F. Matsukura, H. Ohno, and D. D. Awschalom, *Electrical spin injection in a ferromagnetic semiconductor heterostructure*, Nature **402**, 790 (1999).

[40] T. Maassen, I. J. Vera-Marun, M. H. D. G. aes, and B. J. van Wees, *Contact-induced spin relaxation in Hanle spin precession measurements*, Phys. Rev. B **86**, 235408 (2012).

[41] F. Volmer, M. Drögeler, E. Maynicke, N. von den Driesch, M. L. Boschen, G. Güntherodt, and B. Beschoten, *Role of MgO barriers for spin and charge transport in Co/MgO/graphene nonlocal spin-valve devices*, Phys. Rev. B **88**, 161405(R) (2013).

[42] J. Zhou and M. Wu, *Spin relaxation due to the Bir-Aronov-Pikus mechanism in intrinsic and p-type GaAs quantum wells from a fully microscopic approach*, Phys. Rev. B **77**, 075318 (2008).

[43] S. Datta and B. Das, *Electronic analog of the electro-optic modulator*, Appl. Phys. Lett. **56**, 665 (1990).

[44] F. J. Jedema, *Electrical spin injection in metallic mesoscopic spin valves*, Ph.D. thesis, Rijksuniversiteit Groningen (2002).

[45] M. Johnson and R. H. Silsbee, *Interfacial charge-spin coupling: Injection and detection of spin magnetisation in metals*, Phys. Rev. Lett. **55**, 1790 (1985).

[46] S. Takahashi and S. Maekawa, *Spin injection and detection in magnetic nanostructures*, Phys. Rev. B **67**, 052409 (2003).

[47] F. J. Jedema, H. B. Heersche, A. T. Filip, J. J. A. Baselmans, and B. J. van Wees, *Electrical detection of spin precession in a metallic mesoscopic spin valve*, Nature **416**, 713 (2002).

[48] W. Han, K. Pi, K. M. McCreary, Y. Li, J. J. I. Wong, A. G. Swartz, and R. K. Kawakami, *Tunneling spin injection into single layer graphene*, Phys. Rev. Lett. **105**, 167202 (2010).

[49] A. H. Castro Neto, F. Guinea, N. M. R. Peres, K. S. Novoselov, and A. K. Geim, *The electronic properties of graphene*, Rev. Mod. Phys. **81**, 109 (2009).

[50] S. Das Sarma, S. Adam, E. H. Hwang, and E. Rossi, *Electronic transport in two-dimensional graphene*, Rev. Mod. Phys. **83**, 407 (2011).

[51] N. M. R. Peres, *The transport properties of graphene: An introduction*, Rev. Mod. Phys. **82**, 2673 (2010).

[52] M. O. Goerbig, *Electronic properties of graphene in a strong magnetic field*, Rev. Mod. Phys. **83**, 1193 (2011).

[53] K. S. Novoselov, D. Jiang, F. Schedin, T. J. Booth, V. V. Khotkevich, S. V. Morozov, and A. K. Geim, *Two-dimensional atomic crystals*, Proc. Natl. Acad. Sci. USA **102**, 10451 (2005).

[54] X. Li, W. Cai, J. An, S. Kim, J. Nah, D. Yang, R. Piner, A. Velamakanni, I. Jung, E. Tutuc, S. K. Banerjee, L. Colombo, and R. S. Ruoff, *Large-area synthesis of high-quality and uniform graphene films on copper foils*, Science **324**, 1312 (2009).

[55] M. P. Levendorf, C. S. Ruiz-Vargas, S. Garg, and J. Park, *Transfer-free batch fabrication of single-layer graphene transistors*, Nano Lett. **9**, 4479 (2009).

[56] Y. Lee, S. Bae, H. Jang, S. Jang, S.-E. Zhu, S. H. Sim, Y. I. Song, B. H. Hong, and J.-H. Ahn, *Wafer-scale synthesis and transfer of graphene films*, Nano Lett. **10**, 490 (2010).

[57] X. Li, Y. Zhu, W. Cai, M. Borysiak, B. Han, D. Chen, R. D. Piner, L. Colombo, and R. S. Ruoff, *Transfer of large-Area graphene films for high-performance transparent conductive electrodes*, Nano Lett. **9**, 4359 (2009).

[58] S. Bae, H. Kim, Y. Lee, X. Xu, J.-S. Park, Y. Zheng, J. Balakrishnan, T. Lei, H. Ri Kim, Y. I. Song, Y.-J. Kim, K. S. Kim, B. Ozyilmaz, J.-H. Ahn, B. H. Hong, and S. Iijima, *Roll-to-roll production of 30-inch graphene films for transparent electrodes*, Nat. Nano. **5**, 574 (2010).

[59] T. Kobayashi, M. Bando, N. Kimura, K. Shimizu, K. Kadono, N. Umezu, K. Miyahara, S. Hayazaki, S. Nagai, Y. Mizuguchi, Y. Murakami, and D. Hobara, *Production of a 100-m-long high-quality graphene transparent conductive film by roll-to-roll chemical vapor deposition and transfer process*, Appl. Phys. Lett. **102**, 023112 (2013).

[60] R. Quhe, J. Zheng, G. Luo, Q. Liu, R. Qin, J. Zhou, D. Yu, S. Nagase, W.-N. Mei, Z. Gao, and J. Lu, *Tunable and sizable band gap of single-layer graphene sandwiched between hexagonal boron nitride*, NPG Asia Mater. **4**, e6 (2012).

[61] P. Wallace, *The band theory of graphite*, Phys. Rev. **71**, 622 (1947).

[62] C. Schönenberger, “Band structure of graphene and carbon nanotubes: An exercise in condensed matter physics,” (2000).

[63] J.-H. Chen, C. Jang, S. Adam, M. S. Fuhrer, E. D. Williams, and M. Ishigami, *Charged-impurity scattering in graphene*, Nat. Phys. **4**, 377 (2008).

[64] A. S. Mayorov, D. C. Elias, I. S. Mukhin, S. V. Morozov, L. A. Ponomarenko, K. S. Novoselov, A. K. Geim, and R. V. Gorbachev, *How close can one approach the Dirac point in graphene experimentally?*, Nano Lett. **12**, 4629 (2012).

[65] J. Martin, N. Akerman, G. Ulbricht, T. Lohmann, J. H. Smet, and K. von Klitzing, *Observation of electron–hole puddles in graphene using a scanning single-electron transistor*, Nat. Phys. **4**, 144 (2008).

[66] K. Bolotin, K. Sikes, Z. Jiang, M. Klima, G. Fudenberg, J. Hone, P. Kim, and H. Stormer, *Ultrahigh electron mobility in suspended graphene*, Solid State Commun. **146**, 351 (2008).

[67] P. Rickhaus, R. Maurand, M.-H. Liu, M. Weiss, K. Richter, and C. Schönenberger, *Ballistic interferences in suspended graphene*, Nature Comm. **4**, 2342 (2013).

[68] C. R. Dean, A. F. Young, I. Meric, C. Lee, L. Wang, S. Sorgenfrei, K. Watanabe, T. Taniguchi, P. Kim, K. L. Shepard, and J. Hone, *Boron nitride substrates for high-quality graphene electronics*, Nat. Nano. **5**, 722 (2010).

[69] A. C. Ferrari and D. M. Basko, *Raman spectroscopy as a versatile tool for studying the properties of graphene*, Nat. Nano. **8**, 235 (2013).

[70] A. C. Ferrari, J. C. Meyer, V. Scardaci, C. Casiraghi, M. Lazzeri, F. Mauri, S. Piscanec, D. Jiang, K. S. Novoselov, S. Roth, and A. K. Geim, *Raman spectrum of graphene and graphene layers*, Phys. Rev. Lett. **97**, 187401 (2006).

[71] A. C. Ferrari, *Raman spectroscopy of graphene and graphite: Disorder, electron–phonon coupling, doping and nonadiabatic effects*, Solid State Commun. **143**, 47 (2007).

[72] Z. Ni, Y. Wang, T. Yu, and Z. Shen, *Raman spectroscopy and imaging of graphene*, Nano Res. **1**, 273 (2008).

[73] Y. You, Z. Ni, T. Yu, and Z. Shen, *Edge chirality determination of graphene by Raman spectroscopy*, Appl. Phys. Lett. **93**, 163112 (2008).

[74] W. Han and R. K. Kawakami, *Spin relaxation in single-Layer and bilayer graphene*, Phys. Rev. Lett. **107**, 047207 (2011).

[75] T.-Y. Yang, J. Balakrishnan, F. Volmer, A. Avsar, M. Jaiswal, J. Samm, S. R. Ali, A. Pachoud, M. Zeng, M. Popinciuc, G. Güntherodt, B. Beschoten, and B. Özyilmaz, *Observation of long spin-relaxation times in bilayer graphene at room temperature*, Phys. Rev. Lett. **107**, 047206 (2011).

[76] J. Fischer, B. Trauzettel, and D. Loss, *Hyperfine interaction and electron-spin decoherence in graphene and carbon nanotube quantum dots*, Phys. Rev. B **80**, 155401 (2009).

[77] C. Ertler, S. Konschuh, M. Gmitra, and J. Fabian, *Electron spin relaxation in graphene: The role of the substrate*, Phys. Rev. B **80**, 041405(R) (2009).

[78] K. Pi, W. Han, K. M. McCreary, A. G. Swartz, Y. Li, and R. K. Kawakami, *Manipulation of spin transport in graphene by surface chemical doping*, Phys. Rev. Lett. **104**, 187201 (2010).

[79] A. G. Swartz, J.-R. Chen, K. M. McCreary, P. M. Odenthal, W. Han, and R. K. Kawakami, *Effect of in-situ deposition of Mg adatoms on spin relaxation in graphene*, Phys. Rev. B **87**, 075455 (2013).

[80] W. Han, J.-R. Chen, D. Wang, K. M. McCreary, H. Wen, A. G. Swartz, J. Shi, and R. K. Kawakami, *Spin relaxation in single-layer graphene with tunable mobility*, Nano Lett. **12**, 3443 (2012).

[81] D. Kochan, M. Gmitra, and J. Fabian, *Spin relaxation mechanism in graphene: Resonant scattering by magnetic impurities*, Phys. Rev. Lett. **112**, 116602 (2014).

[82] B. Dlubak, M.-B. Martin, C. Deranlot, B. Servet, S. Xavier, R. Mattana, M. Sprinkle, C. Berger, W. A. de Heer, F. Petroff, A. Anane, P. Seneor, and A. Fert, *Highly efficient spin transport in epitaxial graphene on SiC*, Nat. Phys. **8**, 557 (2012).

[83] S. M. Sze and K. K. Ng, *Physics of semiconductor devices* (J. Wiley & Sons, Inc., 2007).

[84] G. G. Roberts and J. I. Polanco, *Thermally assisted tunnelling in dielectric films*, Phys. stat. sol. (a) **1**, 409 (1970).

[85] J. J. Åkerman, R. Escudero, C. Leighton, S. Kim, D. Rabson, R. W. Dave, J. Slaughter, and I. K. Schuller, *Criteria for ferromagnetic–insulator–ferromagnetic tunneling*, J. Magn. Magn. Mater. **240**, 86 (2002).

[86] J. M. Rowell, in *Tunneling phenomena in solids*, edited by E. Burnstein and S. Lundqvist (Plenum, New York, 1969) p. 273.

[87] U. Rüdiger, R. Calarco, U. May, K. Samm, J. Hauch, H. Kittur, M. Sperlich, and G. Güntherodt, *Temperature-dependent resistance of magnetic tunnel junctions as a quality proof of the barrier*, J. Appl. Phys. **89**, 7573 (2001).

[88] U. May, K. Samm, H. Kittur, J. Hauch, R. Calarco, U. Rüdiger, and G. Güntherodt, *Temperature-dependent magnetoresistance of magnetic tunnel junctions with ultraviolet light-assisted oxidized barriers*, Appl. Phys. Lett. **78**, 2026 (2001).

[89] R. L. Puurunen, *Surface chemistry of atomic layer deposition: A case study for the trimethylaluminum/water process*, J. Appl. Phys. **97**, 121301 (2005).

[90] S. M. George, *Atomic layer deposition: An overview*, Chem. Rev. **110**, 111 (2010).

[91] D. B. Farmer and R. G. Gordon, *Atomic layer deposition on suspended single-walled carbon nanotubes via gas-phase noncovalent functionalisation*, Nano Lett. **6**, 699 (2006).

[92] B. Lee, S. Y. Park, H. C. Kim, K. J. Cho, E. M. Vogel, M. J. Kim, R. M. Wallace, and J. Kim, *Conformal Al_2O_3 dielectric layer deposited by atomic layer deposition for graphene-based nanoelectronics*, Appl. Phys. Lett. **92**, 203102 (2008).

[93] X. Wang, S. M. Tabakman, and H. Dai, *Atomic layer deposition of metal oxides on pristine and functionalized graphene*, J. Am. Chem. Soc. **130**, 8152 (2008).

[94] T. Yamaguchi, S. Masubuchi, K. Iguchi, R. Moriya, and T. Machida, *Tunnel spin injection into graphene using Al_2O_3 barrier grown by atomic layer deposition on functionalized graphene surface*, J. Magn. Magn. Mater. **324**, 849 (2012).

[95] J. R. Williams, L. DiCarlo, and C. M. Marcus, *Quantum Hall effect in a gate-controlled p-n junction of graphene*, Science **317**, 638 (2007).

[96] W. H. Wang, W. Han, K. Pi, K. M. McCreary, F. Miao, W. Bao, C. N. Lau, and R. K. Kawakami, *Growth of atomically smooth MgO films on graphene by molecular beam epitaxy*, Appl. Phys. Lett. **93**, 183107 (2008).

[97] B. Fallahazad, K. Lee, G. Lian, S. Kim, C. M. Corbet, D. A. Ferrer, L. Colombo, and E. Tutuc, *Scaling of Al_2O_3 dielectric for graphene field-effect transistors*, Appl. Phys. Lett. **100**, 093112 (2012).

[98] Y. Xuan, Y. Q. Wu, T. Shen, M. Qui, M. A. Capano, J. A. Cooper, and P. D. Ye, *Atomic-layer deposited nanostructures for graphene-based nanoelectronics*, Appl. Phys. Lett. **92**, 013101 (2008).

[99] R. L. Puurunen, *Growth per cycle in atomic layer deposition: Real application examples of a theoretical model*, Chem. Vap. Depos. **9**, 327 (2003).

[100] B. Dlubak, P. Seneor, A. Anane, C. Barraud, C. Deranlot, D. Deneuve, B. Servet, R. Mattana, F. Petroff, and A. Fert, *Are Al_2O_3 and MgO tunnel barriers suitable for spin injection in graphene?*, Appl. Phys. Lett. **97**, 092502 (2010).

[101] J. C. Fisher and I. Giaever, *Tunneling through thin insulating layers*, J. Appl. Phys. **32**, 172 (1961).

[102] J. G. Simmons, *Generalized formula for the electric tunnel effect between similar electrodes separated by a thin insulating film*, J. Appl. Phys. **34**, 1793 (1963).

[103] F. Freitag, *Graphene: From diffusive to ultraclean-interacting systems*, Ph.D. thesis, Universität Basel (2012).

[104] W. Han, K. M. McCreary, K. Pi, W. H. Wang, Y. Li, H. Wen, J. R. Chen, and R. K. Kawakami, *Spin transport and relaxation in graphene*, J. Magn. Magn. Mater. **324**, 369 (2011).

[105] B. Dlubak, M.-B. Martin, C. Deranlot, K. Bouzehouane, S. Fusil, R. Mattana, F. Petroff, A. Anane, P. Seneor, and A. Fert, *Homogeneous pinhole-free 1 nm Al_2O_3 tunnel barriers on graphene*, Appl. Phys. Lett. **101**, 203104 (2012).

[106] J. Mathon and A. Umerski, *Theory of tunneling magnetoresistance of an epitaxial Fe/MgO/Fe(001) junction*, Phys. Rev. B **63**, 220403 (2001).

[107] S. S. P. Parkin, C. Kaiser, A. Panchula, P. M. Rice, B. Hughes, M. Samant, and S.-H. Yang, *Giant tunnelling magnetoresistance at room temperature with MgO (100) tunnel barriers*, Nat. Mater. **3**, 862 (2004).

[108] S. Ikeda, J. Hayakawa, Y. Ashizawa, Y. M. Lee, K. Miura, H. Hasegawa, M. Tsunoda, F. Matsukura, and H. Ohno, *Tunnel magnetoresistance of 604% at 300K by suppression of Ta diffusion in CoFeB-MgO-CoFeB pseudo-spin-valves annealed at high temperature*, Appl. Phys. Lett. **93**, 082508 (2008).

[109] L. A. Ponomarenko, R. Yang, R. V. Gorbachev, P. Blake, A. S. Mayorov, K. S. Novoselov, M. I. Katsnelson, and A. K. Geim, *Density of states and zero Landau level probed through capacitance of graphene*, Phys. Rev. Lett. **105**, 136801 (2010).

[110] G. Droulers, A. Beaumont, J. Beauvais, and D. Drouin, *Spectroscopic ellipsometry on thin titanium oxide layers grown on titanium by plasma oxidation*, J. Vac. Sci. Tech. B **29**, 021010 (2011).

[111] M. M. Benameur, B. Radisavljevic, J. S. Heron, S. Sahoo, H. Berger, and A. Kis, *Visibility of dichalcogenide nanolayers*, Nanotechnology **22**, 125706 (2011).

[112] H. Li, G. Lu, Y. Wang, Z. Yin, C. Cong, Q. He, L. Wang, F. Ding, T. Yu, and H. Zhang, *Mechanical exfoliation and characterization of single- and few-layer nanosheets of* WSe_2 *,* TaS_2 *, and* $TaSe_2$, Small **9**, 1974 (2013).

[113] R. Tenne, L. Margulis, M. Genut, and G. Hodes, *Polyhedral and cylindrical structures of tungsten disulphide*, Nature **360**, 444 (1992).

[114] N. G. Chopra, R. J. Luyken, K. Cherrey, V. H. Crespi, M. L. Cohen, S. G. Louie, and A. Zettl, *Boron nitride nanotubes*, Science **269**, 966 (1995).

[115] M. Remskar, A. Mrzel, Z. Skraba, A. Jesih, M. Ceh, J. Demsar, P. Stadelmann, F. Levy, and D. Mihailovic, *Self-Assembly of subnanometer-diameter single-wall* MoS_2 *nanotubes*, Science **292**, 479 (2001).

[116] M. Nath and C. N. R. Rao, $MoSe_2$ *and* WSe_2 *nanotubes and related structures*, Chem. Commun. **2001**, 2236 (2001).

[117] Y. B. Li, Y. Bando, and D. Golberg, MoS_2 *nanoflowers and their field-emission properties*, Appl. Phys. Lett. **82**, 1962 (2003).

[118] D. Hoffman, G. Doll, and P. Eklund, *Optical properties of pyrolytic boron nitride in the energy range 0.05 – 10 eV*, Phys. Rev. B **30**, 6051 (1984).

[119] K. Watanabe, T. Taniguchi, and H. Kanda, *Direct-bandgap properties and evidence for ultraviolet lasing of hexagonal boron nitride single crystal*, Nat. Mater. **3**, 404 (2004).

[120] R. F. Deacon and J. F. Goodman, *Lubrication by lamellar solids*, Proc. R. Soc. A **243**, 464 (1958).

[121] W. Gannett, W. Regan, K. Watanabe, T. Taniguchi, M. F. Crommie, and A. Zettl, *Boron nitride substrates for high mobility chemical vapor deposited graphene*, Appl. Phys. Lett. **98**, 242105 (2011).

[122] I. Meric, C. R. Dean, N. Petrone, L. Wang, J. Hone, P. Kim, and K. L. Shepard, *Graphene field-effect transistors based on boron nitride dielectrics*, Proc. IEEE **101**, 1609 (2013).

[123] A. S. Mayorov, R. V. Gorbachev, S. V. Morozov, L. Britnell, R. Jalil, L. A. Ponomarenko, P. Blake, K. S. Novoselov, K. Watanabe, T. Taniguchi, and A. K. Geim, *Micrometer-scale ballistic transport in encapsulated graphene at room temperature*, Nano Lett. **11**, 2396 (2011).

[124] L. Wang, I. Meric, P. Y. Huang, Q. Gao, Y. Gao, H. Tran, T. Taniguchi, K. Watanabe, L. M. Campos, D. A. Muller, J. Guo, P. Kim, J. Hone, K. L. Shepard, and C. R. Dean, *One-dimensional electrical contact to a two-dimensional material*, Science **342**, 6158 (2013).

[125] T. Yamaguchi, Y. Inoue, S. Masubuchi, S. Morikawa, M. Onuki, K. Watanabe, T. Taniguchi, R. Moriya, and T. Machida, *Electrical spin injection into graphene through monolayer hexagonal boron nitride*, APEX **6**, 073001 (2013).

[126] L. Britnell, R. V. Gorbachev, R. Jalil, B. D. Belle, F. Schedin, M. I. Katsnelson, L. Eaves, S. V. Morozov, A. S. Mayorov, N. M. R. Peres, A. H. C. Neto, J. Leist, A. K. Geim, L. A. Ponomarenko, and K. S. Novoselov, *Electron tunneling through ultrathin boron nitride crystalline barriers*, Nano Lett. **12**, 1707 (2012).

[127] W. Fu, P. Makk, R. Maurand, M. Bräuninger, and C. Schönenberger, *Large-scale fabrication of BN tunnel barriers for graphene spintronics*, J. Appl. Phys. **116**, 074306 (2014).

[128] B. Radisavljevic, A. Radenovic, J. Brivio, V. Giacometti, and A. Kis, *Single-layer MoS_2 transistors*, Nat. Nano. **6**, 147 (2011).

[129] S. Das, H.-Y. Chen, A. V. Penumatcha, and J. Appenzeller, *High-performance multilayer MoS_2 transistors with scandium contacts*, Nano Lett. **13**, 100 (2013).

[130] A. Splendiani, L. Sun, Y. Zhang, T. Li, J. Kim, C.-Y. Chim, G. Galli, and F. Wang, *Emerging photoluminescence in monolayer MoS_2*, Nano Lett. **10**, 1271 (2010).

[131] B. Radisavljevic, M. B. Whitwick, and A. Kis, *Integrated circuits and logic operations based on single-layer MoS_2*, ACS Nano **5**, 9934 (2011).

[132] O. Lopez-Sanchez, D. Lembke, M. Kayci, A. Radenovic, and A. Kis, *Ultrasensitive photodetectors based on monolayer MoS_2*, Nat. Nano. **8**, 497 (2013).

[133] K. Roy, M. Padmanabhan, S. Goswami, T. P. Sai, G. Ramalingam, S. Raghavan, and A. Ghosh, *Graphene-MoS_2 hybrid structures for multifunctional photoresponsive memory devices*, Nat. Nano. **8**, 826 (2013).

[134] S. Bertolazzi, D. Krasnozhon, and A. Kis, *Nonvolatile memory cells based on MoS_2/graphene heterostructures*, ACS Nano **7**, 3246 (2013).

[135] N. Myoung, K. Seo, S. J. Lee, and G. Ihm, *Large current modulation and spin-dependent tunneling of vertical graphene/MoS_2 heterostructures*, ACS Nano **7**, 7021 (2013).

[136] A. M. van der Zande, P. Y. Huang, D. A. Chenet, T. C. Berkelbach, Y. You, G.-H. Lee, T. F. Heinz, D. R. Reichman, D. A. Muller, and J. C. Hone, *Grains and grain boundaries in highly crystalline monolayer molybdenum disulphide*, Nat. Mater. **12**, 554 (2013).

[137] K. F. Mak, C. Lee, J. Hone, J. Shan, and T. F. Heinz, *Atomically thin MoS_2: A new direct-gap semiconductor*, Phys. Rev. Lett. **105**, 136805 (2010).

[138] B. Radisavljevic and A. Kis, *Mobility engineering and a metal-insulator transition in monolayer MoS_2*, Nat. Mater. **12**, 815 (2013).

[139] J. T. Ye, Y. J. Zhang, R. Akashi, M. S. Bahramy, R. Arita, and Y. Iwasa, *Superconducting dome in a gate-tuned band insulator*, Science **338**, 1193 (2012).

[140] K. Lee, H.-Y. Kim, M. Lotya, J. N. Coleman, G.-T-Kim, and G. S. Duesberg, *Electrical characteristics of molybdenum disulfide flakes produced by liquid exfoliation*, Adv. Mater. **23**, 4178 (2011).

[141] I. Popov, G. Seifert, and D. Tománek, *Designing electrical contacts to MoS_2 monolayers: A computational study*, Phys. Rev. Lett. **108**, 156802 (2012).

[142] H. Qiu, L. Pan, Z. Yao, J. Li, Y. Shi, and X. Wang, *Electrical characterization of back-gated bi-layer MoS_2 field-effect transistors and the effect of ambient on their performances*, Appl. Phys. Lett. **100**, 123104 (2012).

[143] M. Salou, B. Lescop, S. Rioual, A. Lebon, J. B. Youssef, and B. Rouvellou, *Initial oxidation of polycrystalline permalloy surface*, Surf. Sci. **602**, 2901 (2008).

[144] R. Murray and B. Evans, *The thermal expansion of 2H-MoS_2 and 2H-WSe_2 between 10 and 320 K*, J. Appl. Cryst. **12**, 312 (1979).

[145] S. U. Jen, P. J. Wang, Y. C. Tseng, and H. P. Chiang, *Planar Hall effect of permalloy films on Si(111), Si(100), and glass substrates*, J. Appl. Phys. **105**, 07E903 (2009).

[146] C. Dietrich, R. Hertel, M. Huber, D. Weiss, R. Schäfer, and J. Zweck, *Influence of perpendicular magnetic fields on the domain structure of permalloy microstructures grown on thin membranes*, Phys. Rev. B **77**, 174427 (2008).

[147] Y. S. Touloukian, R. K. Kirby, R. E. Taylor, and P. D. Desai, *Thermal expansion – Metallic elements and alloys*, Thermophysical properties of matter, Vol. 12 (IFI/Plenum New York-Washington, 1975).

[148] D. Bonnenberg, K. A. Hempel, and H. Wijn, in *Landolt-Börnstein - Group III Condensed Matter*, III, Vol. 19a: 3d, 4d and 5d elements, alloys and compounds (Springer) Chap. 1.2.1.2.10 Thermomagnetic properties, thermal expansion coefficient, specific heat, Debye temperature, thermal conductivity, p. 247.

[149] C. Lee, H. Yan, L. E. Brus, T. F. Heinz, J. Hone, and S. Ryu, *Anomalous lattice vibrations of single- and few-layer* MoS_2, ACS Nano **4**, 2695 (2010).

[150] H. Li, Q. Zhang, C. C. R. Yap, B. K. Tay, T. H. T. Edwin, A. Olivier, and D. Baillargeat, *From bulk to monolayer* MoS_2*: Evolution of Raman scattering*, Adv. Funct. Mater. **22**, 1385 (2012).

[151] S. Tongay, J. Zhou, C. Ataca, K. Lo, T. S. Matthews, J. Li, J. C. Grossman, and J. Wu, *Thermally driven crossover from indirect toward direct bandgap in 2D semiconductors:* $MoSe_2$ *versus* MoS_2, Nano Lett. **12**, 5576 (2012).

[152] T. Mohiuddin, A. Lombardo, R. Nair, A. Bonetti, G. Savini, R. Jalil, N. Bonini, D. Basko, C. Galiotis, N. Marzari, K. S. Novoselov, A. K. Geim, and A. C. Ferrari, *Uniaxial strain in graphene by Raman spectroscopy: G peak splitting, Grüneisen parameters, and sample orientation*, Phys. Rev. B **79**, 205433 (2009).

[153] J. Renard, M. Studer, and J. A. Folk, *Origins of nonlocality near the neutrality point in graphene*, arXiv **1309**, 7016 (2013).

[154] G. E. W. Bauer, E. Saitoh, and B. J. van Wees, *Spin caloritronics*, Nat. Mater. **11**, 391 (2012).

Curriculum Vitæ

Matthias Wolfgang Bräuninger
born September 13, 1981, in Deggendorf (Germany)

Education

- March 2014
  PhD in experimental physics at the University of Basel in the group of Prof. C. Schönenberger
  "Tunnel barriers for spin injection into graphene"
- September 2006 – September 2007
  Diploma thesis in the group of Prof. E. Umbach at the University of Würzburg
  "Transportmessungen an Diindenoperylen auf einem hochgeordneten Saphirsubstrat"
- 2001 – 2007
  Physics studies at the University of Würzburg, Germany
- 1992 – 2001
  Kaiser-Heinrich-Gymnasium Bamberg, Abitur

Professional positions

- March 2010 – March 2014
  Research assistant in the group of Prof. C. Schönenberger in Basel
  Field of interest: Electronic and spin transport in graphene (experimental physics)
- January 2008 – March 2009
  Research assistant in the group of Prof. B. Trauzettel in Würzburg
  Field of interest: Electronic transport in graphene (theoretical physics)

Teaching experience

- 2010 – 2014: Teaching assistant at the dept. of physics in Basel
- 2003 – 2009: Teaching assistant at the dept. of physics in Würzburg

Lectures

For valuable lectures during my studies I am indebted to:
W. Reusch, W. Ossau, R. Matzdorf, R. Tacke, M. v. Golitschek, W. Kinzel, J. Fricke, G. G. Gerber, W. Pfeiffer, H. Fraas († 2013), W. Wolfsberger, M. Böhm († 2013), J. Geurts, G. Reents, L. Molenkamp, C. Kanzow, E. Batke, K. Brunner, P. Müller, E. Umbach, R. Colditz

List of publications

Scientific articles

- *Temperature dependence of the conductivity of ballistic graphene*

  M. Müller, M. Bräuninger and B. Trauzettel, Phys. Rev. Lett. **103**, 196801 (2009)

- *Large-scale fabrication of BN tunnel barriers for graphene spintronics*

  W. Fu, P. Makk, R. Maurand, M. Bräuninger and C. Schönenberger, J. Appl. Phys. **116**, 074306 (2014)

Poster contributions

- *Graphene: The ultimate two-dimensional conductor*

  M. Bräuninger, M. Calame, W. Fu, F. Freitag, C. Nef, C. Schönenberger, J. Trbovic, M. Weiss

  First general meeting of NCCR-QSIT in Arosa (CH), January 2011

- *Novel transport phenomena in graphene*

  A. van der Torren, E. Tóvári, M. Bräuninger, P. Rickhaus, F. Freitag, J. Trbovic, R. Maurand, M. Weiss and C. Schönenberger

  NCCR-QSIT meeting in Arosa (CH), January 2012

- *Tunnel barriers for graphene spintronics*

  M. Bräuninger, R. Maurand and C. Schönenberger

  SPS meeting in Zürich (CH), June 2012

- *New graphene heterostructures*

  P. Rickhaus, M. Bräuninger, P. Makk, R. Maurand, M. Weiss and C. Schönenberger

  NCCR-QSIT meeing in Arosa (CH), January 2013

- *MoS_2 tunnel barriers for spin injection into graphene*

  P. Makk, M. Bräuninger, R. Maurand and C. Schönenberger

  Graphene week 2013 in Chemnitz (D), June 2013